Formation Mechanisms of "Negative"-Intensity Spots in the Cosmic Microwave Background Radiation and Distant Objects

V. K. Dubrovich*

Special Astrophysical Observatory, Russian Academy of Sciences, pos. Nizhniĭ Arkhyz, Stavropol kraĭ, 357147 Russia
Received June 2, 2000; in final form, October 2, 2000

Abstract—We consider the formation mechanisms of "negative"-intensity spots in the radio band for various astrophysical conditions. For wavelengths $\lambda < 1.5$ mm, the regions of reduced temperature (relative to the cosmic microwave background radiation, CMBR) are shown to be produced only by high-redshift objects moving at peculiar velocities. The main processes are CMBR Thomson scattering and bremsstrahlung. We show that the effect $\delta T/T$ can be $\sim 10^{-5}$ in magnitude. We derive simple analytic expressions, which allow the redshifts, electron densities, and linear sizes of these regions to be estimated from observed spectral and spatial parameters. Additional observational methods for refining these parameters are outlined. © 2001 MAIK "Nauka/Interperiodica".

Key words: *theoretical and observational cosmology*

INTRODUCTION

In the last 30 years, much attention has been given to the search for and a detailed analysis of spatial fluctuations in cosmic microwave background radiation (CMBR) temperature T_r. This is attributable to the fundamental information about the structure and parameters of the Universe that can be obtained from these studies. Theoretically, one of the most important problems is to analyze statistical parameters of the fluctuations: the correlation function and power spectrum of spatial scales.

New experimental possibilities enable a complete mapping of the sky to the level of the presumed primordial fluctuations. From the viewpoint of the theory of the initial fluctuation spectrum, this information is not fundamentally new, and it can be used only as an additional guarantee that we actually observe CMBR anisotropy.

The subject of our study is precisely this map. We will show that observational data obtained from its analysis can be used to search for protoobjects and allow their redshifts to be estimated. They yield the coordinates of areas that can be used for more detailed studies.

Since we are interested in high-redshift objects, the main problem is to determine the sources of their luminosity and to estimate their power. At the prestellar evolutionary stage of protoobjects, there are essentially only two formation mechanisms of the "glow." One of them is the Doppler distortion of external, equilibrium, and isotropic radiation (CMBR). For this to occur, the object must have a peculiar velocity V_p and some nonzero opacity.

In cool, weakly ionized matter, free electrons and primordial molecules can be the source of opacity (Sunyaev and Zel'dovich 1980; Dubrovich 1977, 1997). Molecules scatter CMBR only in narrow spectral bands. In the standard evolutionary model of matter after hydrogen recombination, the residual degree of ionization n_e/n_H at $z \approx 100$ in the absence of additional energy sources does not exceed 10^{-4}, where n_e and n_H are the number densities of free electrons and hydrogen atoms, respectively. This implies that the continuum optical depth τ_T due to Thomson scattering by free electrons is very small.

Another opacity mechanism in the presence of free electrons and protons is free–free absorption and emission. However, for this channel, the optical depth τ_{ff} is also small. Below, we numerically estimate the above depths. Note only that the mechanism of free–free absorption and emission will give additional emission if the temperature of matter T_m is higher than the CMBR temperature and will result in the absorption of energy from CMBR for $T_m < T_r$.

"NEGATIVE INTENSITIES"

Let us now explain what we mean by "negative intensity" (NI). Usually, when the possibility of observing an object is considered, the energy that this object

---

* E-mail address for contacts: dubr@MD1381.spb.edu

can emit is estimated. Clearly, in this case, we have in mind energy release. In the presence of external radiation, the object can also manifest itself by the absorption of this radiation. Thus, for example, foreground gas clouds on the line of sight to a point source produce absorptions in resonance atomic and molecular lines. At the same time, their intrinsic emission can be very weak, so they can ultimately be considered as "negative-intensity" objects. In this case, we observe the NI effect in narrow spectral bands. In broad bands, the NI effect is well known from the absorption of starlight by the dust component in galaxies.

It is difficult to obtain the NI effect for uniform and isotropic background radiation. The point is that, in view of the optical theorem, simple scattering does not change the CMBR isotropy and intensity. The absorption and emission of photons by matter when their temperatures are equal also changes nothing in view of the principle of detailed balancing. Therefore, as was already mentioned above, we can detect an object if the system isotropy is broken in some way or if the matter and radiation temperatures are not equal.

Anisotropy arises, for example, from the presence of peculiar velocities of primordial objects. The amplitude of the CMBR temperature distortion through the Doppler effect is given by

$$\delta T_D / T_r = \frac{V_p}{c} \tau_T. \tag{1}$$

For the Planck spectrum, the flux deviation δF can be written as

$$\delta F / F_r = x(1 - e^{-x})^{-1} \frac{\delta T}{T_r}, \tag{2}$$

where

$$x = h\nu / kT_r, \quad T_r = 2.73(1 + z) \text{ K}, \tag{3}$$

$$F_r = F_0 x^3 (e^x - 1)^{-1} (1 + z)^3. \tag{4}$$

$F_0 = 2.71 \times 10^{-15}$ erg cm^{-2} s^{-1} sr^{-1} Hz^{-1}, h is the Planck constant, ν is the frequency, and k is the Boltzmann constant. The fact that the effect is linear in velocity implies that the observed $\delta T_D / T_r$ can be positive and negative. It is important to note that this assertion is valid for any frequency. Here, the point is not that the Thomson scattering cross section does not depend on frequency; the sign of the temperature deviation is determined only by the sign of the object's radial velocity. This is a fundamental property of the Doppler effect. Thus, the NI effect can be produced in CMBR only by simple scattering without the true absorption of energy.

As was noted above, the NI formation mechanism can be the true absorption of CMBR photons. As follows from general laws of thermodynamics, this requires that the absorbing matter have a temperature

T_m lower than the radiation temperature. As matter cools down in the Universe, there comes a stage when the matter temperature ceases to be approximately equal to the radiation temperature. This is variously estimated to occur after $z = 150$. This stage lasts until the so-called secondary heating attributable to the outbursts of primordial stars. However, the number density of free electrons at this epoch is very low, and, consequently, the possible CMBR distortions are small.

We are interested in individual objects rather than in the homogeneous component of the medium. The time of a protoobject's passage to a nonlinear evolutionary stage should be considered for them. For different objects, this occurs at different times (Puy and Signore 1996; Dubrovich 1999). In this case, both the degree of ionization and the temperature of matter can differ markedly from the mean values. Below, we will assume that $T_m > T_r$.

The specific mechanism that gives rise to NI is the well-known Sunyaev–Zel'dovich effect (SZ) (Zel'dovich and Sunyaev 1969; Sunyaev and Zel'dovich 1972). Its peculiarity is that a reduction in radiation temperature results from a frequency redistribution of CMBR photons through Compton scattering by very hot electrons. This is consistent with the general laws, because the total radiation energy increases, while the decrease in intensity is only the effect of frequency redistribution of CMBR photons and manifests itself only in the Rayleigh–Jeans part of the spectrum. In the Wien wing, the intensity increases (for more details, see below).

Let us now consider what the intensity of protoobjects' radiation can be under various conditions. The expression for τ_T is

$$\tau_T = n_e \sigma_T L = 2.0 \times 10^{-6} n_e L_{pc}, \tag{5}$$

where L_{pc} is the linear size of the protoobject in parsecs, and n_e is in cm^{-3}. For free–free emission, we can write

$$F_{ff} = 1.07 F_0 n_e^2 T_m^{-1/2} e^{-\alpha x} g(x)(L/10^{24} \text{ cm}), \tag{6}$$

where

$$g(x) \approx \ln[28(T_m/10^3 \text{K})^{3/2}(1 + z)^{-1} x^{-1} + 3], \tag{7}$$

$$\alpha = 2.73(1 + z)T_m^{-1}. \tag{8}$$

All physical quantities are taken in a comoving frame of reference, i.e., at the corresponding z. The total observed flux δF from the protoobject is the sum of these two quantities, Doppler and bremsstrahlung $\delta F = F_{ff} + F_D$:

$$F_D = 1.6 F_0 x^4 e^{-x}(1 - e^{-x})^{-2}(1 + z)^3 \frac{V_p}{c} n_e (L/10^{24} \text{ cm}), \tag{9}$$

$$\delta F = \delta F_0[e^{-\alpha x}g(x)/\gamma - x^4 e^{-x}(1 - e^{-x})^{-2}] \tag{10}$$
$$= \delta F_0 f(x),$$

$$\delta F_0 = 1.6 F_0 n_e (1 + z)^3 \frac{V_p}{c}(L/10^{24} \text{ cm}), \tag{11}$$

$$\gamma = 1.4 \frac{V_p}{c} T_m^{1/2} n_e^{-1}(1 + z)^3. \tag{12}$$

The figure shows the spectrum $f(x)$ for $\alpha = 0.1$, $\gamma = 0.5, 1, 10$. It follows from Eqs. (10) and (12) that for $\gamma < 0.2$ at $\alpha < 1$, there is no NI effect at all. The peak position of the effect in frequency depends on γ and z. When the free–free radiation is small, the peak position does not depend on z and the object's parameters; it is $x_m \approx 3.8$. For a present-day observer, this corresponds to wavelength $\lambda = 1.4$ mm, i.e., it is near the peak of the CMBR intensity ($\lambda_{CMBR} = 1.88$ mm). For a small free–free contribution, the peak value of $f(x)$ is $f(x_m) = 4.88$ and depends only slightly on z. At the same time, the role of the free–free mechanism is important at the edges of the spectrum. Thus, for example, at sufficiently high electron densities, the point of sign reversal of the effect in the low- and high-frequency CMBR wings can be close to the peak of its intensity. In this case, the dependence of $f(x)$ on cloud parameters is significant and, therefore, can be used to determine some of them. Below, we consider this problem and calculate the relationship between the linear and angular sizes of objects.

ESTIMATING OBSERVABLE PARAMETERS

Let us require that the amplitude of the effect, at least at its maximum, be larger that the detection limit, $\delta F/F_r > 5 \times 10^{-6}$. This implies that $V_p/c > 10^{-6}$. On the other hand, the peculiar velocity cannot be large: $(V_p/c) < 10^{-3}$. This constrains the objects' parameters ($T_m \approx 10^3$ K):

$$n_e < 7(V_p/c)T_m^{1/2}(1 + z)^3 \text{ cm}^{-3} < 0.2(1 + z)^3 \text{ cm}^{-3}. \tag{13}$$

At the same time, from Eqs. (1), (4), (5) and from the detection limit at maximum, we obtain

$$n_e > 0.65(c/V_p)L_{pc}^{-1} \text{ cm}^{-3}. \tag{14}$$

It thus follows that the NI effect at $\delta F/F_r > 5 \times 10^{-6}$ cannot be caused by any of the known objects: H II clouds in our Galaxy, other galaxies, and the so-called Lα clouds. Indeed, $L_{pc} < 100$ for H II regions in our Galaxy; it is easy to see that either a sufficient optical depth is not reached [the condition (14) is not satisfied] or τ_T has the required value, but at the cost of a high density, $n_e > 10$ cm^{-3}, implying a sharp increase in δF_{ff} and the violation of condition (13).

The situation with intergalactic Lα clouds is not better. Their parameters $L_{pc} < 10^4$ and $n_e < 10^{-3}$ cm^{-3} result in $\tau_T < 10^{-5}$ and $\delta F_D/F_r < 10^{-8}$. Since T_e in these clouds is much higher than T_r, it is clear that the NI effect (in continuum) is out of the question. A sufficiently large
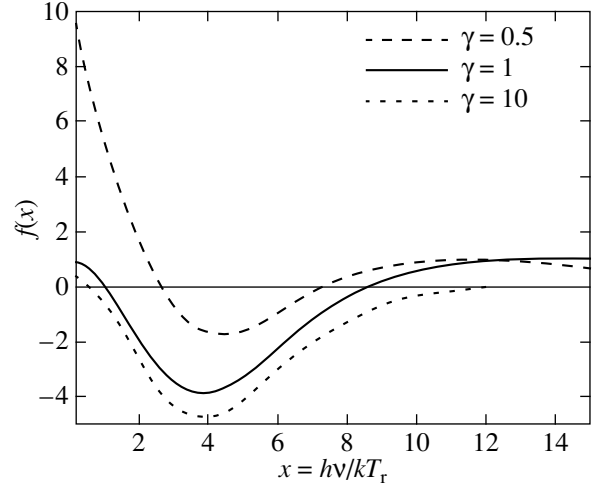
Spectrum $f(x)$ of an individual object for $\alpha = 0.1$ and various values of γ.

optical depth due to Thomson scattering could be provided by distant galaxies, but their radio and millimeter-band emission is much stronger than that required to offset δT_D.

The NI effect could be produced by an object, for example, with the following parameters: $V_p = 100$ km s^{-1}, $L = 10^{24}$ cm, $n_e = 10^{-2}$ cm^{-3}, $M = 10^{13}M_{\odot}$, and $T_e < 10^3$ K. Then, $\delta T_D/T_r \approx 5 \times 10^{-6}$. At $z \sim 2$, a cluster of galaxies could most likely be such an object. However, apart from the fact that it must definitely be visible in the radio, optical, or infrared ranges, the main problem would be associated with the mass of such an object. The point is that the above mass M was calculated based on the density of free electrons. In reality, however, the bulk of the mass in such a cluster is concentrated in galaxies and dark matter. Hence, the total mass of such a cluster would be at least two orders of magnitude larger, which is definitely impossible on scale $L = 300$ kpc.

At the same time, such parameters are quite natural for a protocluster at $z = 30$. For the Hubble constant $H_0 = 60$ km s^{-1} Mpc^{-1}, the hydrogen-to-critical density ratio $\omega_b = n_H/n_c = 0.03$, and the degree of ionization of the order of unity, we have $\delta F_D/F_r \approx 10^{-5}$. Here, the problem of mass is not critical, because such a mass at this epoch is not yet gravitationally isolated and continues to expand up to several Mpc at the present epoch. In this case, the free–free emission is insignificant for two reasons: the low n_e and the strong frequency dependence of F_r. Indeed, the currently observed F_{ff} at a given wavelength essentially corresponds to emission at a frequency that is a factor of 30 higher, where the optical depth for free–free emission is considerably smaller. This is reflected in the z dependence of the first and second terms in Eq. (10).

Thus, we can definitely assert that, except for the SZ effect, none of the known types of objects can produce

the NI effect in radio continuum. In the submillimeter wavelength range, we can discuss only the Doppler mechanism. Indeed, the frequency dependence of the SZ effect is (Zel'dovich and Sunyaev 1969; Weller *et al.* 1999)

$$\delta F_{SZ}(x) = F_0 y_c [x^4 e^{-x}/(1 - e^{-x})^2] \\ \times [x(1 + e^{-x})/(1 - e^{-x}) - 4], \tag{15}$$

where y_c is the dimensionless Compton parameter determined by the electron temperature. This expression is zero at $x = 3.8$. It is less and greater than zero at $x < 3.8$ and $x > 3.8$, respectively. The negative intensity reaches a maximum at $x = 2.3$. The positions of extrema depend on y_c, i.e., on the object's parameters and on z. For the Doppler mechanism without free–free emission, according to Eqs. (1) and (2), the sign of the effect does not depend on frequency, and the intensity deviation reaches a maximum at $x = 3.8$, i.e., where the SZ effect vanishes. In addition, in reasonable evolutionary scenarios for primordial density perturbations at $z > 30$, there is no reason to expect sufficiently high matter temperatures. Thus, in the early Universe, there is essentially only one NI formation mechanism: the Doppler mechanism.

The main problem of this mechanism is to obtain a high degree of ionization. At $z = 30$, many various ionization sources can be considered, but all of them are strongly model-dependent. Thus, for example, the model with primordial stars can provide the required degree of ionization without the strong heating of matter during the explosions of supernovae whose masses account for about 10^{-3} of the total mass of the protoobject. However, even such a number of stars at such a high z require additional hypotheses about the spectrum of primordial fluctuations on small scales. Shock waves that arise when primordial perturbations pass to a nonlinear evolutionary stage can heat up and produce secondary ionization of matter. Such shock waves can exist only in some places of the Universe, so matter will be ionized partially and in spots. In this case, the total number of regions capable of producing the NI effect can be small, and their spatial sizes depend on the parameters of primordial density fluctuations.

Among the exotic, but also most interesting sources of secondary ionization at high z, we can mention the decay of various unstable particles to produce photons with energies above 13.6 eV.

Here, we will not dwell on a comparative analysis of all these models. We only note that the z range close to the time of hydrogen recombination, i.e., corresponds to the stage of primary ionization, should be taken into account. This range is usually studied. Its advantage is a significant degree of ionization and, consequently, an appreciable optical depth τ_T. However, V_p is low in this case. At the epoch of secondary heating, the peculiar velocity is higher, and the optical depth can be large

because of strong ionization and an increase in density due to compression.

Let us now consider yet another parameter of NI objects, their angular size. An important circumstance is its strong redshift dependence. The angular size of an object (at its constant linear size L) decreases as it recedes for low z and increases for z larger than some value. Currently available observational data favor the model of a flat expanding Universe with cosmological constant Λ. In this model, the exact relations between θ and z contain parameters Ω_m and Ω_Λ (the ratio of the density of matter n_m and "vacuum" to the critical density n_c ($\Omega_m + \Omega_\Lambda = 1$) and are (Sahni and Starobinsky 1999)

$$\theta = (H_0 L/c)(1 + z)\int[\Omega_m(1 + z)^3 + \Omega_\Lambda]^{-1/2}dz. \tag{16}$$

For large z and $H_0 = 60$ km s^{-1} Mpc^{-1} h_{60}, $\Omega_m = 0.3$, we obtain

$$\theta \approx 15'' h_{60} L_{Mpc}(1 + z), \tag{17}$$

where $L_{Mpc} - L$ is in Mpc. The increase in θ proportional to z yields a very important additional method of selecting distant objects. Having detected a NI object, we can estimate the product $V_p\tau_T$ from $\delta T_{obs}/T_r$. Subsequently, in view of the weak z dependence of peculiar velocity, we can estimate τ_T to within a factor of 3 or 4, which leaves uncertainty in only two parameters: n_e and L. The relationship between L and θ is also very important here. For the same angular size of the object and approximately the same optical depth, the difference in mass M is proportional to L^2. This implies that whereas $M = 10^{11} M_\odot$ (corresponding to an ordinary protogalaxy similar to ours) is enough to produce the required temperature fluctuation at $z = 10$–15, a cluster of galaxies with the mass associated with free electrons alone (of the order of $10^{13} M_\odot$) will give such an effect at $z \sim 1$. Naturally, in the latter case, the probability that there are no significant observational manifestations in other spectral ranges (optical, X rays, or radio) is extremely low.

ADDITIONAL METHODS FOR IDENTIFYING PROTOOBJECTS

Thus, we once again make sure that the NI effect, a reduction in emission intensity relative to CMBR in the absence of any radiation in other wavelength ranges together with sufficiently large angular sizes, strongly suggests a cosmological z of this object. Naturally, these arguments give only a rough estimate of z. To determine z more accurately requires additional information. Let us consider several possibilities of searching for such information.

First, the sources of energy for reionization may be considered. They can differ in nature, but they must also have common observational manifestations. For example, the Lα hydrogen line emission strongly depends on n_e, and, hence, irrespective of the energy source, the increase in electron density by four orders

of magnitude causes a sharp increase in the number of hydrogen recombinations, which produce Lα photons. The estimated intensity of this line strongly depends on the details of the ionization: its rate, spatial distribution, and duration. Clearly, the ionization attributable to primordial stars will be highly nonuniform and distributed in spots.

The shock waves arising at a nonlinear evolutionary stage of "pancakes" will give a strong flattening of the density distribution of free electrons on large scales. If, however, the secondary ionization at some stage is determined by decay particles, then the degree of ionization will be distributed in the entire space uniformly, and the pattern of temperature fluctuations will be the same as that for primordial fluctuations. For a detailed analysis of the Lα emission distribution, we must solve the transfer equations for all these configurations. In the spectrum, this line must be in the range 1–3 μm.

The second way can be the search for any effects of a high degree of ionization. For example, such an effect can be the appearance of HeH$^+$ molecules in large quantities. Thus, if the density of free electrons sharply increases, the balance between the formation and breakup of this molecule shifts toward its higher abundance nearly linearly n_e. In the scenario with shocks (both from supernovae and in "pancakes"), an additional channel for HeH$^+$ formation in a neutral-particle reaction emerges: He + H $\longrightarrow$ HeH$^+$ + e. The required shock velocity is $\sim$30 km s^{-1}. Other molecules, H$_2^+$, H$_3^+$, HD$^+$, H$_2$D$^+$, etc., can also appear. The redshift of the objects under consideration can be determined from molecular lines. In accordance with general rules, these lines can be attributed to the intrinsic emission of hot matter and to CMBR scattering. In the latter case, their intensity can be higher than that in the former case, and they can be observed not only in emission, but also in absorption (which will also strongly suggest their cosmological origin). The wavelength range for searching these lines is from radio waves to submillimeter waves. For instance, the first molecular HeH$^+$ rotational transition has a laboratory wavelength of 149 μm, and objects with $z = 15$ will be seen at a frequency of about 125 GHz. The molecular spectrum exhibits a large number of lines, which is very important for an unambiguous redshift determination.

The third way is a detailed analysis of the spectral profile $f(x)$ in the Wien and Rayleigh–Jeans wings. At low frequencies, the contribution of bremsstrahlung dominates, which allows us to estimate the emission measure $n_e^2 L$ and to find n_e and L separately. Using expression (10), we can obtain estimates for the main characteristic points of the spectrum x_1, x_2 (the points of sign reversal of δF), and x_m (the point of the peak value of the effect):

$$x_1 \approx 2\gamma^{-1/2},$$

$$\lambda_1 \approx 0.26 \left(\frac{V_p}{100 \text{ km/s}} \right)^{1/2} (T_m/10^3 \text{ K})^{1/4}$$

$$\times \left(\frac{n_e}{0.01 \text{ cm}^{-3}} \right)^{-1/2} (1 + z)^{3/2} \text{ cm},$$

(18)

$$(1 - \alpha)x_2 - 4\ln(x_2) \approx \ln[\gamma/g(10)],$$

$$350 \, \mu\text{m} < \lambda_2 < 600 \, \mu\text{m},$$

(19)

$$x_m \approx 3.8, \quad \lambda_m \approx 1.4 \text{ mm}.$$

(20)

At high z, the point in the long-wavelength spectral region can be difficult to reach in observations, because $x_1 \ll 1$. Formally, our estimates do not depend on L, because they are determined by the form of $f(x)$ alone. Therefore, it will suffice to make four measurements at different points of the distortion profile to estimate the four independent parameters V_p, n_e, T_m, and z. The angular size yields information about L.

A further detailed study of such objects will allow us to solve many problems associated with the nonlinear evolutionary stage of primordial matter-density perturbations until the beginning of the main formation phase of primordial stars and galaxies. However, all of the aforesaid refers only to individual protoobjects. In pure form, they can exist only at the earliest stage of secondary heating, when the matter between them is not yet ionized. After the onset of mass star formation and after complete reionization of the Universe, the CMBR distortion effects must be considered with allowance for the superposition of different objects on the line of sight. In this case, the statistical properties of matter-density fluctuations become crucially important. This problem is a result of the broadband character of Thomson scattering.

In the case of scattering in molecular lines, different objects falling on the same line of sight can be independently identified due to the narrowness of spectral lines (Dubrovich 1997).

Strictly speaking, yet another mechanism of NI formation in CMBR, the Sachs–Wolfe effect (Sachs and Wolfe 1967), should be considered, because it is also linear in metric distortions. As in the case of the Doppler mechanism, there is no frequency dependence of δI due to this effect. Moreover, since, in this case, the distortion of the radiation field does not depend on the physical state of matter, it can be, in particular, completely neutral, and there will be no free–free emission. In this case, the NI effect will be observed in all wavelength ranges. However, for small-scale fluctuations, it is very difficult to obtain an appreciable amplitude of the effect. There may be some ways of a rapid change in metric fluctuations on small scales. For the negative CMBR temperature distortions to arise, there must be such processes as very fast collapse of a large mass without considerable Thomson scattering. Most likely,

such behavior may be expected for the dark matter in the Universe or for fluctuations in some fields.

ACKNOWLEDGMENTS

REFERENCES

1. V. K. Dubrovich, Pis'ma Astron. Zh. **3**, 128 (1977) [Sov. Astron. Lett. **3**, 128 (1977)].
2. V. K. Dubrovich, Astron. Astrophys. **324**, 27 (1997).
3. V. K. Dubrovich, Gravit. Cosmol. **5**, 171 (1999).
4. D. Puy and M. Signore, Astron. Astrophys. **305**, 371 (1996).
5. R. K. Sachs and A. M. Wolfe, Astrophys. J. **147**, 73 (1967).
6. V. Sahni and A. Starobinsky, astro-ph/9904398 (1999).
7. R. A. Sunyaev and Ya. B. Zel'dovich, Comments Astrophys. Space Phys. **4**, 173 (1972).
8. R. A. Sunyaev and Ya. B. Zel'dovich, Mon. Not. R. Astron. Soc. **190**, 413 (1980).
9. J. Weller, R. A. Battye, and A. Albrecht, Phys. Rev. D **60**, 103520 (1999).
10. Ya. B. Zel'dovich and R. A. Sunyaev, Astrophys. Space Sci. **4**, 301 (1969).

Translated by G. Rudnitskiĭ

Rotation Curves for 135 Edge-on Galaxies

D. I. Makarov[1]*, A. N. Burenkov[1], and N. V. Tyurina[2]

[1] *Special Astrophysical Observatory, Russian Academy of Sciences, pos. Nizhniĭ Arkhyz, Stavropol kraĭ, 357147 Russia*
[2] *Moscow State University, Vorob'evy gory, Moscow, 119899 Russia*

Received September 21, 2000

Abstract—We summarize the results of our survey of rotation curves for edge-on galaxies. The observations were carried out with the 6-m Special Astrophysical Observatory telescope. Over the four years of our observations, we obtained spectra for 306 galaxies from the FGC catalog (Karachentsev *et al.* 1993). Rotation curves and radial velocities are given for 135 galaxies. The median radial velocity of the galaxies studied is 7800 km s^{-1}. Together with the observations performed by other authors with different instruments, this survey allowed us to produce a homogeneous sample of edge-on galaxies from the RFGC catalog (Karachentsev *et al.* 1999) uniformly distributed over the entire sky and to analyze the velocity field of galaxies on scales up to 100 Mpc. © 2001 MAIK "Nauka/Interperiodica".

Key words: *galaxies, groups and clusters of galaxies, intergalactic gas*

INTRODUCTION

This article completes our series of papers (Makarov *et al.* 1997a, 1997b, 1999) in which we published the observations of rotation curves for edge-on galaxies from the FGC catalog (Karachentsev *et al.* 1993). Here, we present data for 135 galaxies. The work was begun in 1995 in an effort to study the peculiar velocity field by using a sample of FGC edge-on galaxies (Karachentsev *et al.* 1993). Over this period, we obtained spectra for 306 galaxies. Our survey significantly increased the number of FGC galaxies with measured redshifts and rotation amplitudes in the northern sky. Thus, for example, 153 galaxies with radio observations (Karachentsev *et al.* 1995) and only 45 galaxies with optical rotation curves (Karachentsev and Zhou Xu 1991) were known by 1995. Given the observations of other authors, the full list of FGC galaxies with measured radial velocities and rotation amplitudes currently numbers 1327 galaxies (Karachentsev *et al.* 2000b).

FGC CATALOG

The Flat Galaxy Catalog (FGC) (Karachentsev *et al.* 1993), which has recently been improved and enlarged (RFGC) (Karachentsev *et al.* 1999), was specially compiled to study large-scale coherent motions. It covers the entire sky and contains 4236 spirals with axial ratios $a/b > 7$ and angular sizes of their major axes $a > 0\rlap{.}'6$. As was shown by Heidmann *et al.* (1971), such galaxies occupy a narrow Sc–Sd interval in the Hubble morpho-

logical sequence. They are easily distinguishable from other objects at large distances. All late-type spirals are rich in gas and are reliably detected in the H I line. These galaxies show a close correlation between hydrogen-line profile width and linear diameter, which allows their distances to be determined without performing detailed photometry (Karachentsev *et al.* 1995). Besides, their rotation amplitudes require no correction for galaxy inclination, which allows the associated errors to be avoided. Edge-on galaxies were generally excluded from consideration to avoid the unpredictable effects of internal absorption in their equatorial regions. For this reason, the sample of FGC galaxies overlaps only slightly with other samples of galaxies used to investigate large-scale motions.

Further studies (Karachentsev *et al.* 1997; Kudrya *et al.* 1997) have shown that the FGC catalog is highly homogeneous and complete, which makes it one of the best available samples for investigating large-scale motions. To this end, about 700 FGC galaxies with declinations from 0° to +38° were observed in the 21-cm H I line with the Arecibo radio telescope. Redshifts and H I line widths were measured for 590 flat galaxies (Giovanelli *et al.* 1997), which allowed their distances to be determined by the Tully–Fisher method. These data were used to estimate the amplitude and direction of the bulk motion of galaxies with respect to the cosmic microwave background (Karachentsev *et al.* 1995, 2000a). These studies revealed bulk motions of FGC galaxies with an amplitude of 300 ± 80 km s^{-1} on scales of the order of 100 Mpc toward the concentration of rich Shapley clusters.

In the course of these studies, it became clear that for the solution to be more stable, the number of galaxies with measured radial velocities and rotation ampli-
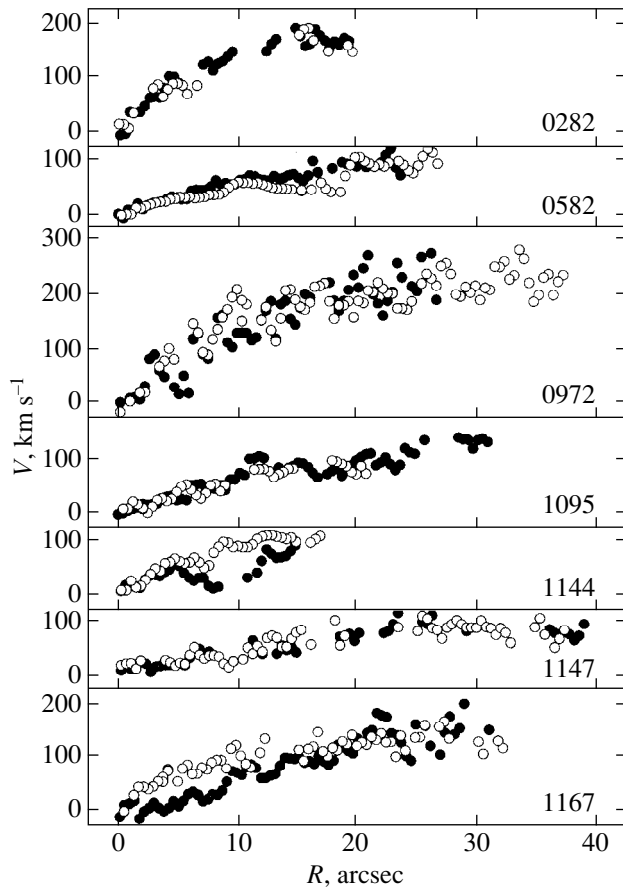
Fig. 1. Sample rotation curves from our survey. The receding and approaching sides of the galaxy are indicated by filled and open circles, respectively. RFGC galaxy numbers (Karachentsev *et al.* 1999) are shown in the lower right corner.

tudes outside the Arecibo zone should be increased. Since the observational problem was complex and since there were virtually no suitable radio telescopes in the northern hemisphere, we opted for an optical study of these galaxies.

OBSERVATIONS

For our observations, we selected northern-sky galaxies at $\delta > +38°$ of the 1st and 2nd surface-brightness indices (according to the FGC classification) with apparent axial ratios $a/b > 8$ and major axes in the range $0\rlap{.}'6 < a < 2'$. The lower and upper limits on the sizes are associated with the FGC limit and the spectrograph slit length, respectively. The observations were carried out with the 6-m Special Astrophysical Observatory telescope by using a fast prime-focus spectrograph (Afanas'ev *et al.* 1995). A 530×580 CCD camera in combination with a 1302 line mm^{-1} grating provided a reciprocal linear dispersion of 1.5 Å pixel^{-1} near Hα with a spectral resolution of 3 Å and a spatial resolution of $0\rlap{.}''4$ pixel^{-1}.

In each case, the spectrograph slit was oriented along the galactic major axis with an accuracy of $1°-2°$. For most objects, we obtained two spectra for each galaxy with a typical exposure time of 15 min, which facilitated the removal of cosmic-ray-particle hits. Comparison spectra were generally taken between galaxy exposures.

The survey was carried out from the second half of 1995 until the second half of 1999. Over this period, we obtained spectra for 306 galaxies. The observational program was 94% complete.

The data reduction included a standard sequence of CCD image reduction and a construction of the dispersion curve from a comparison spectrum. The galactic rotation curves were measured by using the Hα emission line, which dominated in brightness in all the observed flat galaxies. The line profile was fitted with a Gaussian. The mean error in the radial velocity did not exceed ~15 km s^{-1}. The position of the galactic center was determined from the continuum intensity profile or from symmetry of the receding and approaching sides of the galaxy without a distinct nucleus. We estimated the amplitude V_{max} from the maximum of a smoothed rotation curve. The computations were performed by means of the MIDAS package with the LONG context, which is used to reduce data from long-slit spectrographs.

RESULTS

Sample rotation curves are shown in Fig. 1. The galactocentric distance and the radial velocity relative to the center are plotted along the horizontal and vertical axes, respectively. Detailed information can be retrieved via E-mail (dim@sao.ru).

Our observational data are summarized in the table[1], which gives the following parameters for each galaxy:

(1) RFGC, FGC, and PGC numbers in the RFGC (Karachentsev *et al.* 1999), FGC (Karachentsev *et al.* 1993), and PGC (Paturel *et al.* 1996) catalogs, respectively;

(2) Angular diameter a along the major axis, in arcminutes, measured on blue Palomar Observatory Sky Survey maps and reduced to the standard 25 mag arcsec^{-2} isophote;

(3) Axial ratio a/b;

(4) Heliocentric radial velocity V_h;

(5) Rotation amplitude V_{max};

(6) Position angle of the galaxy's receding side *PA*;

(7) Extent of the measured segment on the rotation curve, in fractions of the standard galaxy radius R_V/R_{25}.

As has been repeatedly pointed out (Makarov *et al.* 1997a, 1997b, 1999), the observations of thin, edge-on galaxies are highly efficient. Only in two cases did we

---

[1] The table is published in electronic form only and is accessible via ftp cdsarc.u-strasbg.fr/pub/cats/J (130.79.128.5) or http://cdsweb.u-strasbg.fr/pub/cats/J.
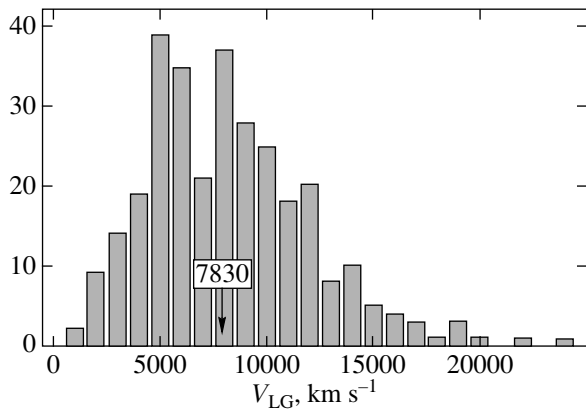
Fig. 2. Histogram of radial velocities corrected for the motion of the Local Group. The arrow indicates the median value $V_{LG} = 7830$ km s^{-1}.
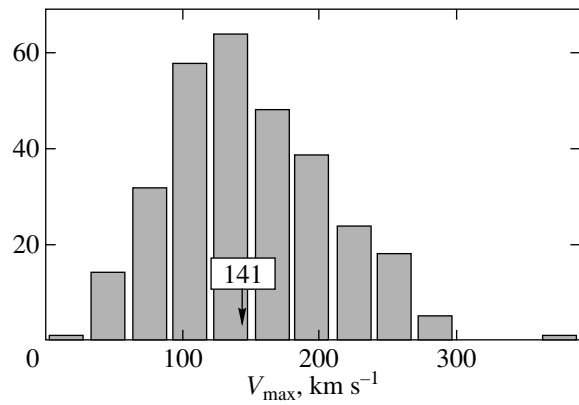

Fig. 3. Histogram of rotation amplitudes. The median values $V_{max} = 141$ km s^{-1} is indicated by the arrow.

fail to determine parameters of the galactic rotation curve. For more than 95% of the FGC objects, the contrast of the Hα emission line above the night-sky spectrum is high enough to measure a typical galaxy rotation amplitude with an error of ~10%, which is acceptable for studying large-scale motions.

The extent of the rotation curve for different galaxies lies in the range 0.45–1.45 with a median value of 0.87 of the standard radius for a flat galaxy. The rotation curve is flat or ascending virtually for all galaxies, which appears typical of isolated galaxies.

The rotation curves for several edge-on galaxies are wavy in pattern with a typical velocity difference of ~50 km s^{-1}. In some cases, there is a distinct asymmetry between the approaching and receding sides of the galaxy. These peculiarities are probably attributable to the high extinction in the plane of the galactic spiral arms crossed by the line of sight at small angles.

Nevertheless, as was noted (Makarov *et al.* 1997a), there is a close correlation between hydrogen line width and rotation amplitude near Hα with the standard deviation $\sigma(V_{max})$ of a mere 11.7 km s^{-1}.

The median radial velocity corrected for motion of the Local Group is 7830 km s^{-1} (see Fig. 2). The galaxies studied are generally massive spirals with a median value of the rotation-curve maximum of about 140 km s^{-1}. The distribution of galaxies in rotation amplitude V_{max} is shown in Fig. 3.

CONCLUSION

Karachentsev *et al.* (2000a) estimated parameters of the bulk motion for FGC galaxies and mapped the distribution of peculiar velocities. Their analysis involved 983 galaxies, including those observed in our survey. In the frame of reference associated with the cosmic microwave background, the bulk motions of FGC galaxies are characterized by velocity $V = 300 \pm 75$ km s^{-1} in the direction $\{l = 328°, b = +7°\}$ with an error of $\pm15°$. The best agreement, both in magnitude and in direction of

the bulk motion, is observed with the data $\{370$ km s^{-1}, $305°, +14°\}$ obtained by analyzing the Mark III galaxy sample (Dekel *et al.* 1999). It should be emphasized that the RFGC sample (Karachentsev *et al.* 1999) contains no objects common to the Mark III sample (Willick *et al.* 1997).

The complete RFGC sample of the galaxies with measured redshifts and rotation amplitudes was published by Karachentsev *et al.* (2000b).

REFERENCES

1. V. L. Afanas'ev, N. A. Burenkov, V. V. Vlasyuk, and S. V. Drabek, Otchet SAO, No. 234 (1995).
2. A. Dekel, A. Eldar, T. Kolatt, *et al.*, Astrophys. J. **522**, 1 (1999).
3. R. Giovanelli, E. Avera, and I. Karachentsev, Astron. J. **114**, 122 (1997).
4. J. Heidmann, N. Heidmann, and G. de Vaucouleurs, Mem. R. Astron. Soc. **75**, 85 (1971).
5. I. D. Karachentsev and Zhou Xu, Pis'ma Astron. Zh. **17**, 321 (1991) [Sov. Astron. Lett. **17**, 135 (1991)].
6. I. D. Karachentsev, V. E. Karachentseva, and S. L. Parnovsky, Astron. Nachr. **314**, 97 (1993).
7. I. D. Karachentsev, V. E. Karachentseva, Yu. N. Kudrya, and S. L. Parnovsky, Astron. Nachr. **316**, 369 (1995).
8. I. D. Karachentsev, V. E. Karachentseva, Yu. N. Kudrya, and S. L. Parnovsky, Pis'ma Astron. Zh. **23**, 652 (1997) [Astron. Lett. **23**, 573 (1997)].
9. I. D. Karachentsev, V. E. Karachentseva, Yu. N. Kudrya, *et al.*, Bull. Spec. Astrophys. Obs. **47**, 5 (1999).
10. I. D. Karachentsev, V. E. Karachentseva, Yu. N. Kudrya, and S. L. Parnovsky, Astron. Zh. **77**, 175 (2000a) [Astron. Rep. **44**, 150 (2000a)].

11. I. D. Karachentsev, V. E. Karachentseva, Yu. N. Kudrya, *et al.*, Bull. Spec. Astrophys. Obs. **50** (2000b) (in press).

12. Yu. N. Kudrya, I. D. Karachentsev, V. E. Karachentseva, and S. L. Parnovsky, Pis'ma Astron. Zh. **23**, 15 (1997) [Astron. Rep. **23**, 573 (1997)].

13. D. I. Makarov, I. D. Karachentsev, N. V. Tyurina, and S. S. Kaĭsin, Pis'ma Astron. Zh. **23**, 509 (1997a) [Astron. Lett. **23**, 445 (1997a)].

14. D. I. Makarov, I. D. Karachentsev, A. N. Burenkov, *et al.*, Pis'ma Astron. Zh. **23**, 736 (1997b) [Astron. Lett. **23**, 638 (1997b)].

15. D. I. Makarov, A. N. Burenkov, and N. V. Tyurina, Pis'ma Astron. Zh. **25**, 813 (1999) [Astron. Lett. **25**, 706 (1999)].

16. G. Paturel, L. Bottinelli, H. Di Nella, N. Durand, R. Garnier, L. Gouguenheim, M. C. Marthinet, C. Petit, J. Rousseau, G. Theureau, and I. Vauglin, *Principal Galaxy Catalogue: PGC-ROM* (Observatorie de Lyon, Saint-Genis Laval, 1996).

17. J. A. Willick, S. Courteau, S. M. Faber, *et al.*, Astrophys. J., Suppl. Ser. **109**, 333 (1997).

Translated by V. Astakhov

Combined Color Indices and Photometric Structures of the Galaxies NGC 834 and NGC 1134

D. V. Bizyaev[1]*, A. V. Zasov[1], and S. S. Kaĭsin[2]

[1] *Sternberg Astronomical Institute, Universitetskiĭ pr. 13, Moscow, 119899 Russia*
[2] *Special Astrophysical Observatory, Russian Academy of Sciences, pos. Nizhniĭ Arkhyz, Stavropol kraĭ, 357147 Russia*

Abstract—Surface *BVRI* photometry is presented for two spiral galaxies with a complex photometric structure: NGC 834 and NGC 1134. We propose to introduce the combined color indices Q_{BVI} and Q_{VRI} to investigate the photometric structure of the galaxies. These color indices depend only slightly on selective absorption, which allows them to be used to study the photometric structure of "dusty" galaxies. Evolutionary stellar-population models show that Q_{BVI} is most sensitive to the presence of blue stars, while Q_{VRI} depends on local Hα equivalent width. A ring with active star formation manifests itself on the Q_{BVI} map for NGC 834 at a distance of ~15″ from its center, and a spiral structure shows up on the Q_{VRI} map for NGC 1134 in its inner region. The Q_{BVI}–Q_{VRI} diagram can provide information about the current stage of a star's formation in various galactic regions. A comparison of the color indices for the galaxies with their model values allows us to estimate the color excesses and extinction in various galactic regions. © 2001 MAIK "Nauka/Interperiodica".

Key words: *galactic photometry, galactic extinction*

INTRODUCTION

Here, we analyze multicolor photometry for two spiral galaxies, NGC 834 and NGC 1134, with a complex photometric structure. NGC 834 is an isolated Sbc galaxy with a high surface brightness and bright regions distinguishable in its central part (see Fig. 1a). Since our observations are restricted only to the inner galactic regions, we give photographs from the Digital Sky Survey. NGC 834 has no close neighbors. NGC 1134 is an Sb galaxy with a highly inclined disk. A rounded inner part and a weak outer extension of the spiral structure stand out in this galaxy. For this reason, the galaxy resembles Saturn with a ring on overexposed DSS-I images (see Fig. 1b). It was included in Arp's catalog (Arp 200) in the group of "material ejected from nuclei" objects and has a small and distant companion about 7′ to the south.

Images of both galaxies exhibit dark regions, which suggest a nonuniformly distributed absorbing medium. Basic parameters of the galaxies (D_{25} from the RC3 catalog, as well as the position angles and inclinations estimated here) and the assumed distances to them for $H_0 = 75$ km s^{-1} Mpc^{-1} are given in Table 1.

Selective absorption complicates the pattern of brightness and color distribution in a galaxy. If it is observed only in two photometric bands, then the role of the dust medium cannot be taken into account in principle without invoking additional information about its stellar population. The uncertainty introduced by selective absorption can be significantly reduced by using three or more photometric bands (two or more color indices).

Although the problem of restoring extinction-corrected color indices is yet to be solved and requires a model approach, the color properties of various galactic regions can be revealed by choosing a color parameter: a combination of two color indices that depend weakly on selective absorption. Zasov and Moiseev (1998, below referred to as ZM98) proposed to use a combined index Q_{VRI} to study the structure of the spiral galaxy NGC 972. As was shown in ZM98, its value depends only slightly on whether we observe the sources through a dust "screen" or the dust and stars are uniformly mixed; it also weakly depends on the heavy-element abundances in stars.

A combination of color indices was also used by Vansevicius (1999) to study the structure of M 51.

In general, having observations in three photometric bands (*A*, *B*, and *C*), we can define the combined index as

$$Q_{ABC} = (A-B) - \frac{E_{AB}}{E_{BC}}(B-C) \qquad (1)$$

or as

$$Q_{ABC} = (A-B) - \frac{E_{AB}}{E_{AC}}(A-C), \qquad (2)$$

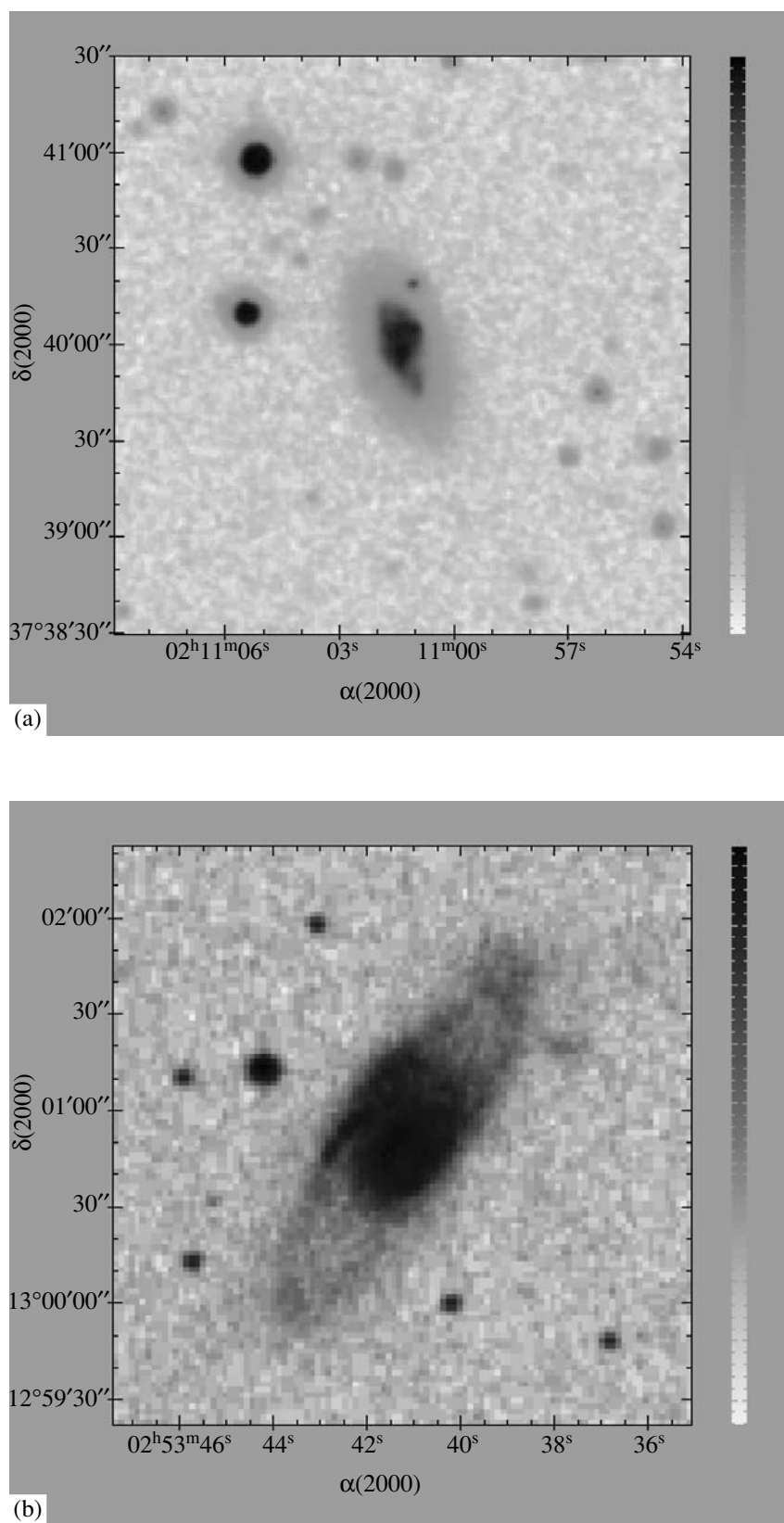
* E-mail address for contacts: dmbiz@sai.msu.ru

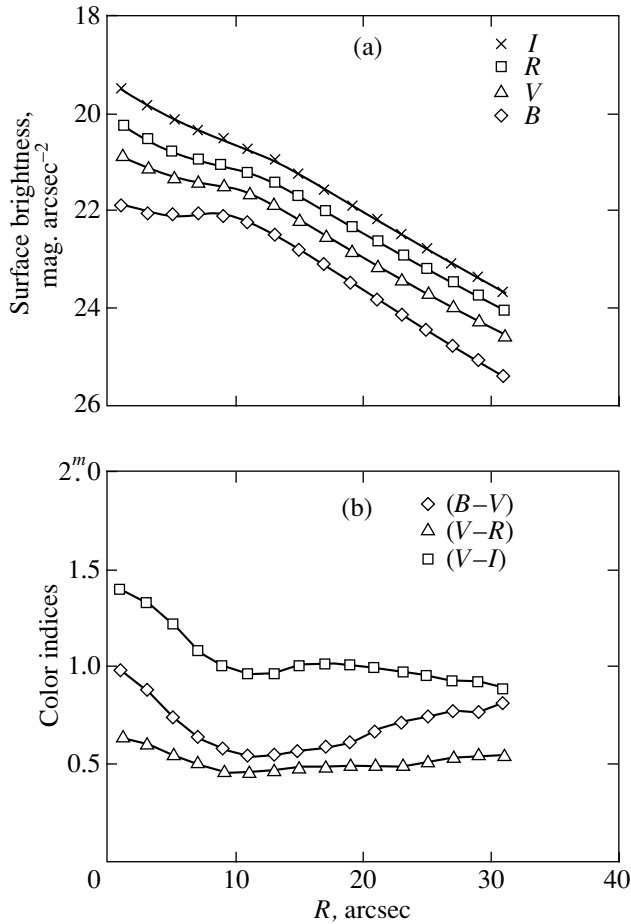**Fig. 1.** Digital Sky Survey images of (a) NGC 834 and (b) NGC 1134.

Fig. 2. *BVRI* surface brightness and color profiles for NGC 834, azimuthally averaged over ellipses. The data were not corrected for galaxy inclination to the line of sight.
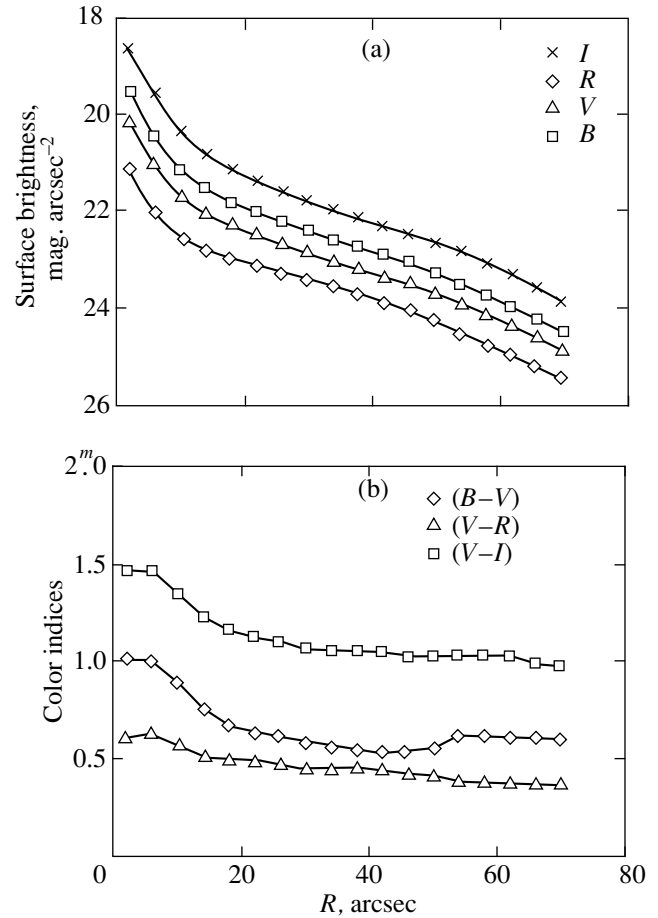

Fig. 3. Same as Fig. 2 for NGC 1134.

where $(A–B)$, $(A–C)$, and $(B–C)$ are the color indices; and E_{AB}, E_{BC}, and E_{AC} are the color excesses. The only assumption made in this case involves using the ratios of color excesses derived for our Galaxy. In general, the optical properties of dust in other galaxies can be different. However, except for the ultraviolet band (which we do not consider here), there is no reason to believe (at least for the nearest galaxies) that these differences are significant (see, e.g., Elmegreen 1980; Clayton and Martin 1985).

Following Cardelli *et al.* (1989), we take the following values for the ratios of color excesses for the *BVRI* bands:

$$\frac{E_{BV}}{E_{VI}} = 0.84, \quad \frac{E_{VR}}{E_{VI}} = 0.41,$$

$$\frac{E_{BV}}{E_{VR}} = 2.03, \quad \frac{E_{BR}}{E_{BI}} = 0.68.$$

Generalizing the results of ZM98 to the *BVRI* photometric bands, we can verify that the combined param-

eters for a "dust screen" and "uniformly mixed stars and dust" differ by no more than 10%.

OBSERVATIONS AND DATA REDUCTION

The two spiral galaxies, NGC 834 and NGC 1134, were observed in the (Cousins) *BVRI* bands on January 21 and 22, 1998, with the 1-m Special Astrophysical Observatory (SAO) telescope. The detector was a standard photometer with a 512×512 CCD array; the resolution was 0.28×0.37 arcsec per pixel. In each band,

Table 1. Orientation and assumed distances for NGC 834 and NGC 1134

Parameter	NGC 834	NGC 1134
Distance, Mpc	64.4	48.7
Angular diameter D_{25}, arcsec	67	151
Position angle, deg	28.4	151.0
Galaxy inclination, deg	59	73

0.60   (V–I)   1.4

0.40   (B–V)   1.4
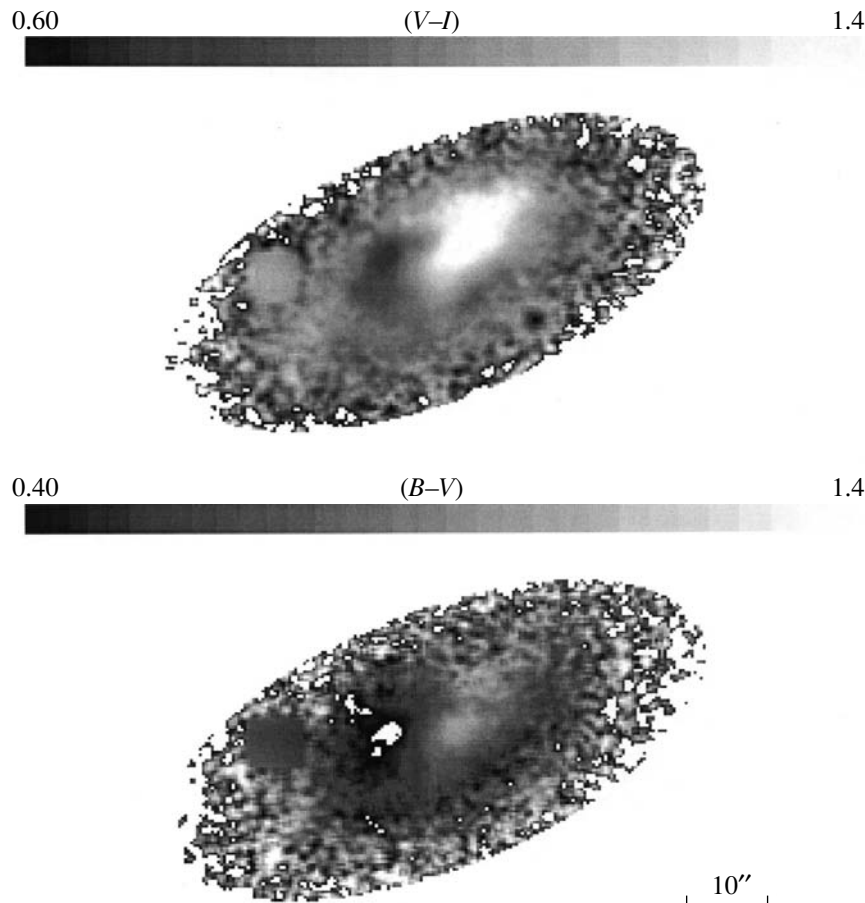

10″

Fig. 4. (V–I) and (B–V) color maps for NGC 834. The galaxy images are bounded by ellipses with major axes equal to D_{25} (from the RC3 catalog), oriented in accordance with the inferred position angle and inclination of the disk plane to the line of sight.

we obtained three images for each of the galaxies, which were slightly displaced to reduce the effect of CCD defects on the image quality. The standard reduction procedure (dark-current and bias subtraction, flat fielding, and the addition of three images for each galaxy) was performed with the MIDAS software package.

The images were calibrated by using Landolt's photometric standards, which were imaged on each night. Integrated B, V photometry for NGC 834 with circular apertures is given in Buta (1996). A comparison with our estimates shows that the V magnitudes through the corresponding aperture coincide, within $0.^{m}01$, while the B magnitudes differ by $0.^{m}23$ (for a 65″8 aperture). This difference apparently stems from the fact that the systematic error due to a light inhomogeneous haze could arise during our observations. We therefore added a free term to the color equation for B, derived from standard stars, which brings our estimates in this color band into correspondence to those of Buta (1996).

All the photometric data given below were corrected for selective absorption in our Galaxy. Following LEDA (Lyon-Meudon Extragalactic Database), we assumed the extinction in B for NGC 834 and NGC 1134 to be $0.^{m}42$ and $0.^{m}35$, respectively.

We determined the inclinations and position angles of the galaxies by using procedures from the SURFPHOT package in MIDAS. Their values are listed in Table 1.

Figures 2 and 3 show the galaxy *BVRI* surface brightness profiles azimuthally averaged over ellipses. The profiles were not corrected for the galaxy inclination to the line of sight. The reduction in brightness rise to the NGC 834 center (Fig. 2), which is particularly noticeable in the blue, suggests that the central galactic regions (R < 10″) are very dusty. Further from the center, the disk surface brightness profile is well described by an exponential law with a radial scale of 7″.

In contrast to NGC 834, the photometric profile of NGC 1134 suggests the existence of a distinct bulge. The radial brightness distribution in the bulge was assumed to follow the King profile $[I(r) = I_0 / \left(1 + \dfrac{r}{a_b}\right)^2$ with central surface brightness I_0 and characteristic radius a_b]. Separating the photometric components into

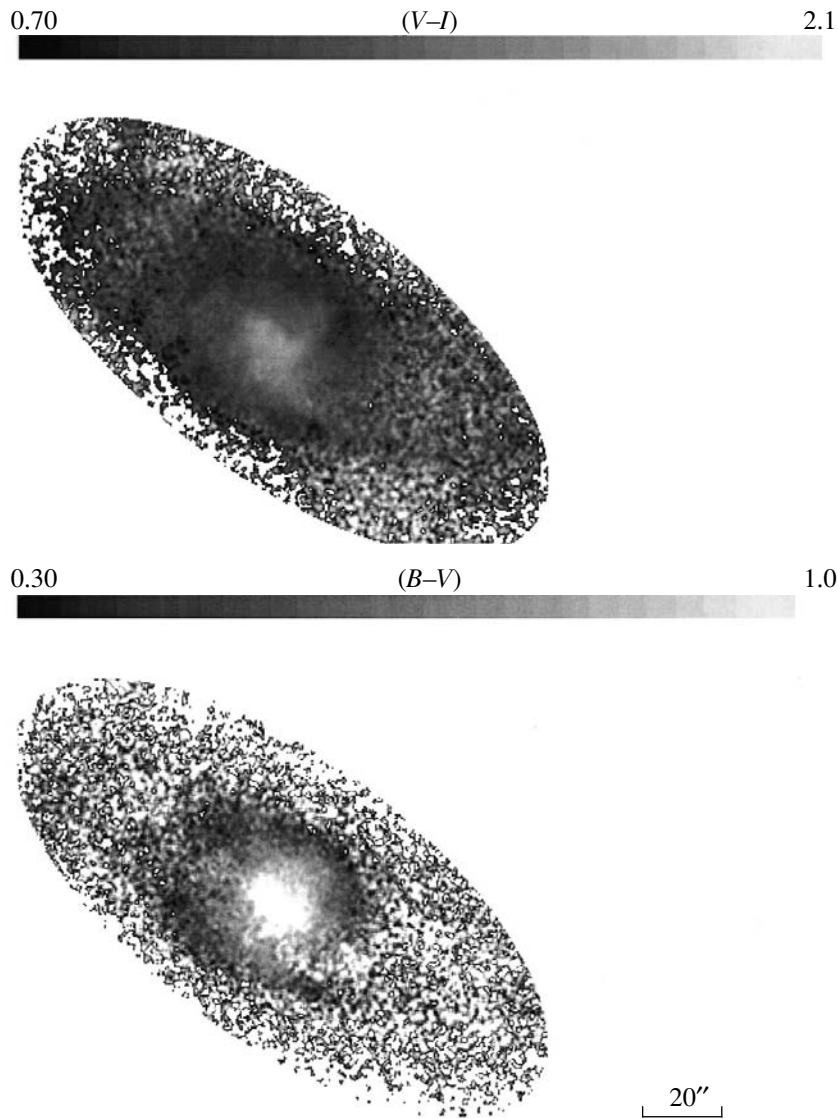0.70   (V–I)   2.1

0.30   (B–V)   1.0

20″

Fig. 5. Same as Fig. 4 for NGC 1134.

a bulge and an exponential disk yields a radial disk scale of about 24″, or 5.7 kpc. Despite the significant inclination of the disk to the line of sight, its central B surface brightness is $22{.}^{m}2$ arcsec^{-2} (without correction for the projection), which allows NGC 1134 to be classified as a galaxy of reduced surface brightness.

The photometric parameters of the components in the galaxies under consideration estimated by decom-

Table 2. Photometric parameters for NGC 834 and NGC 1134

| Parameter	NGC 834	NGC 1134
Radial disk scale in B, arcsec	6.7	25.3
Same in kpc	2.0	6.0
Disk central B surface brightness, mag. arcsec^{-2}	20.40	22.21
Bulge parameter a_b in B, arcsec	–	1.14
Bulge central B surface brightness I_0, mag. arcsec^{-2}	–	20.00
Radial disk scale in I, arcsec	7.2	22.2
Same in kpc	2.1	5.2
Disk central I surface brightness, mag. arcsec^{-2}	18.99	20.54
Bulge parameter a_b in I, arcsec	–	2.80
Bulge central I surface brightness I_0, mag. arcsec^{-2}	–	18.31
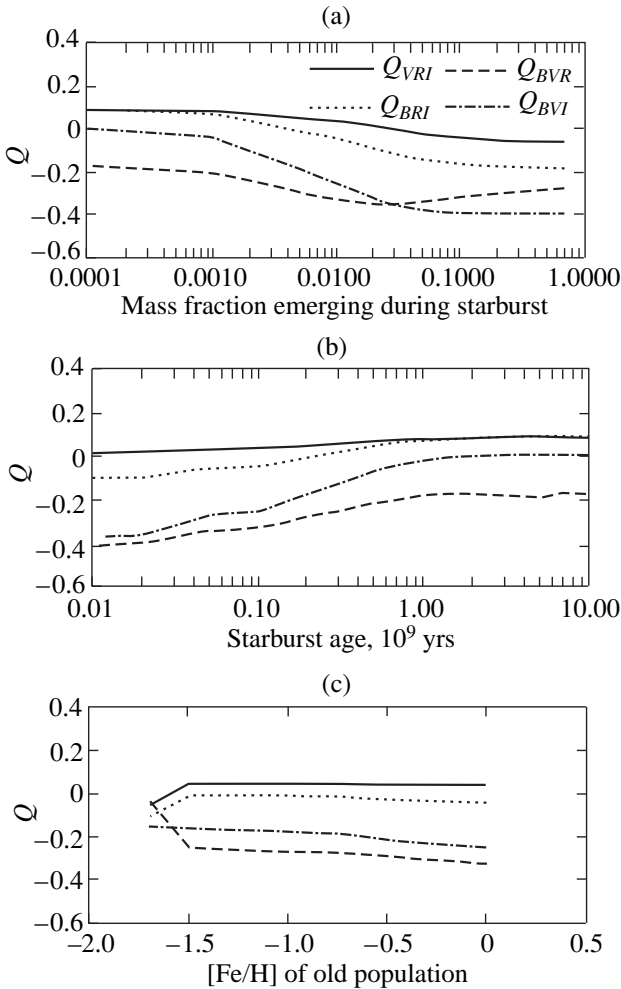
Fig. 6. (a) Model indices Q_{BVI}, Q_{BVR}, Q_{BRI}, and Q_{VRI} versus relative mass of a young stellar population with age $t = 100$ Myr; (b) various indices Q for the stellar-population models under consideration versus age of the young stellar population for its fixed relative mass (0.01 of the total mass of the stars); and (c) model indices Q versus metallicity of an old stellar population. The metallicity of young stars in all models was assumed to be solar.

posing the brightness profiles radially averaged in elliptical isophotes are given in Table 2.

The (B–V) and (V–I) color maps are shown in Figs. 4 and 5 for NGC 834 and NGC 1134, respectively. The galaxy images are bounded by ellipses with major axes D_{25} (from the RC3 catalog). The color distributions are asymmetric, which is apparently attributable to the fact that the galaxies, especially NGC 834, are dusty.

COMBINED COLOR INDICES

The combined color indices Q_{ABC} defined by Eqs. (1) and (2) are neither the real colors nor the quantities that characterize selective absorption. According to ZM98, Q_{VRI} constructed from Eq. (2) depends on the stellar-population composition and on the presence of Hα

emission and varies only slightly with stellar-population metallicity.

In order to ascertain how the indices Q change in the presence of young stars formed during a starburst, we considered several simple stellar-population models composed of a mixture of the populations of two ages: an old one with age $t = 13$ Ga and a younger one. Model color estimates were obtained by using the code of Worthey (1994). This code models the colors of a stellar population and is accessible via the Web. We assumed a Salpeter initial mass function for the stars (α = 2.35).

In Fig. 6a, model parameters Q_{BVI}, Q_{BVR}, Q_{BRI} [given by Eq. (1)], and Q_{VRI} [given by Eq. (2)] are plotted along the vertical axis, and the relative mass of a young stellar population with age $t = 100$ Myr is plotted along the horizontal axis. Figure 6b shows a plot of Q against age of the stellar population for its fixed relative mass (0.01 of the total stellar-population mass). Finally, Fig. 6c shows a plot of Q against metallicity of the old stellar population. In this case, the metallicity of young stars in all models was assumed to be solar.

We see from Fig. 6 that of all the indices Q considered, Q_{BVI} is most sensitive to the presence of young stars and to the starburst age, while the change in Q_{VRI} is smaller than that in other indices. On the other hand, Q_{VRI} helps localize Hα emission regions, because emission in this line can give an appreciable contribution in R. Figure 6c confirms the weak dependence of combined color indices on stellar metallicity.

The Q_{BVI} and Q_{VRI} maps for the galaxies under study are shown in Figs. 7 and 8. As one might expect, they appear more symmetric than the color maps in Figs. 4 and 5. A ring-shaped region ~15″ (4.7 kpc) in radius is clearly distinguishable on the Q_{BVI} maps for NGC 834. The reduced Q_{BVI} in the ring suggests that the percentage of blue stars there is higher than that in the outer and inner galactic regions (except for the region immediately adjacent to the nucleus).

Curiously, the ring does not show up on the color maps, clearly because of substantial dust absorption. For the same reason, the ring is indistinct in the direct images of the galaxy: NGC 834 was not included in the catalog of ring galaxies by Buta and Crocker (1993).

It follows from Fig. 7 that the central and blue-ring regions have similar Q_{BVI}, suggesting that the percentage of young stars in these regions is approximately the same. The difference in Q_{VRI} between the ring and central regions can be explained by the presence of brighter Hα emission sources in the ring.

A spiral structure (indistinguishable on ordinary photographs) shows up on the Q_{VRI} map in the inner region of NGC 1134. Q_{VRI} is enhanced in the spiral regions, which can be explained by the local increase in Hα emission intensity (the required equivalent width is $W_{Hα} \sim 100$ Å). Curiously, the enhancement of emission from young blue stars in these spirals is less pronounced than that of Hα emission, because the spiral arms are indistinguishable on the Q_{BVI} map.
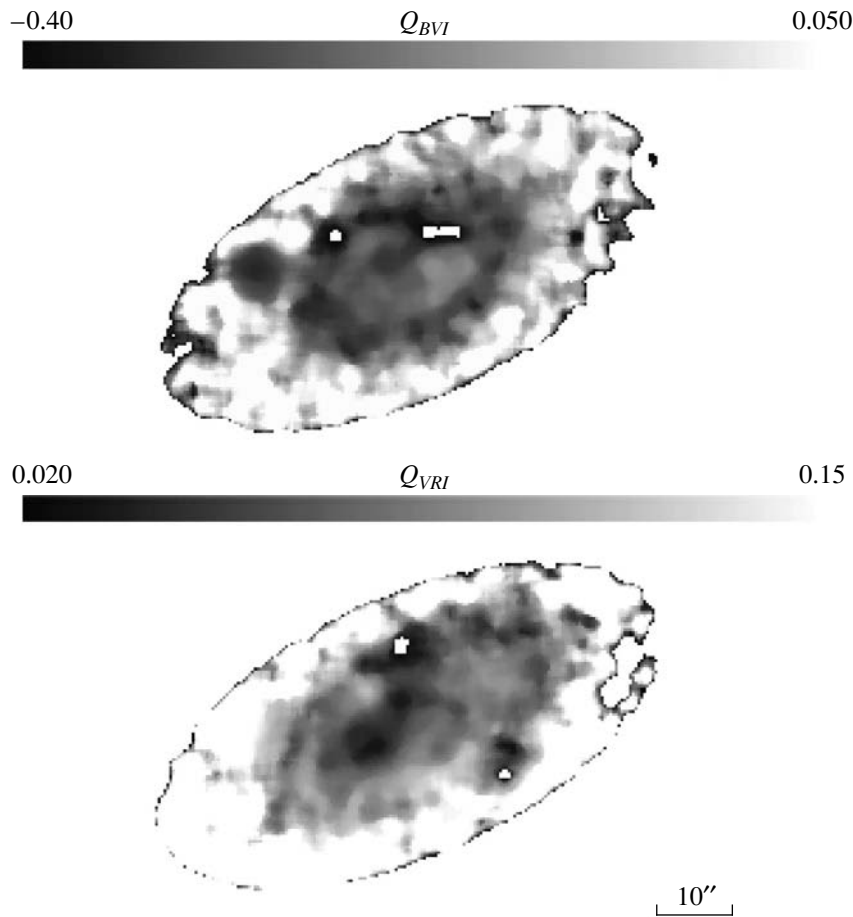
Fig. 7. Maps of combined color indices Q_{BVI} and Q_{VRI} for NGC 834.

Note that the star-forming regions distinguished by a reduced Q_{BVI}, which reflects the presence of blue stars, do not all manifest themselves in Hα (by Q_{VRI}). A similar result was previously obtained in ZM98 for another dusty spiral galaxy: NGC 972. This difference in the photometric properties of star-forming regions can be attributed both to a difference in the initial mass functions (Hα emission is produced by the most massive stars) and to the fact that the star-formation rate in regions indistinguishable in Hα dropped about 10^7 yrs ago (the lifetime of gas-ionizing stars); i.e., these regions are at a post-starburst stage.

It is convenient to simultaneously compare the photometric data for a galaxy with model values in four photometric bands on a Q_{VRI}–Q_{BVI} diagram. This diagram is similar for both galaxies. For NGC 834, however, it is more revealing, because the difference between Q for different galactic regions is larger for this diagram. The positions of these NGC 834 regions on the diagram are indicated by different symbols in Fig. 9.

Since the combined indices, inferred from more than 100 pixels, correspond to each point, the error in their relative positions is small ($\sim 0\overset{m}{.}02$). At the same time,

the absolute value of Q and the positions of points relative to the coordinate axes are less certain and depend on the calibration accuracy (of the order of $0\overset{m}{.}1$ in B). Nevertheless, the stage of star formation in the corresponding regions can be judged by the relative positions of points. For comparison, Fig. 9 shows the solid curve obtained for model stellar systems with exponentially declining star-formation rates (see the next section for the details of model construction). The dashed curve reflects the colors of galaxies with a high percentage of young stars. It was obtained in the same model by adding stars with an age of 3×10^7 yrs and a relative mass of 10–50% of the total mass to the stellar population formed with a constant (in time) star-formation rate. The stellar metallicity was assumed to be solar.

We see from Fig. 9 that Q_{BVI} are approximately the same in the central region and in the regions on the star-formation ring, suggesting equal fractions of blue stars in them. However, the ring regions lie to the right in the diagram, apparently because the Hα emission contributes appreciably in R. The mean $W_{H\alpha}$ in the ring regions must exceed this value for the central region by about 50 Å.
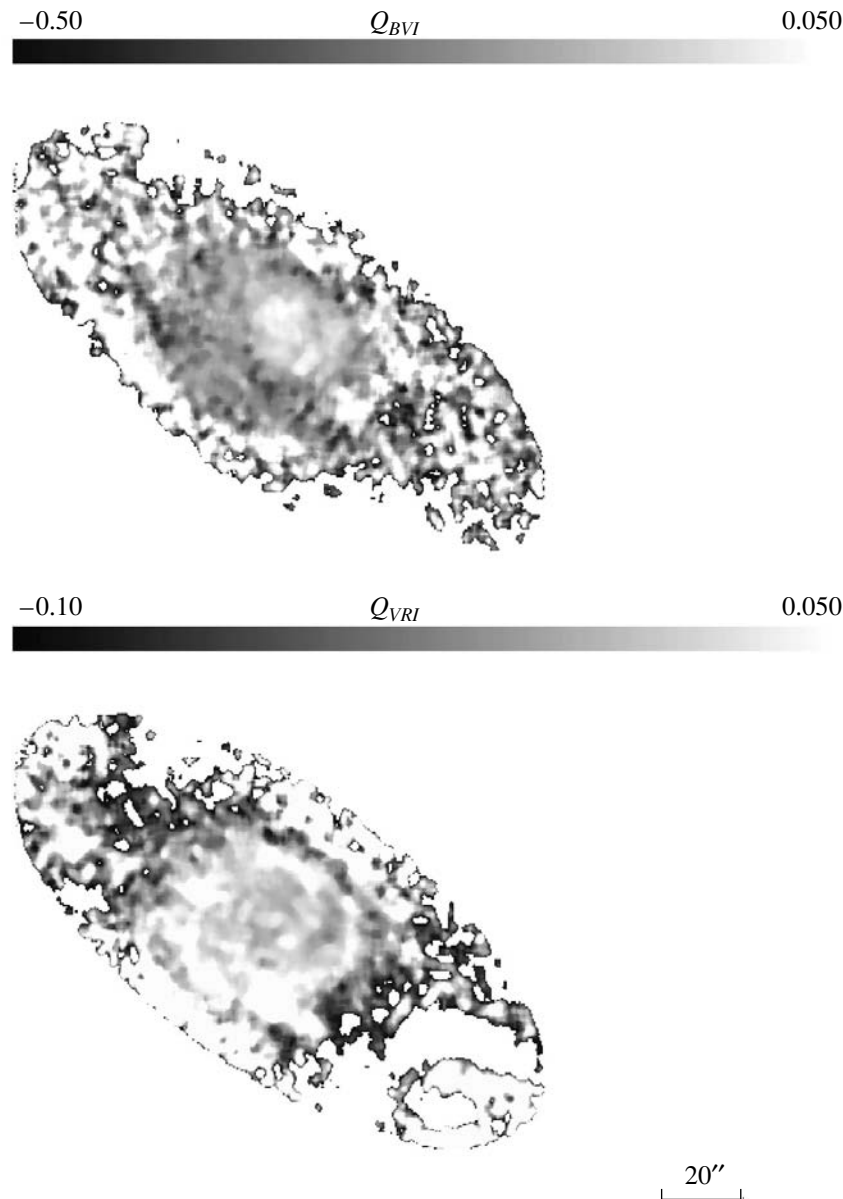
Fig. 8. Same as Fig. 7 for NGC 1134.

Note that the differences between Q_{VRI} and Q_{BVI} for the central region (represented by the diamond in Fig. 9) and the outskirts of the galaxy (the square in Fig. 9) are approximately equal to those expected for points on the model curve (solid line in Fig. 9), suggesting approximately the same contribution of Hα emission for these regions. At the same time, the difference in Q_{BVI} points to a larger contribution of young blue stars to the emission from the central region (as well as the blue ring) than that for the outskirts. Thus, the state of star formation in the corresponding regions can be judged from the relative positions of points on the Q_{VRI}–Q_{BVI} diagram. A high percentage of blue stars, together with strong Hα emission, suggest an intense ongoing formation of massive stars.

SELECTIVE ABSORPTION IN GALAXIES

Selective absorption can be roughly estimated from the positions of the galaxy or its separate regions on a two-color diagram relative to the normal color sequence (NCS). This is the sequence along which stellar systems with different fractions of young stars without internal absorption and without abrupt changes in star-formation rates with time would be located. The NCS can be constructed by using evolutionary models of stellar systems, although the results in this case unavoidably prove to be model dependent. Nevertheless, the sequence on the two-color diagram obtained from observations of real galaxies (after the color indices were corrected for inclination) lies close to the curve theoretically calculated by evolutionary model-
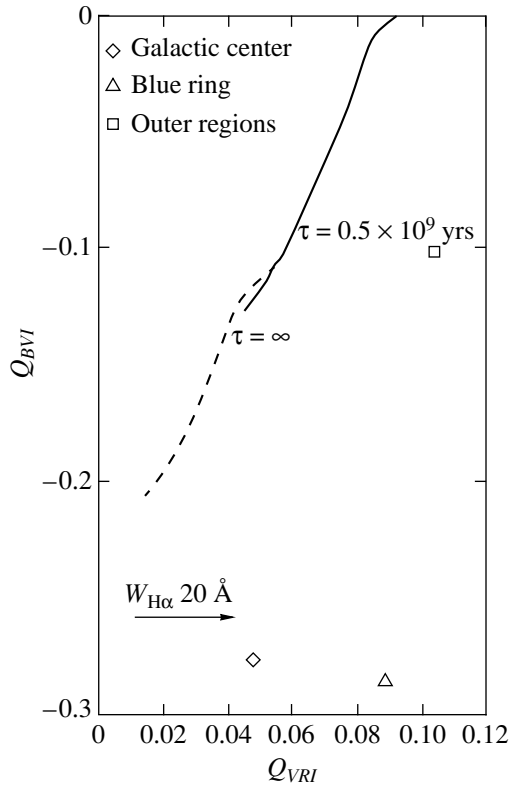
Fig. 9. Q_{VRI}–Q_{BVI} diagram for various regions of NGC 834. The average indices for the central, blue-ring, and outer galactic regions are indicated by a diamond, a triangle, and a square, respectively. The solid line represents the normal color sequence (model sequence along which the characteristic decay time scale of star formation changes). The dashed line shows how model estimates are displaced when young stars are added to the stellar population that evolves at a constant star-formation rate (a single starburst with an age of 3×10^7 yrs and with the mass fraction of young stars 10–50% of the total mass). The stellar-population metallicity was assumed to be solar. The arrow indicates the displacement of points in the presence of additional Hα emission from H II regions.

Fig. 10. $(B–V)$–$(V–I)$ diagram for various regions of NGC 834. Each point corresponds to a 5×5-pixel region with a signal-to-noise ratio >5. The dash-dotted line represents a model normal color sequence. The dashed line represents the color sequence with the inclusion of young stars. The squares indicate the mean color indices for various morphological types of galaxies (Buta and Williams 1995). Selective absorption displaces points parallel to the segment in the lower right corner of the diagram.

ing [see Searle *et al.* (1973) and a number of subsequent papers].

In order to avoid the effect of Hα emission on the color index, we restrict our analysis to the $(B–V)$–$(V–I)$ diagram. Let us consider it for NGC 834 as an example (see Fig. 10, which shows the color indices corrected for extinction in our Galaxy). The diagram for NGC 1134 is similar. The dash-dotted line represents the NCS that was computed by using a simple evolutionary model of a galaxy with an exponential decline in star-formation rate, SFR ~ exp($-t/\tau$), for various positive values of τ from 100 to 1 Gyr. Our computations were based on the model and the computational scheme proposed by Worthey (1994) for a single starburst. We also used the Geneva library of evolutionary tracks for evolutionary times 1–13 Gyr and the Padua library of evolutionary stellar tracks to model a younger stellar population with $T = 3 \times 10^7$ yrs (in the latter case, we
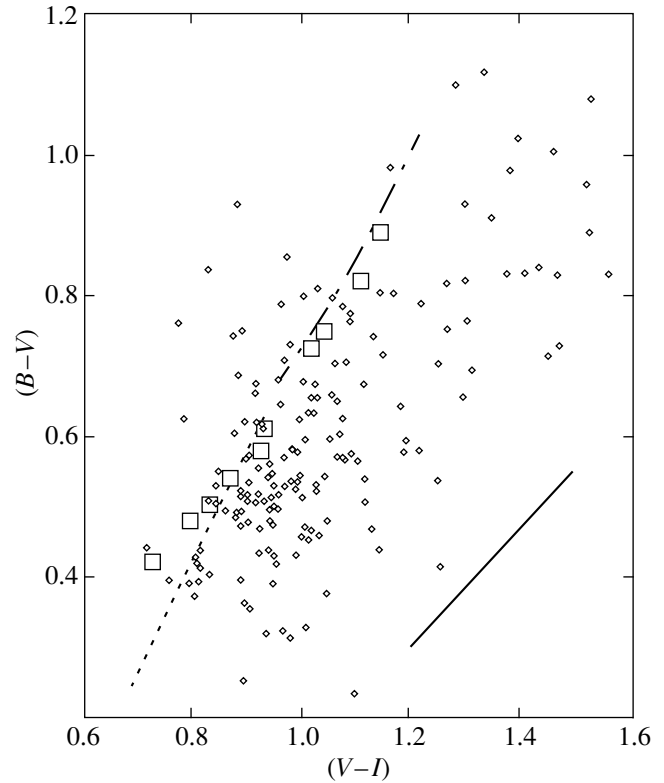
varied the mass fraction accounted for by young stars). The color sequence with the inclusion of young stars (from 5 to 40% of the total stellar-population mass) is indicated in the figure by the dotted line. The presence of a starburst in the galaxy displaces it on the diagram virtually along the NCS. For comparison with observations, the squares represent the mean color indices for various morphological types of galaxies (corrected for disk inclination to the line of sight) from Buta and Williams (1995).

If the rightward deviations from the NCS are considered as resulting from extinction, then the color excesses can be easily estimated for various galactic regions. Note that such estimates cannot claim to be accurate both because of measurement errors (since extinction displaces regions on the diagram only at a small angle to the NCS, parallel to the solid line in the lower right corner of Fig. 10) and because of certain assumptions made when modeling it. In order to reduce the errors, our estimates of the color excesses are given for 5×5-pixel regions (note that the seeing during our observations was ~1″.5). We also rejected measure-
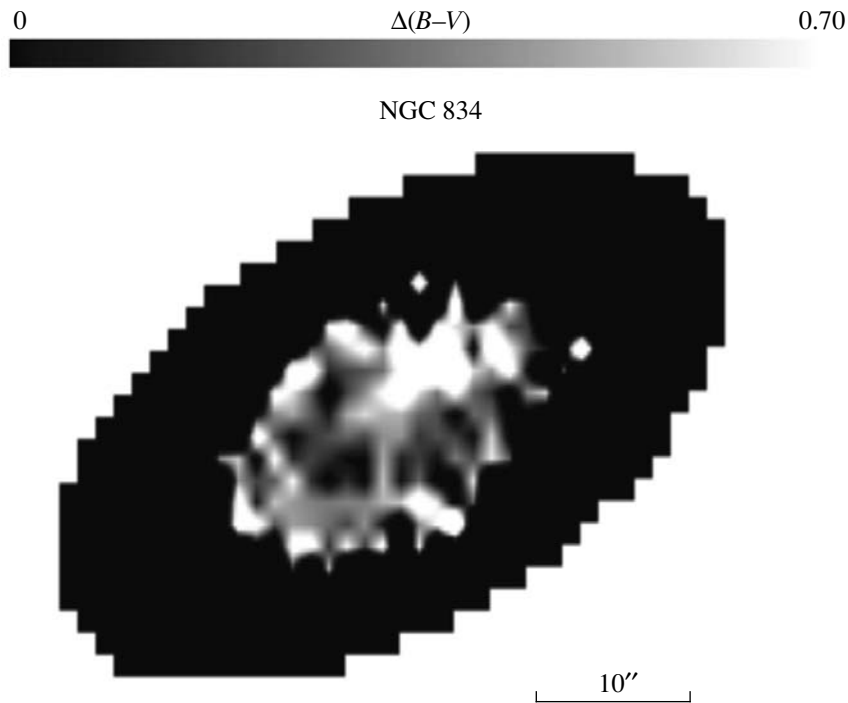
0                                    $\Delta(B–V)$ 0.70

NGC 834

10″

Fig. 11. Maps of color excesses E_{B-V} in the inner region of NGC 834.

0                                    $\Delta(B–V)$ 0.70
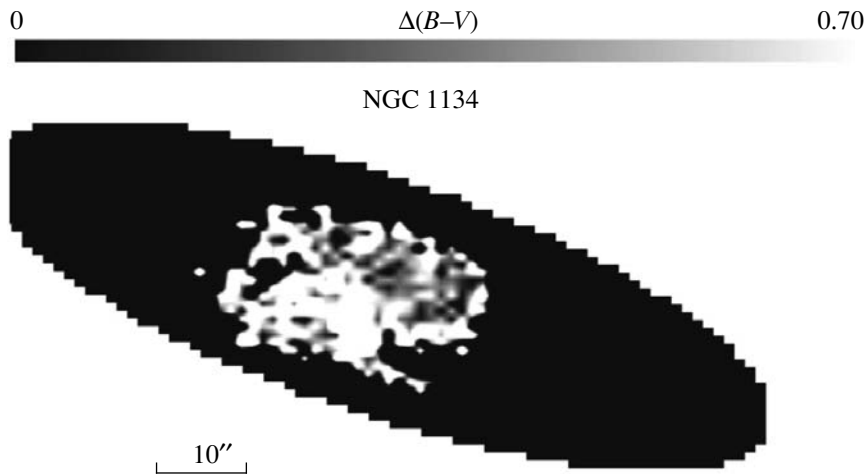
NGC 1134

10″

Fig. 12. Same as Fig. 11 for NGC 1134.

ments with a signal-to-noise ratio lower than 5. In this case, the error in E_{B-V} for the remaining points does not exceed $0\overset{m}{.}09$. The calibration-related systematic errors lie within the same limits. Zero extinction was assigned to the points leftward of the NCS on the diagram (they are few in number, and the color excesses for them do not differ from zero by more than 2σ).

The E_{B-V} maps for the inner regions of NGC 834 and NGC 1134 are shown in Figs. 11 and 12, respectively. Although the color excesses estimated by the method described above more likely correlate with the dust content in a given region than yield a reliable quantita-

tive extinction estimate, the inferred distribution of color excesses is clearly not noise in nature. The typical color excesses E_{B-V} in both galaxies are, on the average, $0\overset{m}{.}2–0\overset{m}{.}4$, which corresponds to visual extinction $A_V \approx 0\overset{m}{.}6–1\overset{m}{.}2$ if the stellar disk is viewed through a dust layer. Note that this estimate is a lower limit on the extinction, because if the stars and dust are well mixed, then a large optical depth of the disk is required to obtain the same color excess.

The largest color excesses in NGC 834 ($\sim0\overset{m}{.}7$ in $B–V$) are observed in the inner region in the western part of

the galaxy in the S and SE regions of the star-formation ring described above. Apart from a nonuniform dust distribution in the disk plane, such an extinction distribution can be explained, for example, by the inclination of the ring plane to the main galactic disk, when half of the ring lies "above" the main gas-dust layer of the galaxy and the other half lies behind it.

The situation in NGC 1134 is slightly different. Since this galaxy is highly inclined to the line of sight, the dust layer produces an asymmetry of brightness and colors along its minor axis. Indeed, the regions of minimum and maximum color excesses are located on both sides of the center near the minor axis (see Fig. 12). If the galaxy is assumed to have winding spiral arms, then, as one might expect, the largest color excesses show up in the inner region in its half located closer to us.

CONCLUSION

By reducing and analyzing our observational data, we have been able to construct the brightness and color distributions over the disks of NGC 834 and NGC 1134 and to estimate the photometric parameters of their stellar components (Table 2). The inner regions of the two galaxies are characterized by a nonuniform color distribution, both because of dust and because of local star-forming regions. An analysis of combined color indices makes it possible to minimize the distortions introduced by dust and to localize the regions of the most intense star formation. Estimates based on simple evolutionary stellar-population models show that Q_{BVI} is most sensitive to the presence of blue stars, while Q_{VRI} can be used to localize the regions of enhanced Hα emission.

As with the dusty galaxy NGC 972 (see ZM98), the star-forming regions distinguished by a decrease in Q_{BVI}, which reflects the presence of blue stars, do not all manifest themselves in the enhanced R emission associated with Hα emission. This difference in the photometric properties of star-forming regions can be attributed both to a difference in the initial mass func-

tions of stars (Hα emission originate from the most massive stars) and to the fact that the star-formation rate in the regions indistinguishable in Hα dropped about 10^7 yrs ago (the lifetime of gas-ionizing stars).

Using the galaxies considered as an example, we have shown that Q_{BVI} and Q_{VRI} help reveal the structural features that are distorted or hidden by dust (the ring of star-forming regions in NGC 834 and the inner spiral arms in NGC 1134). The color excesses and extinction can be roughly estimated from the positions of various galactic regions on a two-color diagram relative to the normal color sequence of stellar systems. Our measurements confirm the existence of substantial extinction with an asymmetric distribution of color excesses in the inner regions of both galaxies.

REFERENCES

1. R. Buta, Astron. J. **111**, 591 (1996).
2. R. Buta and D. Crocker, Astron. J. **105**, 1344 (1993).
3. R. Buta and K. Williams, Astron. J. **109**, 543 (1995).
4. J. Cardelli, G. Clayton, and J. Mathis, Astrophys. J. **345**, 245 (1989).
5. G. Clayton and P. Martin, Astrophys. J. **288**, 558 (1985).
6. D. Elmegreen, Astrophys. J., Suppl. Ser. **43**, 37 (1980).
7. L. Searle, W. L. W. Sargent, and W. G. Bagnuolo, Astrophys. J. **179**, 427 (1973).
8. V. Vansevicius, astro-ph/9906352.
9. G. Worthey, Astrophys. J., Suppl. Ser. **95**, 107 (1994).
10. A. Zasov and A. Moiseev, Pis'ma Astron. Zh. **24**, 677 (1998) [Astron. Lett. **24**, 584 (1998)].

Translated by V. Astakhov

Ultrahigh-Energy Gamma-Ray Emission
from the Geminga Pulsar

Yu. I. Neshpor, A. A. Stepanyan*, Yu. L. Zyskin, O. R. Kalekin,
V. P. Fomin, N. N. Chalenko, and V. G. Shitov

Crimean Astrophysical Observatory, National Academy of Sciences of Ukraine, p/o Nauchnyĭ, Crimea, 334413 Ukraine
Received March 22, 2000; in final form, November 16, 2000

Abstract—In 1996–1997, the Geminga pulsar was observed at the Crimean Astrophysical Observatory with a ground-based gamma-ray telescope. An analysis of the observational data suggests that this object is a source of ultrahigh-energy gamma rays. An analysis of the temporal distribution of gamma-ray photons by an epoch-folding technique reveals a periodicity in the gamma-ray emission with a period of 0.237 s. © *2001 MAIK "Nauka/Interperiodica".*

Key words: *pulsars, ground-based gamma-ray astronomy, gamma-ray photons*

INTRODUCTION

As a source of ultrahigh-energy gamma-ray emission, the Geminga pulsar was first discovered more than twenty years ago by the SAS-2 satellite (Kniffen *et al.* 1975) and, two years later, by the COS-B satellite (Masnou *et al.* 1977). Using the instrumentation onboard the *Einstein* X-ray satellite, Bignami *et al.* (1983) managed to identify Geminga with a weak X-ray source. As a result, Geminga was also detected at an optical wavelengths (Bignami *et al.* 1987). It is one of the most puzzling objects in modern astrophysics. It is of interest primarily because its gamma-ray flux (at energies > 50 MeV) is a thousand and two hundred thousand times higher than that in the X-ray and optical bands, respectively. Thompson *et al.* (1977) detected a periodicity with a period of 59 s in the SAS-2 observational data for 1972–1973 at energy 35 MeV. Subsequently, from 1972 until 1983, the Geminga flux was found to be also variable with the same period in other energy bands (Bignami *et al.* 1984) up to ultrahigh energies (Zyskin and Mukanov 1983). However, Buccheri *et al.* (1985) questioned the validity of the estimates for the significance of the above results.

Geminga observations continued and produced results. Based on ROSAT data, Halpern and Holt (1992) found pulsations with a period of 0.237 s in the X-ray emission from Geminga. The reduction of EGRET (Bertsch *et al.* 1992), COS-B (Bignami and Caraveo 1992; Hermsen *et al.* 1992), and SAS-2 (Mattox *et al.* 1992) observational data confirmed the presence of a periodicity with a period of 0.237 s. The ground-based observations of Geminga in 1983 (Bowden *et al.*

1993) and in 1984–1985 (Vishwanath *et al.* 1993) through the detection of Cherenkov flashes in the atmosphere also revealed a pulsating component with a period of 0.237 s in the ultrahigh-energy gamma-ray emission. According to *Gamma-1* observations, the total pulsating flux is $(1.1 \pm 0.3) \times 10^{-6}$ cm^{-2} s^{-1} at energies 300–5000 MeV (Akimov *et al.* 1993). It should be noted, however, that the Whipple Observatory group detected no ultrahigh-energy gamma rays from Geminga during their 1989–1991 observations (Akerlof *et al.* 1993). Radio observations of Geminga at the radio-astronomical station of the Astrospace Center (Lebedev Physical Institute, Russian Academy of Sciences) in 1992, 1993, and 1996 revealed radio pulses with a period of 0.237 s (Shitov and Pugachev 1997). Mattox *et al.* (1998) analyzed the long-term (24.2 years) SAS-2, COS-B, and EGRET data on gamma-ray emission. The ephemeris of the Geminga pulsar was computed with a high accuracy. In 1996 and 1997, the Geminga gamma-ray source was observed at the Crimean Astrophysical Observatory with the GT-48 gamma-ray telescope at ultrahigh energies. Below, we analyze the observational data.

DESCRIPTION
OF THE GT-48 GAMMA-RAY TELESCOPE

The GT-48 gamma-ray telescope records photons with energies $> 10^{12}$ eV by detecting Cherenkov flashes produced by the interaction of ultrahigh-energy gamma-ray photons with the nuclei of atoms in the Earth's atmosphere. The area illuminated by a Cherenkov flash is rather large, tens of thousands of square meters, which makes it possible to record low ($\sim 10^{-11}$ cm^{-2} s^{-1}) gamma-ray fluxes. The main obstacle to detecting and analyzing ultrahigh-energy gamma-ray sources is a substan-

---

* E-mail address for contacts: arnold@crao.crimea.ua

tial background of cosmic rays. The latter produce Cherenkov flashes in the Earth's atmosphere that are difficult to distinguish from those generated by gamma-ray photons.

New detectors, multi-element cameras, are used to cut off most of the Cherenkov flashes produced by charged cosmic-ray particles. Multi-element cameras form discretized images of Cherenkov flashes. The first telescope of this type came into operation in 1982 at the Whipple Observatory (USA) (Cawley *et al.* 1983).

Our observations with the GT-48 gamma-ray telescope at the Crimean Astrophysical Observatory were started in 1989. The facility consists of two identical altazimuth mountings (sections), northern and southern, separated by a distance of 20 m in the north–south direction and located at an altitude of 600 m above sea level. We have repeatedly described GT-48 in various papers (Vladimirskiĭ *et al.* 1994; Neshpor *et al.* 1998). The GT-48 gamma-ray telescope differs from other operating telescopes in that it also records Cherenkov flashes in the ultraviolet (200–300 nm). The total area of the GT-48 mirrors is 54 m². The control system moves the facility with a tracking accuracy of ±1′. Observations can be carried out both in the mode of coincidence between the two sections and independently with each section. The flash detection time is recorded to within one microsecond. A crystal oscillator is used as the clock. The relative accuracy of the clock rate was 5×10^{-9} over the observing period.

DATA REDUCTION

We observed the Geminga object ($\alpha = 6^h33^m37^s$ and $\delta = 17°46′25″$ for the epoch 1996) with two aligned sections in coincidence mode with a time resolution of 100 ns. The advantages of this detection technique were detailed by Chalenko *et al.* (1997). We tracked the object by comparing observations of the gamma-ray source with cosmic-ray background observations shifted in time from each other by 40 min. The off-source observations preceded the on-source observations, and they were performed at the same azimuth and zenith angles. Five and eight 35-min-long observing sessions were conducted in 1996 and 1997, respectively; the total duration of the source's observations was 175 and 280 min in 1996 and 1997, respectively.

The data were subjected to preliminary reduction, which is required to correctly calculate the first and second moments of the light distribution. The latter were used to determine the following Cherenkov-flash parameters: effective length *A*, effective width *B*, orientation angle φ characterizing the direction of maximum elongation of the flash image, and centroid coordinates of the light distribution X_c and Y_c. All the other possible Cherenkov-flash parameters can be inferred from these quantities (Vladimirskiĭ *et al.* 1994). After the preliminary data reduction, 3867 on-source and 3826 off-source events and 5725 on-source and 5690 off-source

events observed in 1996 and 1997 were left for the subsequent analysis.

For the possible flux of gamma-ray photons to be determined, they must be selected by excluding flashes produced by charged cosmic-ray particles.

As we have already noted above, the parameters of the Cherenkov flashes from ultrahigh-energy gamma-ray photons differ little from the parameters of the flashes generated by charged cosmic-ray particles (*p*-showers). Nevertheless, most of the flashes generated by *p*-showers can be excluded, thereby significantly increasing the ratio of the number of selected gamma-ray photons to the number of background ones. In this case, we must correctly choose the boundary values for the selection parameters to obtain an optimal signal-to-noise ratio $Q = (N0_s - N0_b)/\sqrt{N0_s + N0_b}$, where $N0_s$ and $N0_b$ are the numbers of selected gamma-ray-like flashes in the on- and off-source observations, respectively. The difference $N0_s - N0_b = N_\gamma$ is the number of selected gamma-ray photons detected over the observing period, and $\sqrt{N0_s + N0_b}$ is the statistical error in the number of gamma-ray photons after selection. If the selection is made by using several parameters, then up to 99% or more flashes from the charged component can be excluded.

Since the parameters of each flash (event) recorded simultaneously with each section were determined independently, they had two values denoted for the northern and southern sections by numbers 1 and 2, respectively. We used several selection criteria with Cherenkov-flash parameters to reduce the background of the flashes generated by charged cosmic-rays particles.

When selecting events, we primarily considered the flash amplitude *V*, which is proportional to the total "energy" of the recorded radiation (integrated flux from the flash). The amplitude was determined for the same area as the second moment of the flashes. Showers with amplitudes $V(1) < 100$ discretization units (500 photons) of the analog-to-digital converter or $V(2) < 100$ were excluded from the subsequent analysis, because the parameters of these flashes were determined with a large error.

The effective length *A* and effective width *B* of the flash image were used as the selection parameters. Events were excluded from the subsequent analysis, if at least one of the following conditions was satisfied: $A(1) > 0°30; A(2) > 0°32; B(1) > 0°17;$ and $B(2) > 0°17$.

As has already been noted above, we recorded the ultraviolet emission from flashes. The electrons from *p*-showers of a given energy are known to penetrate appreciably deeper into the Earth's atmosphere than those from gamma-ray showers of the same energy. As a result, the Cherenkov flashes from *p*-showers have considerably higher fluxes in the wavelength range 200–300 nm (ultraviolet) than those from gamma-ray showers (Stepanyan *et al.* 1983). Below, the ratio of the

Table 1. The number of detected and selected events

Selection method	Number of on-source events	Number of off-source events	Difference	Difference-to-error ratio	Year
Without selection	3867	3826	41	0.43	1996
Selection by coordinate-independent parameters	176	103	73	4.37	
Without selection	5725	5690	35	0.33	1997
Selection by coordinate-independent parameters	109	86	23	1.65	

flash amplitude in this spectral range (*U*) to the total amplitude in the visible range (*V*) is called the *UV* parameter for simplicity. This parameter was first successfully used by us when analyzing observations of the Crab nebula (Kalekin *et al.* 1995) and, subsequently, of other objects.

Selection with the *UV* parameter averaged over all the years of observations increased the confidence level of the results to 4.4 standard deviations. The *A*, *B*, *V*, and *UV* parameters do not depend on the flash position relative to the source and are called coordinate-independent parameters.

The data obtained by selection using the above parameters are given in Table 1.

Thus, the observational data for Geminga on the coordinate-independent parameters of flashes can be considered to point to the presence of an ultrahigh-energy gamma-ray flux from this object. An analysis of the periodic pattern of ultrahigh-energy gamma-ray radiation further confirms this result.
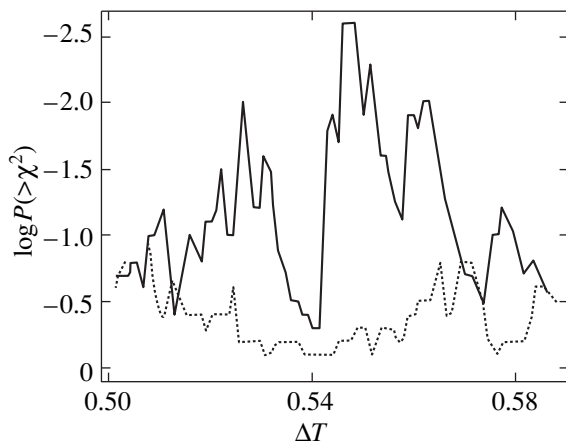

Fig. 1. A fragment of the periodogram as constructed from the 1996 data. The logarithm of the statistical probability of a random deviation ($>\chi^2$) is plotted along the vertical axis; $\Delta T = (T - 0.237099300) \times 10^7$, where *T* is the period in seconds, is plotted along the horizontal axis. The solid and dotted lines refer to on- and off-source observations, respectively.

PULSATING GAMMA-RAY RADIATION

The above observations were analyzed in an effort to detect a pulsating component with a period of 0.237 s in the ultrahigh-energy gamma-ray radiation. We do not pose the problem of searching for a period but only want to test the hypothesis that there is a periodicity in our observations based on the highly accurate ephemeris inferred from published long-term data (Shitov and Pugachev 1997; Mattox *et al.* 1998). Using SAS-2, COS-B, and EGRET data, Mattox *et al.* (1998) obtained the following ephemeris for the epoch $t = $ JD 2 446 600 (June 18, 1986): $f = 4.217705363081(13)$ Hz, $\dot{f} = -1.9521712(12) \times 10^{-13}$ Hz s^{-1}, and $\ddot{f} = 1.49(3) \times 10^{-25}$ Hz s^{-2}. Shitov and Pugachev (1997) derived the following period from the radio observations of Geminga from 1992 until 1996: $T = 0.23709745295(12)$ s and $\dot{T} = 10.9765(15) \times 10^{-15}$ s s^{-1} for the epoch JD = 2 448 400. Although the error in the period inferred from radio data is larger, the epoch of these observations is closer to that of our observations (JD 2 450 401, November 13, 1996).

We used the above results to compute the period and its derivative for the epoch of our observations. For November 13, 1996, $T = 0.2370993496$ s and $\dot{T} = -1.09715948 \times 10^{-14}$ s s^{-1} (Mattox *et al.* 1998) and $T = 0.2370993506$ s and $\dot{T} = -1.09765 \times 10^{-14}$ s s^{-1} (Shitov and Pugachev 1997) (the second derivative was not determined). For November 1, 1997, $T = 0.2370996833$ s and $\dot{T} = -1.09713706 \times 10^{-14}$ s s^{-1} (Mattox *et al.* 1998) and $T = 0.2370996845$ s and its derivative is the same (Shitov and Pugachev 1997). We analyzed the observational data for periodicity in a narrow frequency range within ±5 steps of independence of the computed periods. For our data, the independence step is 5×10^{-9} s and 4×10^{-9} s for 1996 and 1997, respectively, which is much larger than the difference between the frequencies predicted by Shitov and Pugachev (1997) and Mattox *et al.* (1998) (10^{-9} s). The analysis was performed by the epoch-folding technique for the events selected by coordinate-independent parameters from on-source observations (176 and 109 events for 1996 and 1997, respectively). For checking purposes, we also analyzed
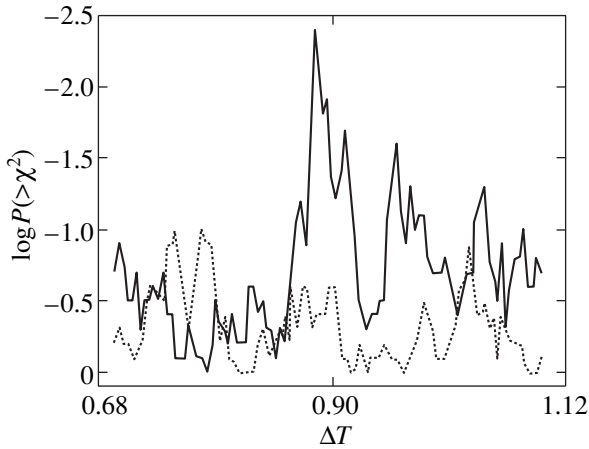
Fig. 2. A fragment of the periodogram as constructed from the 1997 data (the notation is the same as in Fig. 1). $\Delta T = (T - 0.237099600) \times 10^7$.
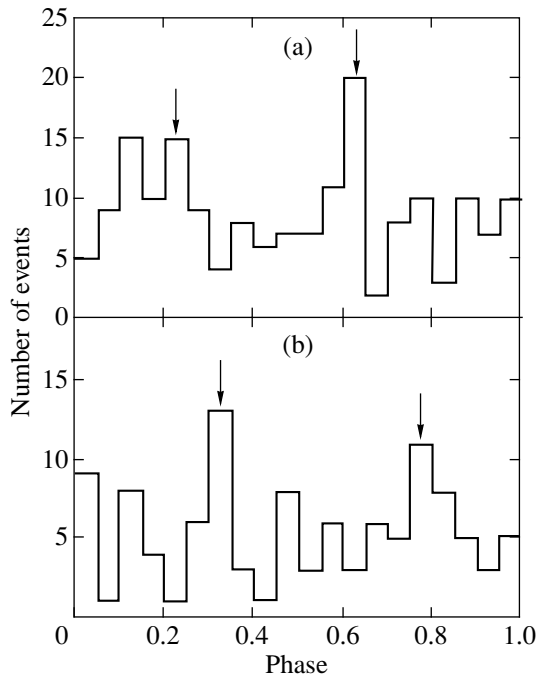

Fig. 3. Phase histograms for (a) $T = 0.237099354$ s (1996) and (b) $T = 0.237099688$ s (1997).

the events selected by coordinate-independent parameters from off-source observations (103 and 86 events for 1996 and 1997, respectively). For each event, we determined its phase from the specified period and its

Table 2. Gamma-ray flux measurements for Geminga

Observatory	Epoch of observations	Energy range, TeV	Flux, 10^{12} cm^{-2} s^{-1}
HEGRA	1996	>1	<2.3
Whipple	1989–1991	>0.5	<8.8
Durham team	1983	>1	30
Ootakamund	1984–1985	>0.8	21 ± 8
Crimean Astrophysical Observatory	1996, 1997	>1	24 ± 8

derivative. The period was taken at the start of our observations. Variations in the period derivative during our observations (less than one month) were disregarded because they were small. We broke down the entire period into twenty phase bins and constructed the phase histogram (light curve) of events. The light curves were constructed for each trial period and analyzed by the χ^2 test. For each χ^2, we determined the $(>\chi^2)$ probability of a random distribution for the phase histogram.

We then analyzed the periodograms obtained in this way. Figures 1 and 2 show their fragments based on the 1996 and 1997 data, respectively. In Figs. 1 and 2, the trial period and the logarithm of probability $P(>\chi^2)$ are plotted along the horizontal and vertical axes. The solid and dotted lines refer to the on- and off-source observations, respectively.

The logarithm of probability in the periodograms obtained from off-source observations does not exceed unity (in absolute value). This fact and the pattern of the periodograms constructed from on-source observations suggest that there is a periodicity in the ultrahigh-energy gamma-ray radiation with period $T = 0.237099354(5)$ for 1996 and $T = 0.237099688(4)$ s for 1997. The independence step is given in parentheses. We consider this value to be the error with which the period can be determined. In addition, recall that the relative error in the detection time over the period of GT-48 observations was 5×10^{-9}.

The probabilities of a random phase distribution of events are $P = 2.3 \times 10^{-3}$ for 1996 and $P = 3.4 \times 10^{-3}$ for 1997. Given the derivative, the period inferred by Malofeev and Malov (1997) for an epoch (MJD = 50 434.4) close to that of our observations yields $P = 0.237099351$ s, which closely matches our period for MJD = 50 401. It is of interest to examine the phase histograms (light curves) for these two periods (see Fig. 3). Note the presence of two peaks in the light curves (marked by arrows) separated by $\Delta\varphi = 0.40$–0.45. The 1996 and 1997 light curves cannot be phased because of the uncertainty (error) in the period. The light curve reported from Mattox *et al.* (1998) also exhibits two peaks separated by $\Delta\varphi = 0.48$.

CONCLUSION

Having analyzed our observations of the Geminga pulsar, we obtained the following results:

(1) An ultrahigh-energy gamma-ray flux is observed from the pulsar at a confidence level of 4.4 standard deviations.

(2) A periodicity analysis by the epoch-folding technique in a narrow interval near the period inferred in other energy bands [radio and high-energy (~100 MeV) gamma-ray photons] revealed a periodicity in the gamma-ray flux. The probability of a random phase distribution of the flux is 0.3%.

These two results collectively suggest that Geminga is an ultrahigh-energy gamma-ray source.

As we already pointed out in the Introduction, the results of Geminga observations by different groups of researchers differ markedly. The measured fluxes and the epochs of observations are given in Table 2.

The negative results obtained at the Whipple and HERGA observatories (Aharonian *et al.* 1999) may be attributable to variability of the source. As we noted in the Introduction, positive results were obtained in the observations of the Durham (Bowden *et al.* 1993) and Indian (Vishwanath *et al.* 1993) teams of researchers.

REFERENCES

1. F. A. Aharonian, A. G. Ahperjanian, J. A. Barrio, *et al.*, Astron. Astrophys. **346**, 913 (1999).
2. C. W. Akerlof, A. C. Breslin, M. F. Cawley, *et al.*, Astron. Astrophys. **274**, L17 (1993).
3. V. V. Akimov, V. G. Afanas'ev, I. D. Blokhintsev, *et al.*, Pis'ma Astron. Zh. **19**, 579 (1993) [Astron. Lett. **19**, 229 (1993)].
4. D. L. Bertsch, K. T. S. Brazier, C. E. Fichtel, *et al.*, Nature **357**, 306 (1992).
5. G. F. Bignami and P. A. Caraveo, Nature **357**, 287 (1992).
6. G. F. Bignami, P. A. Caraveo, and R. C. Lamb, Astrophys. J. Lett. **272**, L9 (1983).
7. G. F. Bignami, P. A. Caraveo, and J. A. Paul, Nature **310**, 464 (1984).
8. G. F. Bignami, P. A. Caraveo, J. A. Paul, *et al.*, Astrophys. J. **319**, 358 (1987).
9. C. C. G. Bowden, S. M. Bradbury, P. M. Chadwick, *et al.*, J. Phys. G **19**, L29 (1993).
10. R. Buccheri, N. D'Amico, W. Hermsen, and B. Sacco, Nature **316**, 131 (1985).
11. M. F. Cawley, J. Clear, D. J. Fegan, *et al.*, in *Proceedings of the 18th International Cosmic Ray Conference, Bangalore, 1983*, Vol. 1, p. 118.
12. N. N. Chalenko, O. R. Kalekin, Yu. I. Neshpor, *et al.*, Astrophys. Astron. **18**, 151 (1997).
13. J. P. Halpern and S. S. Holt, Nature **357**, 222 (1992).
14. W. Hermsen, B. N. Swanenburg, R. Buccheri, *et al.*, IAU Circ., No. 5541 (1992).
15. O. R. Kalekin, Yu. I. Neshpor, A. A. Stepanyan, *et al.*, Pis'ma Astron. Zh. **21**, 184 (1995) [Astron. Lett. **21**, 163 (1995)].
16. D. A. Kniffen, G. F. Bignami, C. E. Fichtel, *et al.*, in *Proceedings of the 14th International Cosmic Ray Conference, Munchen, 1975*, Vol. 1, p. 100.
17. V. M. Malofeev and O. I. Malov, Nature **389**, 697 (1997).
18. J. L. Masnou, K. Bennet, G. F. Bignami, *et al.*, in *Proceedings of the 12th ESLAB Symposium, Frascati, 1977*, p. 33.
19. J. R. Mattox, D. L. Bertsch, C. E. Fichtel, *et al.*, Astrophys. J. Lett. **401**, L23 (1992).
20. J. R. Mattox, J. P. Helpern, and P. A. Caraveo, Astrophys. J. **493**, 891 (1998).
21. Yu. I. Neshpor, A. A. Stepanyan, O. R. Kalekin, *et al.*, Pis'ma Astron. Zh. **24**, 167 (1998) [Astron. Lett. **24**, 134 (1998)].
22. Yu. P. Shitov and V. D. Pugachev, New Astron. **3**, 101 (1997).
23. A. A. Stepanyan, V. P. Fomin, and B. M. Vladimirskiĭ, Izv. Krym. Astrofiz. Obs. **66**, 234 (1983).
24. D. J. Thompson, C. E. Fichtel, and R. C. Hartman, Astrophys. J. **213**, 252 (1977).
25. P. R. Vishwanath, G. P. Satyanarayana, P. V. Ramanamurty, *et al.*, Astron. Astrophys. **267**, L5 (1993).
26. B. M. Vladimirskiĭ, Yu. L. Zyskin, A. P. Kornienko, *et al.*, Izv. Krym. Astrofiz. Obs. **91**, 74 (1995).
27. Yu. L. Zyskin and D. B. Mukanov, Pis'ma Astron. Zh. **9**, 219 (1983) [Sov. Astron. Lett. **9**, 117 (1983)].

Translated by A. Dambis

H I Distribution in the Region
of the Supernova Remnant G78.2 + 2.1

I. V. Gosachinskij*

*Special Astrophysical Observatory, St. Petersburg Branch, Russian Academy of Sciences,
Pulkovo, St. Petersburg, 196140 Russia*

Abstract—Based on RATAN-600 21-cm line observations with an angular resolution of 2.4′ over a wide range of radial velocities, we analyze the neutral-hydrogen distribution in the region of the SNR G78.2 + 2.1. In addition to an H I shell at low radial velocities immediately surrounding the radio remnant, we detected an extended expanding H I shell, $\approx 3°$ in diameter, at a radial velocity of –25 km s^{-1}, which closely coincides in coordinates and angular sizes with the outer X-ray shell discovered by Lozinskaya *et al.* (2000). The Hα emission studied by these authors in the SNR region also has a secondary peak at radial velocities from –45 to –20 km s^{-1}. Since the radial velocities of these two objects differ significantly, their distances can be assumed to differ as well; i.e., a chance projection of two distinct objects is observed. © *2001 MAIK "Nauka/Interperiodica"*.

Key words: *supernovae, supernova remnants, interaction with medium*

INTRODUCTION

The well-known shell-type supernova remnant (SNR) G78.2 + 2.1 [see Green (1996), Gosachinskij *et al.* (1999), and Lozinskaya *et al.* (2000) for references] is projected onto the region of the Cygnus X radio source. More than fifty various objects, mostly compact H II regions (Piepenbrink and Wendker 1988), are located there in a small area of the sky (a mere 6°–7° in diameter). Only three of these objects, judging from their H 110 α radial velocities measured by the above authors, are projected by chance onto this region from more distant spiral arms. At the same time, the interpretation of observations in this region is complicated by uncertainties in distances, especially kinematic ones, because of the small dv/dr, and by the fact that the line of sight passes along the Orion-Cygnus spiral arm.

The interstellar medium in this region has been studied by dozens of authors over various wavelength ranges and in various spectral lines. Gosachinskij *et al.* (1999) discovered two ring-like H I structures, which morphologically resemble expanding shells. One of them, with a larger angular size, is located around the Cygnus X radio source, and the other, at a mean radial velocity of +3 km s^{-1}, immediately surrounds SNR G78.2 + 2.1. A quantitative analysis shows that it could be produced both by the SNR shock wave and by the progenitor star's stellar wind. Here, we also give references to previous studies of neutral hydrogen in

the SNR region and critically analyze the results of some of them.

The archival ROSAT and ASCA X-ray data were analyzed by Lozinskaya *et al.* (2000). Their analysis revealed two clumpy nested X-ray shells, which may be associated with this SNR. The surprising thing is that, whereas one of them, composed of three clouds, is only slightly larger than the SNR, the angular diameter of the second, weaker shell is three times that of the SNR. Bearing in mind that this region is very rich in various objects, a chance projection of X-ray features onto one another and onto the SNR cannot be ruled out. On the other hand, high-angular-resolution observations are known to commonly reveal shells or cavities in the H I distribution where active objects with high energy release are located: SNRs, H II regions, or stellar-wind-associated shells, let alone X-ray emitting regions. For this reason, when investigating the relationship of the H I distribution to SNR G78.2 + 2.1 and other objects, it makes sense not to restrict the analysis to radial velocities near zero, which corresponds to the SNR distance, but to consider the entire H I-line range. Below, we present our results.

INSTRUMENTATION AND REDUCTION

We used 18 drift curves in right ascension at 0.6° intervals in declination obtained with the RATAN-600 radio telescope to investigate the interstellar-gas distribution in the region of the Cygnus X radio source and SNR G78.2 + 2.1. The instrumentation and reduction are detailed in Gosachinskij *et al.* (1999), but, for con-

---

* E-mail address for contacts: gos@fsao.spb.su

venience, we give their brief description. In this elevation range, the RATAN-600 antenna at 21 cm has an angular resolution of $2' \times 12'$, an effective area of 875 m^2, and substantial (up to 40%) losses in brightness temperature. The latter is attributable to the specific antenna design and to the fact that the observations were carried out near zenith. The system noise temperature is 60 K; the 39-channel filter spectrum analyzer has a channel bandwidth of 30 kHz (6.3 km s^{-1}). The drift curve at each declination consists of two series of three observations, each obtained by shifting the receiver tuning frequency by half the channel bandwidth. As a result, each drift curve has 78 channels that follow at intervals of 3.15 km s^{-1}. This observing technique also allows for an effective interference cleaning. The mean square of fluctuations in spectral channels on an averaged scan is 0.2 K. The antenna and equipment parameters were checked in each series of observations by measuring a set of reference sources (Venger *et al.* 1979).

Subsequently, we subtracted an extended background obtained by spline interpolation at lower brightness-distribution level from the drift curves in each spectral channel and then reduced the drift curves containing only features of small angular sizes. The subtracted background of the drift curves includes: (1) large-scale features of the interstellar-gas distribution, such as spiral arms or giant complexes; (2) emission from the intercloud medium, if present; (3) features of small angular sizes unresolved by the RATAN-600 beam; and (4) spurious large-scale background produced by distant side lobes and the RATAN-600 stray field. It should be noted that subtracting the background by the above method could result in an underestimation of the brightness and angular sizes of the remaining small-scale features, whose parameters were determined by using a code of Gauss analysis.

The measured parameters have the following errors. The radial velocity of an isolated medium-brightness H I feature is measured with an accuracy of ± 1 km s^{-1}. In several cases noted below, the accuracy is reduced because of the difficulties in separating the object from the background or from neighboring features. Given the antenna calibration errors, the measurement error of the H I-line brightness temperature is about 0.5 K, while the error of the estimated angular sizes in right ascension is 0.1°. The same qualifications as those for the radial velocities hold in the latter case. The antenna resolution in declination is much lower, and, accordingly, the accuracy of measuring angular sizes is lower. The accuracy of estimating distances depends on the method of their determination, and it should be considered separately in each case. As a result, the accuracy of estimating the H I mass turns out to be no higher than 0.5–1 order of magnitude.

OBSERVATIONS AND THEIR DISCUSSION

The brightness distribution of H I features at a radial velocity of +10 km s^{-1} after the extended radio-line emission background in the region of the Cygnus X radio source and SNR G78.2 + 2.1 has been subtracted is shown in Fig. 1. The declinations of the drift curves are indicated on the right; the vertical and horizontal scales slightly differ. The ring-like H I structures that can be correlated with the above objects, as was done by Gosachinskij *et al.* (1999), are represented by thin lines.

A schematic 21-cm radio image of the SNR from Higgs *et al.* (1977) is shown in Fig. 2 (heavy circle) together with X-ray (0.5–2.0 keV) isophotes from Lozinskaya *et al.* (2000). In this figure, the vertical and horizontal scales are approximately the same.

Gosachinskij *et al.* (1999) found that the smaller ring-like H I structure immediately surrounds the radio remnant and determined the following observed parameters of the H I shell around the SNR:

Coordinates of the center α (2000.0) = $20^h21.3^m$, δ (2000.0) = +40.8°;

Angular sizes $2.8° \times 3.5°$ (inner) and $2.0° \times 2.5°$ (outer);

Mean brightness temperature of the line 8 ± 0.5 K;

Mean radial velocity +3 km s^{-1};

The radial-velocity range in which the H I shell was observed ≥ 20 km s^{-1}.

When identifying the H I shell, we carefully allowed for the effect of the H I absorption line, because the SNR continuum emission was intense. We also compared the detected structure with the data of other authors who analyzed the H I distribution in this region.

We assumed the SNR distance to be 1.5 kpc (Landecker *et al.* 1980) when calculating the following physical parameters of the H I shell around G78.2 + 2.1:

Large-scale velocity of radial motions ≥ 10 km s^{-1};

Outer diameter 75 pc;

Inner diameter 55 pc;

Gas density 2.5 cm^{-3};

Shell mass $8.1 \times 10^3 M_\odot$.

If the H I shell around SNR G78.2 + 2.1 results from the impact of the shock wave generated by a supernova explosion on the interstellar gas, then the initial explosion energy and the SNR age can be estimated from observed H I-shell parameters. The required density of the ambient interstellar medium, $n_0 \simeq 1.6$ cm^{-3}, was estimated by Gosachinskij *et al.* (1999) by assuming that the H I-shell gas was initially "spread" over its entire volume.

The presence of an expanding H I shell around the SNR was also assumed to suggest that the remnant is in the radiative phase. In this case, using relations from Wheeler *et al.* (1980), we obtained the initial explosion energy and the SNR age:

$$E_0 = 3 \times 10^{50} \text{ erg and } t = 1.1 \times 10^6 \text{ yr.}$$

Although the derived initial explosion energy is in good agreement with the universally accepted value,
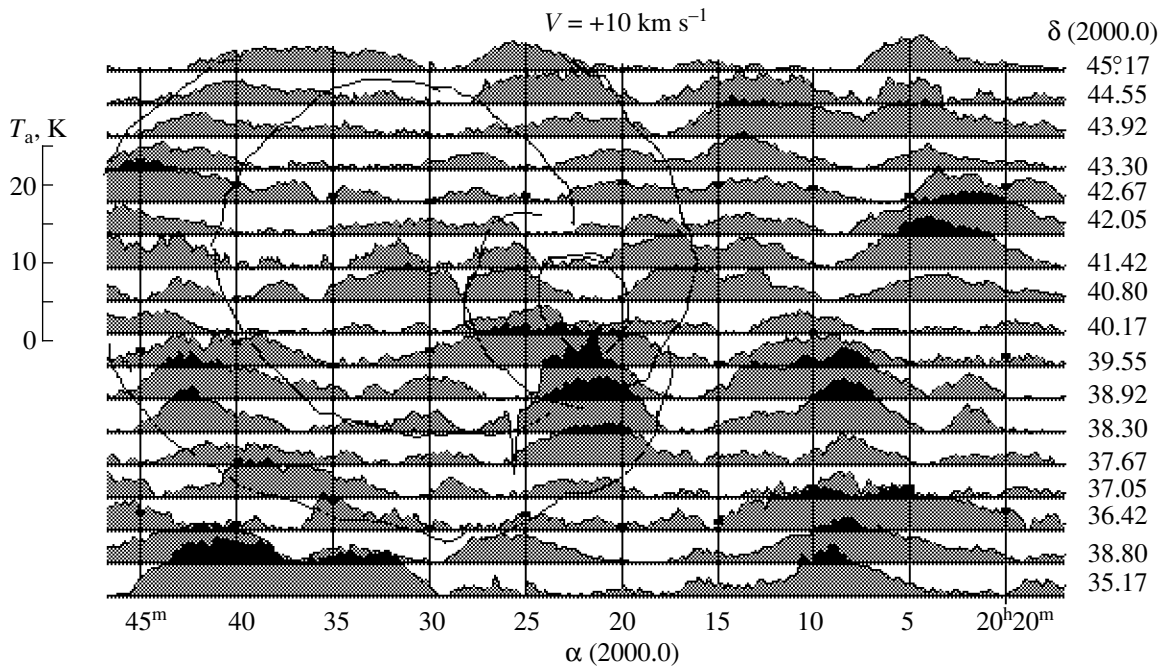
$V = +10$ km s^{-1}

Fig. 1. The brightness distribution of H I features at a radial velocity of +10 km s^{-1} after an extended background in the region of the Cygnus X radio source and SNR G78.2 + 2.1 has been subtracted. The declinations of H I drift curves are indicated on the right; the vertical and horizontal scales are different. The thin lines represent the ring-like H I structures related to the above objects (Gosachinskij *et al.* 1999).

the age proves to be too large for an X-ray emitting remnant. As an alternative explanation, Gosachinskij *et al.* (1999) assumed that an extended slow H I shell could be produced by the supernova progenitor's stellar wind. Using the calculations by Weaver *et al.* (1977), we then estimated the stellar-wind intensity and duration required for the formation of an H I shell from its observed parameters to be

$$L_w = 10^{36} \text{ erg and } t = 2.3 \times 10^6 \text{ yr.}$$

Such an intensity is characteristic of the winds from OB stars with $M_{init} \geq 8M_\odot$, which produce supernova explosions, while the wind duration is an order of magnitude shorter than the main-sequence lifetimes of these stars. This confirms that the outer H I shell around SNR G78.2 + 2.1 could be produced by the supernova progenitor's stellar wind.

Data on the soft X-ray emission from the G78.2 + 2.1 region (Lozinskaya *et al.* 2000) (see Fig. 2) confuse the picture further still. The presence of the so-called inner X-ray shell, which consists of three extended clouds and coincides almost exactly with the radio remnant in coordinates and angular sizes, can still be explained somehow if the remnant is still in the adiabatic phase [see Lozinskaya *et al.* (2000) for a detailed discussion]. The weak outer clumpy X-ray shell (of course, if it actually exists) is offset by almost 1° northwest of the radio-remnant center. In addition, its angular size is almost triple that of the remnant, which also completely disagree with the sizes and location of the H I shell

detected by Gosachinskij *et al.* (1999). Note, however, that, in accordance with the assumed distance to the remnant, the latter authors analyzed the association of the H I shell with the SNR only at nearly zero radial velocities. Clearly, the pattern of H I distribution should be studied over a much wider range of radial velocities.
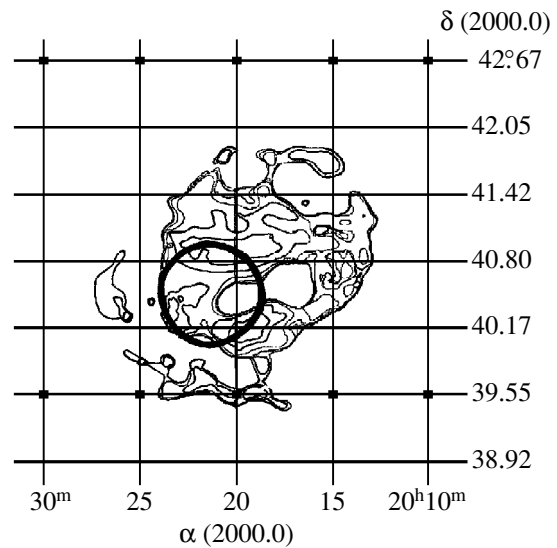

Fig. 2. A schematic image of SNR G78.2 + 2.1 as constructed from the 21-cm data of Higgs *et al.* (1977) (heavy circle) and X-ray (0.5–2.0 keV) isophotes from Lozinskaya *et al.* (2000). The vertical and horizontal scales and approximately the same.
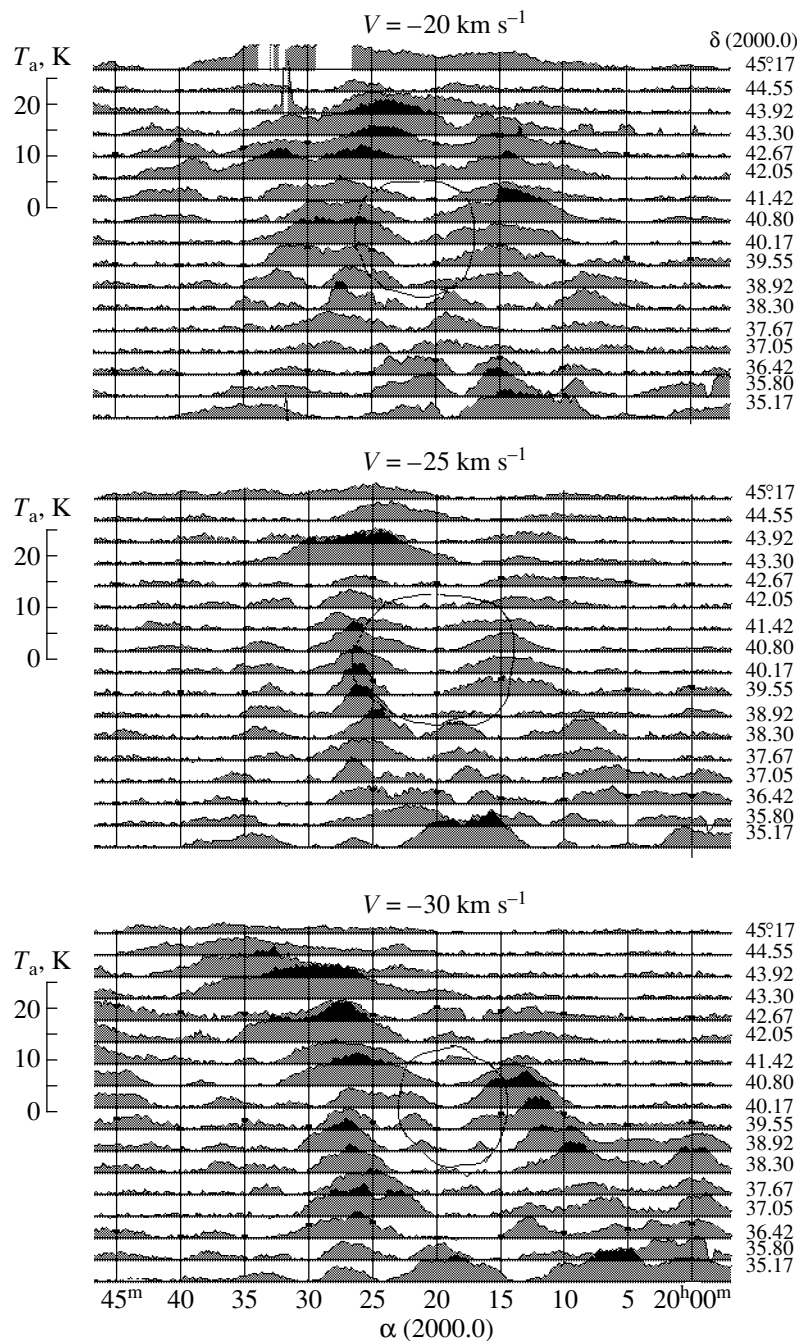
Fig. 3. Same as Fig. 1 at radial velocities of –20, –25, and –30 km s^{-1}. The thin lines represent the cavity that coincides in coordinates with the outer X-ray shell found by Lozinskaya *et al.* (2000) and shown in Fig. 2.

The possible association of H I features with the above objects in the radio, optical, and X-ray ranges was analyzed in the radial-velocity range –125 to +35 km s^{-1}. It turned out that, apart from the features at positive radial velocities noted by Gosachinskij *et al.* (1999), there is an interesting gas structure in the range –15 to –35 km s^{-1}. The distribution of H I features at radial velocities in the range –20 to –30 km s^{-1} is shown in Fig. 3. A comparison of this map with Fig. 2 reveals a distinct cavity or even an H I shell, which closely coin-

cides in coordinates and angular sizes with the outer X-ray shell from Lozinskaya *et al.* (2000). This shell has the following observed parameters:

Coordinates of the center α (2000.0) = 20^{h}20.0^m, δ (2000.0) = +40.8°;

Angular sizes 3.7° × 4.7° (inner) and 2.5° × 3.5° (outer);

Mean brightness temperature of the line 12.0 ± 0.5 K;

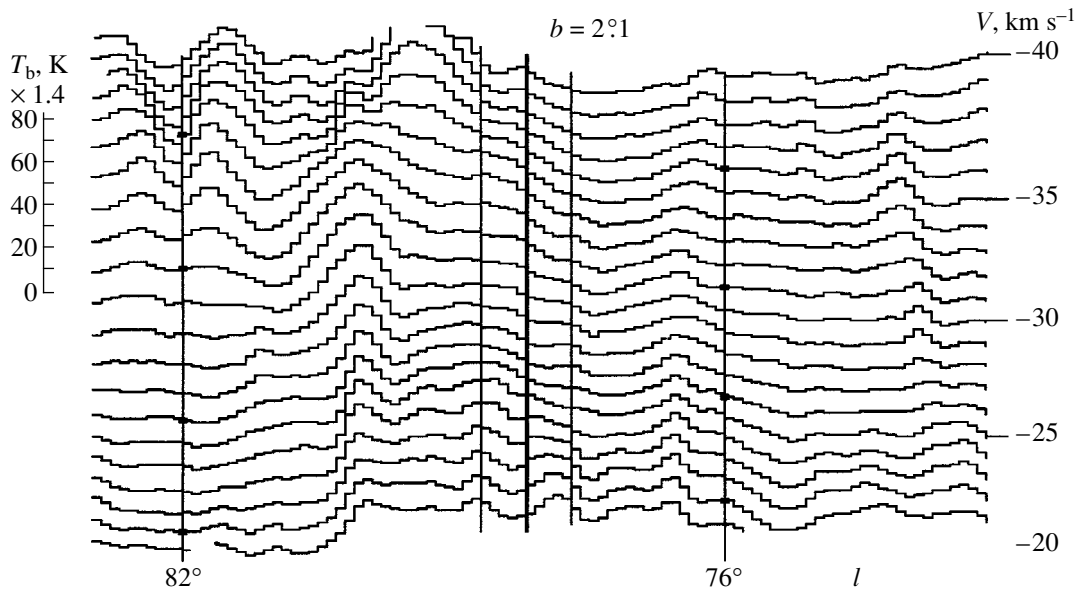Mean radial velocity –25 km s^{-1};

Fig. 4. The distribution of H I-line brightness temperature in the vicinity of G78.2 + 2.1 as constructed from data of the survey by Westerhout and Wendlandt (1982) with an angular resolution of 12′ and a radial-velocity resolution of 2 km s^{-1}. The source center (heavy lines) and the sizes at "zero" brightness temperature as inferred by Reich *et al.* (1990) at 11 cm are indicated.

The radial-velocity range in which the H I shell was observed ±10 km s^{-1}.

Note also that the angular sizes of the shell are at a maximum at a radial velocity of –25 km s^{-1}; this velocity can thus be considered to be the mean for the object. At lower and higher radial velocities, the angular sizes of the ring-like structure decrease, while the center slightly displaces in right ascension. Such an isophotal structure is characteristic of a shell with a large-scale radial velocity component (expansion) and rotation. Nevertheless, it should be noted that the cavity is not quite circular and is elongated from north to south. Thus, it cannot be reliably interpreted as an expanding shell. However, in the radial-velocity range studied, we failed to detect any other H I features whose morphology would correspond so closely to the outer X-ray shell found by Lozinskaya *et al.* (2000).

Whether the ring-like structure that we detected in the H I distribution is real can be verified, for example, by using data from a survey made with the 90-m NRAO radio telescope with an angular resolution of 12′ and a radial-velocity resolution of 2 km s^{-1} (Westerhout and Wendlandt 1982). Data from this survey are now accessible via the Internet in the ADS archive (Strasburg). Figure 4 shows the distributions of H I-line brightness temperature in Galactic longitude taken from this survey at the source latitude $b = +2.1°$ in the radial-velocity range –20.0 to –40.0 km s^{-1}. The heavy and thin vertical lines mark, respectively, the position of the SNR center and its sizes at "zero" continuum radio brightness as inferred by Reich *et al.* (1990). There is a clear reduction in H I-line intensity southwest of the SNR at longitudes 76°–77°. This effect is at a maximum at

radial velocities of about –30 km s^{-1}. Of course, the H I distribution from Westerhout and Wendlandt (1982) differs in details from our distribution, particularly the mean radial velocity of the cavity on the profiles in Fig. 4. This can be explained, first, by a marked difference between the antenna beam shapes and a different radial-velocity resolution and, second, by the fact that Westerhout and Wendlandt (1982) provided data only for the southeastern part of the cavity up to $b = +2.4°$.

Lozinskaya *et al.* (2000) measured the Hα radial velocities in the G78.2 + 2.1 region. It turned out that there is a secondary peak of the line profile at radial velocities in the range –20 to –45 km s^{-1} outside the bright remnant, but inside the outer weak X-ray shell, which closely corresponds to the velocity range of the H I shell, we detected and confirms that it is real. However, Lozinskaya *et al.* (2000) point out that the above velocity range is also observed in the Hα profiles in the broader region of the Cygnus X source.

The question arises as to whether the two objects, which can be characterized as a supernova remnant, on the one hand, and as an outer X-ray shell of a large diameter, on the other, are interrelated. In the range of Galactic longitudes under study, the objects in the Orion–Cygnus arm have radial velocities of Galactic rotation within ±5 km s^{-1} for any Galactic-rotation models (see Burton and Gordon 1978; Kerr and Linden Bell 1986). Given the peculiar velocities and systematic noncircular motions, this range extends to ±15 km s^{-1}. The radial velocity –25 km s^{-1} is well outside this range and formally corresponds to a distance of 6 kpc from the sun in the most compact Galactic-rotation model by Gluskova *et al.* (1998).

Of course, we can assume that these objects spatially coincide and that the radial-velocity difference is explained by their internal kinematics, for example, by radial motions. However, there are no clear traces of interaction between these objects in the H I distribution at radial velocities between +3 and –25 km s^{-1}. Therefore, we believe a chance projection of these objects to be most likely. This comes as no surprise in a region that is so rich in objects of a different nature: the SNR G78.2 + 2.1 itself is projected onto the Cygnus X thermal complex, while the well-known gaseous nebula around the star γ Cyg is projected onto the SNR shell.

CONCLUSION

A thorough analysis of the H I distribution in the G78.2 + 2.1 region over a wide radial-velocity range has revealed an extended expanding elliptical H I shell, $\approx 3°$ in diameter, at radial velocities from –10 to –25 km s^{-1}, which closely coincides in coordinates and angular sizes with the outer X-ray shell from Lozinskaya *et al.* (2000). The Hα emission investigated by the above authors in the SNR region also has a secondary peak inside the outer shell at radial velocities from –45 to –20 km s^{-1}. Since the radial velocities of the SNR with the inner X-ray shell and of the outer X-ray shell with the H I shell and Hα-emitting regions differ markedly, their distances can be assumed to differ as well; i.e., we observe a chance projection of two distinct objects, which is not surprising for the Cygnus region under study. Of course, if subsequent observations in all ranges will reveal unquestionable evidence for a physical association of these remarkable objects, then this simplest interpretation will have to be rejected.

ACKNOWLEDGMENTS

REFERENCES

1. W. B. Burton and M. A. Gordon, Astron. Astrophys. **63**, 7 (1978).
2. E. V. Glushkova, A. K. Dambis, A. M. Mel'nik, and A. S. Rastorguev, Astron. Astrophys. **329**, 514 (1998).
3. I. V. Gosachinskij, T. A. Lozinskaya, and V. V. Pravdikova, Astron. Zh. **76**, 453 (1999) [Astron. Rep. **43**, 391 (1999)].
4. D. A. Green, in *Proceedings of the IAU Colloquium No. 145 on Supernovae and Supernova Remnants*, Ed. by R. McCray and Z. Wang (Cambridge Univ. Press, Cambridge, 1996), p. 419.
5. L. A. Higgs, T. L. Landecker, and R. S. Roger, Astron. J. **82**, 718 (1977).
6. F. G. Kerr and D. Linden Bell, Mon. Not. R. Astron. Soc. **221**, 1023 (1986).
7. T. L. Landecker, R. S. Roger, and L. A. Higgs, Astron. Astrophys., Suppl. Ser. **39**, 133 (1980).
8. T. A. Lozinskaya, V. V. Pravdikova, and A. V. Finogenov, Pis'ma Astron. Zh. **26**, 102 (2000) [Astron. Lett. **26**, 77 (2000)].
9. A. Piepenbrink and H. J. Wendker, Astron. Astrophys. **191**, 313 (1988).
10. W. Reich, E. Fuerst, P. Reich, and K. Reif, Astron. Astrophys., Suppl. Ser. **85**, 633 (1990).
11. A. P. Venger, I. V. Gosachinskij, V. G. Grachev, and N. F. Ryzhkov, Izv. SAO **14**, 118 (1979).
12. R. Weaver, R. McCray, J. Castor, *et al.*, Astrophys. J. **218**, 377 (1977).
13. G. Westerhout and H. U. Wendlandt, Astron. Astrophys., Suppl. Ser. **49**, 137 (1982).
14. J. C. Wheeler, T. J. Masurek, and A. Sivaramakrishnan, Astrophys. J. **237**, 781 (1980).

Translated by V. Astakhov

Nucleosynthesis of Heavy Elements: Computational Experiment

I. V. Panov[1]*, S. I. Blinnikov[1], and F.-K. Thielemann[2]

[1] *Institute for Theoretical and Experimental Physics, ul. Bol'shaya Cheremushkinskaya 25, Moscow, 117259 Russia*
[2] *Institute for Theoretical Physics, Basel University, Basel, Switzerland*
Received September 29, 2000

Abstract—The kinetic-model (KM) efficiency in heavy-element nucleosynthesis calculations is analyzed. Various nucleosynthesis conditions and various mathematical models are considered. All basic two-particle reactions with neutrons, protons, α particles, and photons are taken into account. The results for the nuclear statistical equilibrium (NSE) model and for the KM are compared under various ambient conditions. The time it takes for the solution to become a steady-state one is estimated in the KM, provided that the NSE approximation holds. The computational processor time for temperatures $T < 8 \times 10^9$ K is shown to be modest, and the KM can be used for nucleosynthesis calculations in this range. The KM can be realized together with the NSE model at higher initial temperatures, with the results being smoothly joined by using the NSE solution as the initial KM approximation. The kinetic model can also be successfully used to compute the *r*-process under various physical conditions. © *2001 MAIK "Nauka/Interperiodica".*

Key words: *nuclear astrophysics*

INTRODUCTION

Different physical and mathematical nucleosynthesis models are used at different stages of stellar evolution. At high temperatures and densities, nuclear statistical equilibrium (NSE) is a simple and reliable approximation. The question of whether this approximation is applicable has been repeatedly discussed when investigating various physical processes: nuclear equilibrium in stars (Imshennik *et al.* 1981; Imshennik and Khokhlov 1983), β-processes (Imshennik *et al.* 1967), *r*-process (Cameron *et al.* 1983a; Lyutostanskiĭ *et al.* 1986), and the special case of NSE (QSE) (Hix and Thielemann 1999a).

For nuclei ranging from silicon to the iron-peak elements and with reaction energies of the order of 10 MeV, photonuclear reactions begin to play a significant role only at temperatures above 3×10^9 K. NSE is established at such or still higher temperatures, but this takes some time: the higher the temperature, the smaller the time. When the excess of neutrons (or protons) over stable nuclei is large enough, the typical NSE time scale considerably decreases. In each specific case, however, the NSE time scale can depend, in particular, on the accuracy of the initial solution and on the number of the nuclei and particles included in the analysis. For example, for neutron-rich nuclei typical of the *r*-process, the NSE approximation is applicable

(with respect to reactions with neutrons) even at temperatures $T = 10^9$ K (Cameron *et al.* 1983a) and, in several cases, at lower temperatures, especially at a sufficiently high density of free neutrons ($n_n > 10^{24}$ cm^{-3}).

At the stage of explosive nucleosynthesis, when a massive supernova explodes, the ambient parameters change rapidly compared to the NSE time scale, so the NSE approximation can often be inapplicable, and other models should be used. In this case, we must take into account all the possible nuclear reactions between all types of nuclei and particles that synthesize new nuclei and chemical elements (in most cases, it will suffice to take into account only paired nuclear reactions and some others, for example, the triple-3-α reaction), which requires the kinetic model (KM).

Here, we discuss the following two basic issues: (i) the use of different models at different stages of the process under consideration and a neat transition from one model to another; (ii) the mutual integral testing of various codes and determining their efficiency, including estimating the efficiency of the previously developed KM (Blinnikov and Panov 1996; Nadyozhin *et al.* 1998), when the NSE model is applicable, as well as determining the KM efficiency at the dynamic stages of physical nucleosynthesis scenarios in inner supernova regions.

From the very outset [the theoretical foundations of thermodynamic equilibrium were formulated by Pokrowski (1931)], the theory of statistical equilibrium has been appealing, in particular, computationally. Only the binding energies and partition functions of all the

* E-mail address for contacts: panov@vitep5.itep.ru

nuclear ingredients involved in a reaction must be known for calculations. The equilibrium approximation is also attractive, because calculations are simple; it can be used to obtain useful results when considering various problems (such as the *r*-process, explosive nucleosynthesis, etc.). The latest results obtained by Hix and Thielemann (1999a, 1999b) in the NSE approximation provide a deeper understanding of the details of silicon nuclear burning.

The NSE-based models developed in the 1960s (see Bogansky *et al.* 1968) are simple and reliable enough, but their application to physical processes makes sense only when several physical conditions determined by NSE model parameters are satisfied. In particular, the time t_{NSE} it takes for NSE to be established must be much smaller than the time scale t_τ of the process under consideration. Otherwise, the solution of the problem can be incorrect or completely impossible. In addition, the computational time required for the problem to be solved must be reasonable.

We used the KM to solve heavy-nuclei nucleosynthesis problems, such as determining the yields of isotopes when iron-group elements are synthesized in presupernova inner shells at various temperatures and densities, and to compute the *r*-process. These two processes, the *r*-process and the equilibrium synthesis of iron-peak elements, were considered for the following reasons, which seem important.

Since the *r*-process is one of the two limiting processes with neutrons in which heavy elements are synthesized, its calculation is cumbersome and time consuming, while the results can be obtained only based on a number of theoretical models. At the same time, the synthesis of iron-peak elements (as well as lighter elements) is of great importance, because the iron-group elements, on the one hand, are the end products of equilibrium and explosive nuclear burning and, on the other, are apparently the seed (starting) nuclei for the *r*-process. The NSE approximation is a major approach to modeling the synthesis of intermediate and iron-group elements. The KM must be used for the *r*-process and for any other dynamic explosive processes.

Progress in understanding both the *r*-process and the processes at equilibrium burning stages described by the NSE approximation is complicated by cumbersome calculations and by ambiguity in interpreting the results. It is therefore important to have a reliable tool for computational astrophysics, carefully tested computer codes.

THE MODEL

Let us briefly describe the previously developed KM of nucleosynthesis (Blinnikov and Panov 1996; Nadyozhin *et al.* 1998; Panov and Nadyozhin 1999), in which the change in the fraction of each nuclide (A, Z) is given by

$$
\begin{aligned}
dY_{A,Z}/dt = {} & -\lambda_\beta(A, Z)Y_{A,Z} + \sum_{i=1,2,3} i\lambda_\beta(A, Z)P_i(A, Z)Y_{A,Z} \\
& -\lambda_{n\gamma}(A, Z)Y_{A,Z} + \lambda_{n\gamma}(A-1, Z)Y_{A-1,Z} \\
& -\lambda_{\gamma n}(A, Z)Y_{A,Z} + \lambda_{\gamma n}(A+1, Z)Y_{A+1,Z} \\
& -\lambda_{p\gamma}(A, Z)Y_{A,Z} + \lambda_{\gamma p}(A+1, Z+1)Y_{A+1,Z+1} \\
& -\lambda_{\gamma p}(A, Z)Y_{A,Z} + \lambda_{p\gamma}(A-1, Z-1)Y_{A-1,Z-1} \\
& -\lambda_{\alpha\gamma}(A, Z)Y_{A,Z} + \lambda_{\gamma\alpha}(A+4, Z+2)Y_{A+4,Z+2} \\
& -\lambda_{\gamma\alpha}(A, Z)Y_{A,Z} + \lambda_{\alpha\gamma}(A-4, Z-2)Y_{A-4,Z-2} \\
& -\lambda_{np}(A, Z)Y_{A,Z} + \lambda_{np}(A, Z+1)Y_{A,Z+1} \\
& -\lambda_{pn}(A, Z)Y_{A,Z} + \lambda_{pn}(A, Z-1)Y_{A,Z-1} \\
& -\lambda_{p\alpha}(A, Z)Y_{A,Z} + \lambda_{\alpha p}(A-3, Z-1)Y_{A-3,Z-1} \\
& -\lambda_{\alpha p}(A, Z)Y_{A,Z} + \lambda_{p\alpha}(A+3, Z+1)Y_{A+3,Z+1} \\
& -\lambda_{\alpha n}(A-3, Z-2)Y_{A-3,Z-2} - \lambda_{\alpha n}(A, Z)Y_{A,Z} \\
& +\lambda_{n\alpha}(A, Z)Y_{A,Z} - \lambda_{n\alpha}(A+3, Z+2)Y_{A+3,Z+2},
\end{aligned}
\tag{1}
$$

where λ_{ij} are the rates of various reactions. For two-particle reactions, $(A, Z) + i \longrightarrow (A_f, Z_f) + j$, we have

$$
\lambda_{ij}(A, Z) = Y_i(t)\rho(t)N_A\langle\sigma_{ij}(A, Z)v\rangle,
$$

where $i = $ n, p, α and $j = $ n, p, α, γ.

The rates of reverse photodissociation (γ, i) reactions can be determined via the rates of direct (i, γ) reactions (Fowler *et al.* 1967),

$$
\lambda_{\gamma i}(A, Z) = C^i_{AZ}N_A\langle\sigma_{i\gamma}(A-A_i, Z-Z_i)v\rangle,
$$

where

$$C_{AZ}^i = 0.987 \times 10^{10} \frac{g_i g_{A-A_p, Z-Z_p}}{g_{A,Z}} \left[\frac{A_p (A-A_p)}{A} T_9 \right]^{3/2}$$

$$\times \exp\left(-Q_{i\gamma} \frac{11.605}{T_9}\right) \text{g cm}^{-3}.$$

Here, $A_p = 1, 1, 4$, $Z_p = 0, 1, 2$, and $g_p = 2, 2, 1$ for n, p, and α, respectively; T_9 is the temperature (in units of 10^9 K); $Q_{i\gamma}$ is the energy (in MeV) released in the corresponding direct (n, γ), (p, γ), and (α, γ) reactions: $(A - A_p, Z - Z_p) + i \longrightarrow (A, Z) + \gamma + Q_{i\gamma}$.

Note that the terms in Eq. (1) that allow for reactions with neutrinos and delayed fission were discarded in our calculations.

The fractions of neutrons, protons, and α particles are given by the following equations, which are solved simultaneously with Eq. (1):

$$dY_n/dt = -\sum_Z \sum_A \left(\lambda_{n\gamma} - \lambda_{\gamma n} + \lambda_{np} + \lambda_{n\alpha} - \lambda_{\alpha n} - \lambda_{pn} \right.$$

$$\left. - \sum_{k=1,2,3} k\lambda_\beta(A,Z) P_k(A,Z) \right) Y_{A,Z},$$

$$dY_p/dt$$

$$= -\sum_Z \sum_A (\lambda_{p\gamma} - \lambda_{\gamma p} + \lambda_{p\alpha} - \lambda_{\alpha p} + \lambda_{pn} - \lambda_{np}) Y_{A,Z}, \quad (2)$$

$$dY_\alpha/dt$$

$$= -\sum_Z \sum_A (\lambda_{\alpha\gamma} - \lambda_{\gamma\alpha} + \lambda_{\alpha p} + \lambda_{\alpha n} - \lambda_{n\alpha} - \lambda_{p\alpha}) Y_{A,Z},$$

where

$$Y_{A,Z} = \frac{n(A,Z)}{\rho N_A}, \quad Y_n = \frac{n_n}{\rho N_A}, \quad Y_p = \frac{n_p}{\rho N_A},$$

$$Y_\alpha = \frac{n_\alpha}{\rho N_A}. \quad (3)$$

The total number of the nuclei considered in nucleosynthesis calculations and, accordingly, the number of equations (1) depends on the choice of an integration range and mass formulas.

Since the reaction rates for the above processes, which determine the eigenvalues of the Jacobian matrix for Eqs. (1) and (2), differ in absolute value by several orders of magnitude, this system of equations is a classical example of a stiff system of ordinary differential equations. Many methods have been developed to numerically integrate such systems. We used one of the most efficient methods, the method of Gear (1971) modified by Brayton *et al.* (1972). Special software was

developed for its implementation (Blinnikov and Bartunov 1993; Blinnikov and Dunina-Barkovskaya 1994). The predictor-corrector method with the automatic choice of a step and order of the method underlies the algorithm. The main difficulty in implementing this algorithm is the necessity of solving a very large system of linear equations [of the order of several thousand, by the number of equations in Eqs. (1) and (2)] when making corrector iterations. This difficulty also arises in other implicit methods, for example, in the simple implicit method of Euler polygonal lines. Since the matrix of coefficients in this system is sparse, special methods developed for sparse matrices (see, e.g., Pissanetzky 1984) can be used for its solution; the choice of a method for solving a sparse system has a crucial effect on the efficiency of the entire algorithm for a kinetic problem.

A description of the full software package and the model application to *r*-process calculations can be found in Blinnikov and Panov (1996).

Another promising approximate approach to calculating stiff systems of differential equations based on a transformation from differential equations to algebraic ones was developed by Thielemann with his coworkers (Cowan *et al.* 1991; Rembges *et al.* 1997; Freiburghaus *et al.* 1999; Hix and Thielemann 1999b).

RESULTS OF CALCULATIONS

We performed several calculations with the KM, which allowed us to solve the system of equations (1) by an "exact" numerical method using the implicit scheme described above. We considered various physical conditions and scenarios, in which our calculations were compared and tested by calculations based on other computer codes and mathematical models.

The r-Process

The *r*-process calculations are perhaps the most cumbersome nucleosynthesis calculations, because the largest number of various isotopes with the largest possible spread in properties and characteristics are involved in the *r*-process.

We determined the range of nuclei involved in nucleosynthesis as follows: $Z_{min} = 14$ and $Z_{max} = 95$; the lightest stable isotope and the heaviest neutron-rich isotope (at the neutron stability boundary) were chosen, respectively, as the minimum and maximum values of A for each Z. When neutron-deficient unstable nuclei are included in analysis, the total number of nuclei and kinetic equations can reach 4000 or more. The exact number depends on the determination of neutron and proton stability boundaries, which are calculated by using mass formulas (i.e., it eventually depends on the choice of a mass formula), a starting region of the *r*-process, a fission model for transuranium nuclei, and the power of a free-neutron source. Thus, for example, the number of equations was 2800 and 3551 for the
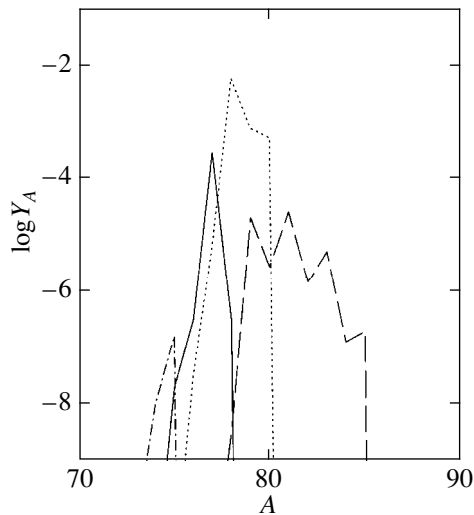
Fig. 1. KM calculations of equilibrium fractions for iron, cobalt, nickel, and copper for $n/p = 4$, $T_9 = 5.0$, and $\rho = 2 \times 10^9$ g cm^{-3}. The dash-dotted, solid, dotted, and dashed lines represent Fe, Co, Ni, and Cu, respectively.

mass formulas from Hilf *et al.* (1976) and Jänecke and Eynon (1976), respectively. In our KM calculations, the number of nuclei included in the *r*-process was 3100 (1188 ingredients were taken into account in the calculations of presupernova chemical composition performed for comparison with the NSE model).

We took (n, γ)-reaction rates, as well as photodissociation-reaction rates, mostly from Thielemann *et al.* (1987) and Cowan *et al.* (1991). Mass fractions and β-decay rates, as well as the emission probabilities of delayed neutrons, were determined by using predictions of the QRPA model [see Möller *et al.* (1997) for details].

Nuclear masses were calculated by using the FRDM-92 model (Kratz *et al.* 1993) with Coulomb corrections and with allowance for pairing effects that is more accurate than with other mass formulas (Möller and Hix 1992). The region with the magic number of neutrons $N = 82$, where the masses from Hilf *et al.* (1976) were used, constituted an exception [see Kratz *et al.* (1993) for more details]. Reactions with protons and α particles were disregarded in our *r*-process calculations.

As an example of modeling the *r*-process, we considered the classical model of a dynamic *r*-process. Here, "dynamic" means that the change in the fraction of free neutrons was reconciled with the change in the fraction of all nuclei, which was determined by simultaneously solving Eqs. (1) and (2). As the *r*-process medium, we considered a simple qualitative model (Hillebrandt 1978), when a small number of seed nuclei (for simplicity, we chose the nucleus of one of the iron-peak elements, which below is arbitrarily called "iron") were in a sea of free neutrons. The initial fractions of neutrons and iron were determined by introducing a

free parameter: the ratio of the numbers of neutrons and protons n/p, whose value was varied over the range 4 to 10 in our calculations.

At first, we verified the distribution of seed nuclei calculated in the NSE approximation for $\rho = 2 \times 10^9$ g cm^{-3} and $T_9 = 5$ (Hillebrandt 1978) with $n/p = 4$. We used the same initial data with ^{78}Ni as a seed nucleus. The isotopic Fe, Co, Ni, and Cu distributions calculated with the KM (Run R1) reproduced well the NSE distributions of the same isotopes, although different mass formulas and partition functions were used in the NSE and KM approaches (Fig. 1). In both cases, the nickel isotopes were most abundant, the copper yields were slightly underestimated in the KM calculations, while the cobalt yields were overestimated compared to NSE calculations (Hillebrandt 1978). Such distributions were obtained in the KM in time $t = 10^{-5}$ s and were constant for the entire computational time until $t_{fin} = 50$ s.

In our subsequent *r*-process calculations performed for these initial parameters (calculation R2), all nuclei from iron to uranium are synthesized before the neutron density drops below its critical value (10^{18} cm^{-3}), at which the *r*-process no longer proceeds. Note that for such parameters, it does not matter whether the fission is delayed or spontaneous (Panov *et al.* 2000), because the neutron density drops below its critical value when the nucleosynthesis wave reaches the transuranium region. We performed our calculations up to a physical time of 10 s; the density of free neutrons decreased in this time from 2.6×10^{23} to 2.6×10^{12} cm^{-3}. Most of the chemical elements were synthesized in 2 s (when the density of free neutrons changed only slightly and was ~10^{23} cm^{-3}), because the path of the *r*-process during this time passed along the neutron stability line over the nuclei with minimum half-lives. Subsequently, as increasingly heavy elements were synthesized, the neutron density rapidly decreased, the path of the *r*-process displaced into the region of longer-lived nuclei, the nucleosynthesis slowed down, and the synthesis of new elements continued only in the region of nuclei with $N \approx 82$ through the escape of the nucleosynthesis wave from the region of nuclei with short half-lives into the region of long-lived nuclei. At this time, β-decays and (γ, n) reactions begin to dominate over neutron captures. The results of our calculations (R2) are shown in Fig. 2.

Although, as we see from the figure, our calculated curve (solid line) closely follows the main structure of the solar abundance curve (dotted line), the yields of isotopes with $A > 130$ were appreciably overestimated. However, the positions of the peaks ($A \sim 130, 196$) are in excellent agreement with observations, which more likely confirms the "dynamic" nature of the *r*-process than the statistical model. In the latter model, it was impossible to obtain a close coincidence of the positions of all computed and solar peaks in a single event. If the model *r*-process conditions are invalid, then the positions of the peaks, especially of the second and third ones, will

displace from the peaks on the solar abundance curve [see, e.g., Lyutostanskiĭ *et al.* (1986); Kratz *et al.* (1993); and references therein].

The duration of this kind of calculation on a computer is modest: on an IBM RS3600, the calculation takes several minutes of processor time. However, for an actual physical model with rapidly changing conditions, the computational time increases by an order of magnitude because of the multiple recalculation of reaction rates and because of a reduction in integration step for the system of differential equations (1) and (2).

A third calculation (R3) was performed under typical conditions of nucleosynthesis in the hot bubble model (Witti *et al.* 1994). The region in a type II supernova produced by neutrino energy deposition from the collapsing core and characterized by the high temperature and density required for the *r*-process to proceed (Woosley and Hoffman 1992) is called a hot bubble. Just as in the above papers, we took the final results of hydrodynamic calculations as the initial conditions for the *r*-process. This means that the *r*-process started when the temperature decreased to $T_9 = 2.34$, when the reactions with charged particles froze out, and the reactions with neutrons and β decays became the main ones. The isotopes produced at the hydrodynamic stage, mostly by the α-process (Witti *et al.* 1994; Woosley and Hoffman 1992), acted as seed nuclei.

Just as was done by Freiburghaus *et al.* (1998), we took the cross sections of reactions with neutrons from the calculations by Cowan *et al.* (1991). The initial (for the *r*-process) fraction of neutrons was also taken from α-process calculations (Freiburghaus *et al.* 1998) performed for the following model parameters:

Initial bubble radius $R_0 = 3.82 \times 10^3$ km;

Expansion velocity $V = 4.5 \times 10^4$ km s^{-1};

$T_9 = 2.34$, $\rho = 1.09 \times 10^4$ g cm^{-3}, entropy $s = 270$.

Neutron fraction $Y_n = 0.0669$, and neutron excess $\eta = 0.04$.

The time dependence of temperature and neutron density was determined as follows (Freiburghaus *et al.* 1998):

$$t_9(t) = T_9(R_0/(R_0 + Vt));$$
$$\rho(t) = 1.21 \times 10^5 T_9^3/(1 + 7f/4), \qquad (4)$$

where $f = T_9^2/(T_9^2 + 5.3)$.

The *r*-process was computed until the neutron density dropped below $n_n = 10^{14}$ cm^{-3}, and the final densities were obtained after the chains of β-decay into stable nuclei (the decay time was assumed to be 10^{10} s). The final results of our calculations are shown in Fig. 3. The dashed line represents the calculations by Freiburghaus *et al.* (1998) based on an approximate model for solving the system of equations, AKM [see Hix and Thielemann (1999b) and references therein], which was developed in recent years by Cowan *et al.* (1991) and which is used to compute various types of
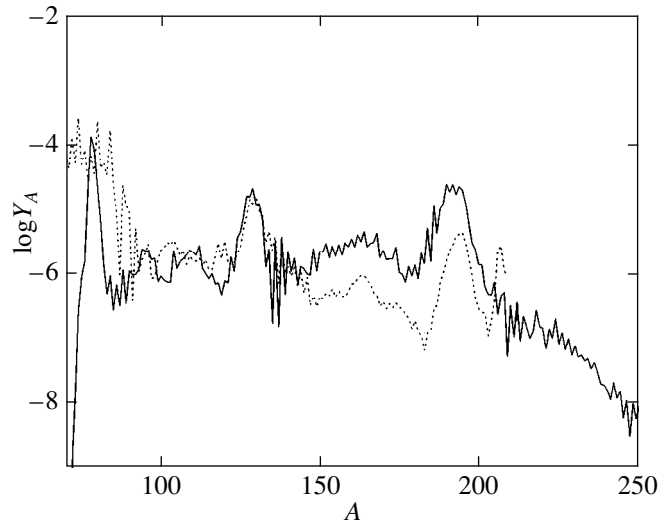
Fig. 2. Calculations of a classical *r*-process with initial ratio $n/p = 4$. The seed nucleus is ^{78}Ni; $T_9 = 1$; the path of the *r*-process passes over nuclei with neutron binding energy $S_n = 2$ MeV; the initial neutron density is $n_n = 2.6 \times 10^{23}$ cm^{-3}; the dotted line represents the solar *r*-element abundance curve (Käppeler *et al.* 1989).
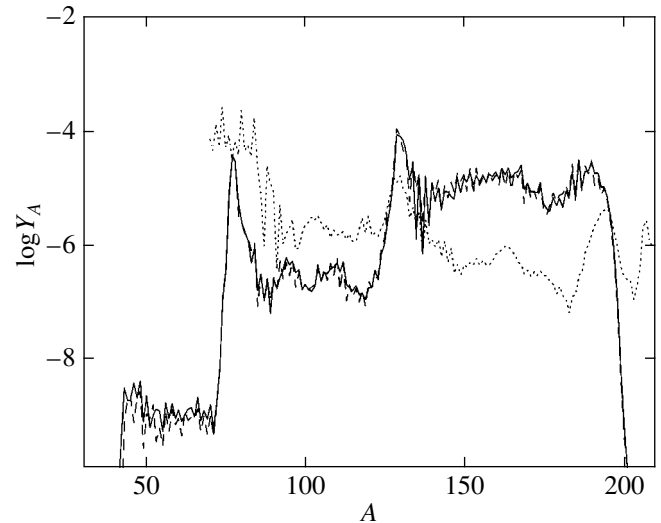
Fig. 3. KM calculations of the *r*-process using two different codes under conditions characteristic of the hot bubble model. The solid, dashed, and dotted lines represent our KM and AKM calculations and the solar *r*-process curve, respectively.

nucleosynthesis: carbon burning (Hix and Thielemann 1999a), the *rp*-process (Rembges *et al.* 1997), and the *r*-process (Freiburghaus *et al.* 1999).

The two mathematical models work well both for low-temperature nucleosynthesis characterized by a constant flow of matter (Cameron *et al.* 1983b) and at high temperatures, when the NSE approximation holds. However, transition cases where there is neither nuclear equilibrium nor a constant flow of nuclei, for example,

the case where β-decay is one of the leading nucleosynthesis reactions (Blinnikov *et al.* 1995), are of greatest interest. The developed mathematical models that we test here by comparing the results of calculations between themselves and with the results of other codes are primarily needed for such problems.

As we see from the above discussion, the results of different calculations based on the two mathematical models and computer codes reproduce each other well. Small differences (especially in calculations R1 and R2) can be explained as follows: (1) by a discrepancy in the data used, primarily in the emission probabilities of delayed neutrons (and in the difference mass formulas and partition functions used for R1); and (2) by a partial noncoincience of the boundaries of the nucleosynthesis region under consideration, i.e., by the different number of the nuclei involved in the models (and also by the accuracy of mathematical models for R3).

Under completely identical conditions of the problem and for the same nuclear data, although the KM and AKM results reflect similarly an odd-even dependence on the abundance curve (Panov *et al.* 2000), they exhibit a modest (in absolute value), but systematic, discrepancy. The latter appears as a price for simplifying and speeding up the calculations; for a number of problems, this inaccuracy (a few percent) can be of little importance.

NSE Calculations

Since the typical energy thresholds of photodissociation reactions for most intermediate nuclei and iron-peak nuclei near the stability valley is ~10 MeV, (γ, X) reactions begin to significantly affect nucleosynthesis only at temperature is above 3×10^9 K. The NSE approximation is therefore applicable only under these conditions.

Here, we will not discuss differences between the NSE and QSE models [a detailed list of papers on this subject can be found in Imshennik and Khokhlov (1983) and Hix and Thielemann (1999a)] and temporal characteristics of equilibrium establishment in these models.

For our NSE calculations, we used the model that was described in detail by Blinnikov *et al.* (2001). The method of NSE calculation described by the above authors was aimed at high-density regions (up to 10^{12} g cm^{-3}), in which the nonideal effects of a nuclide gas and, at high temperatures, the excitation of nuclei must be taken into account. Here, we considered slightly different NSE conditions, and not all of the effects taken into account in the NSE code were included in the kinetic scheme (1) and (2).

We determined the range of nuclei in which nucleosynthesis was considered as follows: $Z_{min} = 3$ and $Z_{max} = 45$; in the KM, all isotopes between the neutron and proton stability boundaries were taken into account for each element. The total number of elements and kinetic equations in our problem was 1188 [the stability boundaries were determined by using the mass formula from Hilf *et al.* (1976)].

We applied the two models described above (NSE and the KM) to compute the same physical scenario (under NSE applicability conditions). In both computer codes implementing the NSE and KM models, the same mass formula (Hilf *et al.* 1976) was used to compute nuclear masses and binding energies. In our KM calculations, we considered the solution (fractions $Y_{A, Z}$) obtained in the NSE model for the corresponding excess of neutrons $\eta = 1 - 2Y_e$, where Y_e is the electron fraction, as the initial approximation.

The main results of our calculations are shown in Figs. 4–6. It is clear from these figures that for $Y_e = 0.48$, the NSE approximation works well not only at high temperatures ($T_9 \sim 10$), but also at $T_9 = 5$. The differences in different models were appreciable only for the ^{8}Be isotope, whose instability against α-decay was ignored in both models.

In the scenario in question, the NSE time scale is $t_{eq} \sim 10^{-8}$–10^{-4} s, depending on the conditions considered. This is consistent with the conclusions of Imshennik *et al.* (1981) and Imshennik and Khokhlov (1983), who found the NSE time scale at densities $\rho \geq 10^7$ cm^{-3} to be no less than 1 s for $T_9 = 5$ and 10^{-5} s for $T_9 = 9$, respectively. The lower the temperature, the larger the equilibrium time scale. However, the equilibrium time scale in the KM also depends on the degree of neutronization: thus, for example, the equilibrium time scale for $Y_e = 0.36$ is larger than that for $Y_e = 0.48$ (Fig. 5).

For the neutron, proton, and α-particle fractions $Y_n(t)$, $Y_p(t)$, and $Y_\alpha(t)$ determined via the fractions of all the involved nuclei, the discrepancy generally did not exceed ~20%. [The isotopic fraction $Y_{A, Z}(t)$ changes with time smoothly, becoming constant in a time corresponding to the NSE time scale]. Because of the selected scheme for determining the fractions of neutrons, protons, and α particles and because of the method used, Y_n, Y_p, and Y_α can oscillate with time near the sought-for solutions. However, the oscillation amplitude generally does not exceed 0.1%. It can be reduced by increasing the accuracy of the method and by the corresponding decrease in step, causing the computational time to increase considerably, which, in our view, is pointless when the error is small.

Insignificant discrepancies (see Figs. 4 and 5) for small neutron excess ($Y_e > 0.45$) can be explained by different calculations of partition functions and by differences in the binding energies used for light elements. The boundary effect, which is attributable to a deficiency of neutron-rich isotopes in our NSE calculations and which leads to appreciable discrepancies in the KM and NSE solutions, increases with neutron excess (Figs. 4b, 4c, and 5b). The discrepancies in the results obtained in the two approaches under consideration result mainly from differences in the number and composition of the isotopes involved in the models: the KM
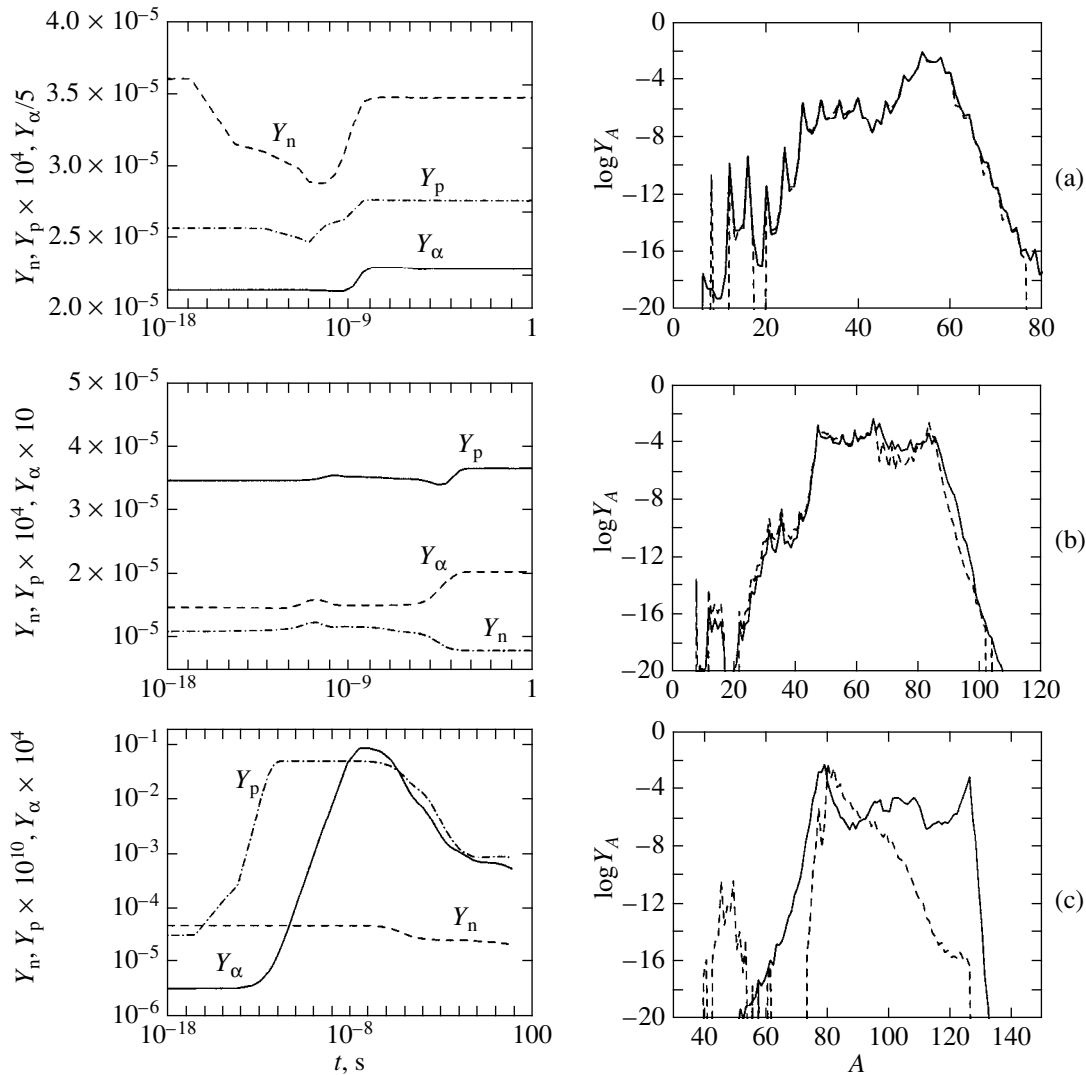
Fig. 4. Comparison of the NSE and KM solutions for $T_9 = 5$ at $Y_e = 0.48$ (a), 0.42 (b), and 0.36 (c). The left panels show NSE establishment for Y_n, Y_p, and Y_α with the initial NSE approximation $Y_i(0)$; the right panels compare the final (solid line) and initial (dashed line) abundance Y_i.

considers all neutron-rich isotopes with $Z > 2$ and does not include hydrogen and helium isotopes, while the NSE code does not include all neutron-rich isotopes, but takes into account hydrogen and helium isotopes more accurately.

For example, the NSE solution at low Y_e and $T_9 = 5$ is not exact, because some of the neutron-rich isotopes whose fraction must be appreciable was not included in the computational NSE scheme (as was noted above, the discrepancies in the determination of isotope ranges stem from the fact that the NSE code was written to determine the chemical composition at very high temperatures and pressures for $Y_e \sim 0.45$). For this reason, the discrepancies between the results are appreciable for $Y_e = 0.36$ and considerably decrease with increasing model parameter Y_e. The physical equilibrium time scale in the KM also decreases with increasing Y_e.

We see from these comparative calculations that NSE calculations for low Y_e and $T_9 \leq 0.4$ must include all neutron-rich isotopes up to the neutron stability boundary.

The initial isotopic composition for our KM calculations was computed by using the NSE code (Blinnikov *et al.* 2001). We also performed calculations with a "bad" initial composition corresponding to slightly different initial conditions. In this case, as we see from our calculations (Fig. 6a), the abundances of the heaviest nuclei are lower (the region of the peak with masses $A > 60$), while the abundances of other nuclei are higher. An equilibrium distribution is also established rapidly in this case, despite discrepancies in the initial approximation, primarily in $Y_n(t)$, $Y_p(t)$, and $Y_\alpha(t)$ (approximately by 20–30% compared to the "good" solution in Fig. 5), although it leads to a redistribution
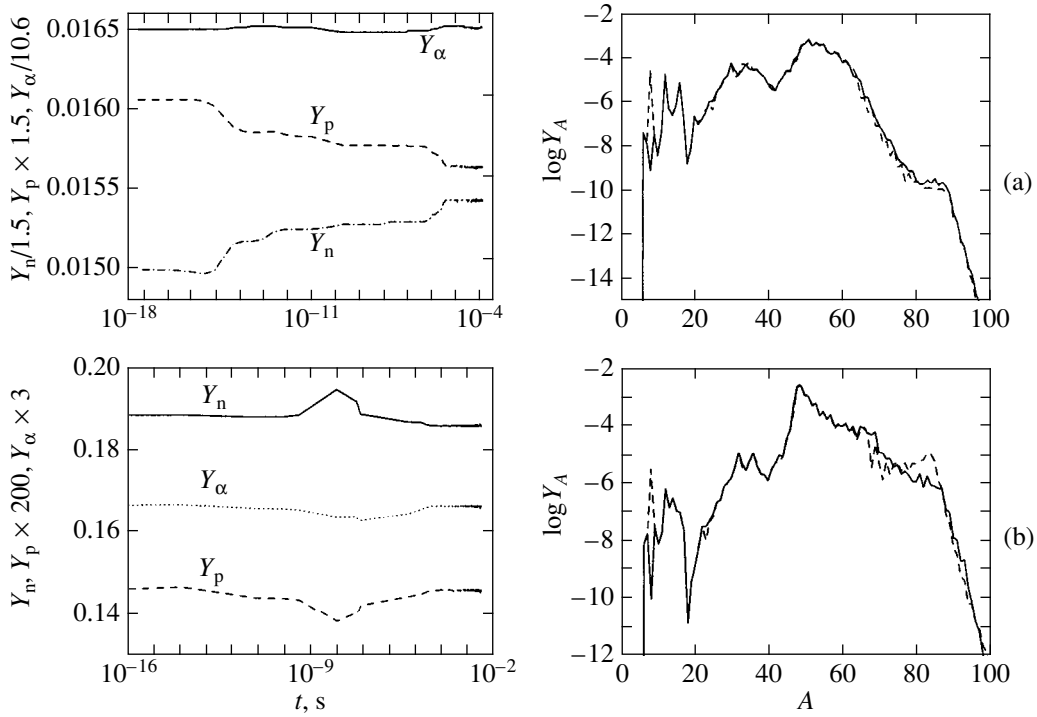
Fig. 5. Comparison of our NSE and KM calculations of Y_i for $T_9 = 10$ at $Y_e = 0.48$ (a) and 0.36 (b). The notation is the same as in Fig. 4.
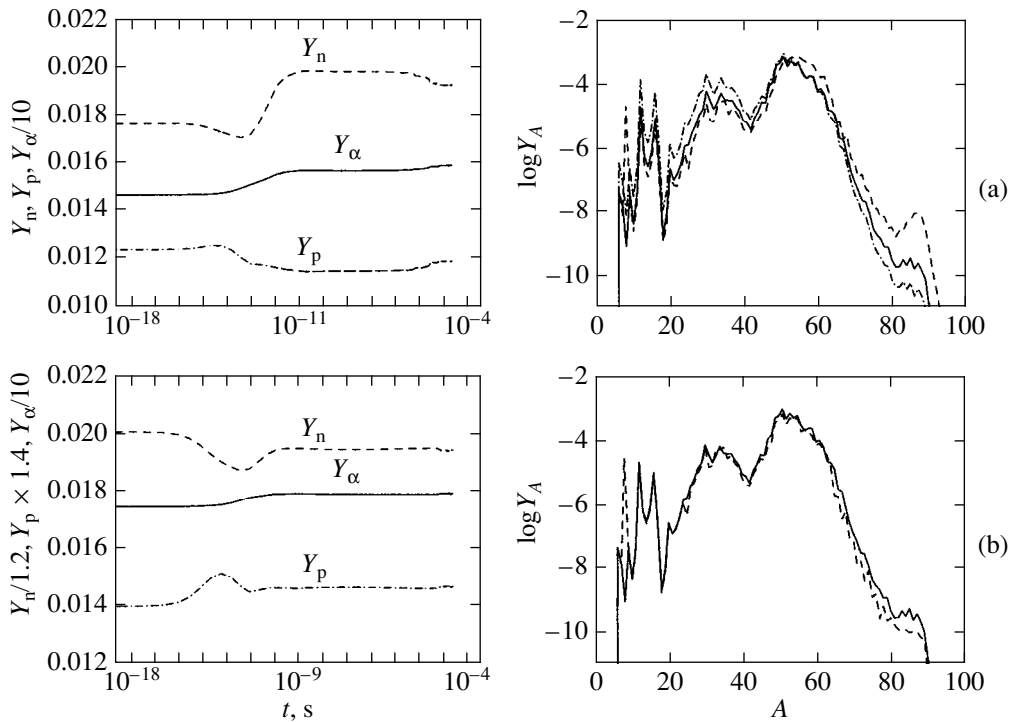
Fig. 6. Effects of the initial approximation on the final result of KM calculations for $T_9 = 10$ and $Y_e = 0.48$. The left panels show how Y_n, Y_p, and Y_α obtained in the NSE model approach their equilibrium values. The right panels compare the initial (NSE) and final (KM) abundances of isotopes with masses A. The solid line represents the final KM solution for the exact initial approximation; (a) the dashed and dash-dotted lines represent the "bad" initial and final solutions, respectively; (b) the dashed line represents our KM calculations with the "bad" initial distribution of all elements with $Z > 2$, but Y_n, Y_p, and Y_α were taken from the "good" calculations (Fig. 5a).

of the isotope yields. Recall that $Y_n(t)$, $Y_p(t)$, and $Y_\alpha(t)$ are determined as algebraic sums of the yields of isotopes with $A > 2$. That is why they are very sensitive to any changes of the conditions in our calculations. On the other hand, the reaction rates directly depend on Y_n, Y_p, and Y_α. For $Y_e = 0.42$, the rates of (n, α) and (α, n) reactions are almost equal for the majority of the most abundant nuclei; therefore, the increase in the NSE time scale can be explained by the effect of a decrease in the rate of nucleosynthesis flow.

At first glance, the results in Fig. 6a show a relatively high sensitivity of the KM to the choice of an initial approximation and a low stability of the solution in such a large system of equations. However, according to our additional calculations with "corrected" $Y_n(t)$, $Y_p(t)$, and $Y_\alpha(t)$ (Fig. 6b), this is not always the case. Our additional calculations were performed for $T_9 = 10$ and $\rho = 10^9$ cm^{-3} with the "bad" initial approximation for $Z > 2$ (as in Fig. 6a), but with the correct fractions Y_n, Y_p, and Y_α (as in Fig. 5). The results of these calculations (Fig. 6b) show a relatively high stability of the solution (at least for $Y_e = 0.48$) for the fractions of elements with $Z > 2$ and a high sensitivity of the solutions Y_n, Y_p, and Y_α to initial data. The fractions Y_n, Y_p, and Y_α are established faster, while the difference between their final values and the initial solution is much smaller than that for the case in Fig. 6a. This implies that the KM calculations strongly depend on the accuracy and reliability of evolutionary calculations, from which the initial conditions and time profiles $T_9(t)$ and $\rho(t)$ are taken. On the other hand, these results (Fig. 6b) once again emphasize good agreement between the NSE and KM approximations despite a difference between the isotopic compositions in our calculations for $Y_e < 0.48$.

CONCLUSION

In general, the results of our calculations based on various mathematical models and computer codes are similar in the range of those conditions for which they are applicable. Small discrepancies in the results can be explained by the following factors: (1) the KM and NSE models had discrepancies in the nuclear data, in particular, in the partition functions and emission probabilities of delayed neutrons; (2) a difference in the numbers of included isotopes, which was crucial, especially for enhanced neutron excess; and (3) different requirements to the accuracy of mathematical methods of solution, which can occasionally exceed the KM computer accuracy (for example, in determining the reaction flow via the difference between the flows of direct and reverse reactions, when the flows are large, while the difference can be near computer zero. The latter circumstance must also be taken into account when performing calculations on different computers and with different software.

Our r-process calculations with different computer codes based on different mathematical methods and algorithms yielded identical results, which can now be considered much more reliable. A comparison of our NSE and KM calculations indicates that for strongly neutronized matter ($Y_e < 0.3$) and temperatures $T \leq 7 \times 10^9$ K, the range of the nuclei under consideration must include all neutron-rich nuclei up to the neutron stability boundary. In other cases (for $Y_e > 0.3$ and $T > 7 \times 10^9$ K), our calculations using both codes agree even though there are discrepancies in the scenario conditions and initial data (see above).

Our integral test revealed the effective applicability ranges for the codes that implement different mathematical models (KM, AKM, and NSE). Thus, for example, the code based on Gear's implicit method and initially written for r-process calculations can be used for various nucleosynthesis calculations of heavy nuclei with allowance for reactions with charged particles. For a rapid change in physical conditions during collapse, when the hydrodynamic time scale $t_n \leq t_{NSE}$, the NSE approach is inapplicable. If, however, the ambient temperature and density are so high that the KM requires more processor time for calculations, it is cheaper and easier to use other codes based on simplified mathematical models, for example, AKM (Hix and Thielemann 1999b). Note that in consistent model calculations of chemical composition under the conditions of cooling and a reduction in matter density characteristic of explosive processes, the transition from NSE to the KM is most convenient at $T \approx (5-6) \times 10^9$ K, when NSE and the KM give equivalent solutions and the transition from NSE and the KM is simple, does not produce any nonphysical solutions, and is efficient in solving dynamic problems with short time scales.

Our comparison of various approaches and mathematical models is particularly useful in connection with a complication of new unique codes and with problems of their testing for various physical scenarios. We believe such a comparison of various mathematical models and computer codes to be highly productive, because it (1) confirms the reliability of calculations with each of the codes; (2) verifies the applicability ranges of models (primarily of the approximate model); and (3) determines the efficiency of models. For example, the exact method at high densities and temperatures ($\rho > 10^9$ g cm^{-3}, $T_9 \geq 8$) requires more processor time, and, hence, it is more convenient to use the NSE model or the approximate scheme.

Good agreement with the calculations of other authors and reasonable computational time show that the developed model and the computer code are efficient tools for studying various types of nucleosynthesis, extreme (such as the r- and rp-processes) and, more importantly, any type of nucleosynthesis without restrictive assumptions characteristic of these limiting cases.

As for the physical results, our calculations indicate that the r-process must proceed under dynamic rather than static conditions. Only for a rapid change in con-

ditions and for the depletion of free neutrons (short hydrodynamic time scales) do the positions of the *r*-peak on the abundance curve agree excellently with observations for any *r*-process scenario.

ACKNOWLEDGMENTS

REFERENCES

1. S. I. Blinnikov and O. S. Bartunov, Astron. Astrophys. **273**, 106 (1993).

2. S. I. Blinnikov and N. V. Dunina-Barkovskaya, Mon. Not. R. Astron. Soc. **266**, 289 (1994).

3. S. I. Blinnikov and I. V. Panov, Pis'ma Astron. Zh. **22**, 45 (1996) [Astron. Lett. **22**, 39 (1996)].

4. S. I. Blinnikov, I. V. Panov, V. M. Chechetkin, and D. A. Ptitsyn, Pis'ma Astron. Zh. **21** (11), 872 (1995) [Astron. Lett. **21**, 786 (1995)].

5. S. I. Blinnikov, I. V. Panov, and M. A. Rudzkiĭ, Pis'ma Astron. Zh. **27** (2001) (in press) [Astron. Lett. **27** (2001) (in press)].

6. D. Bodansky, D. D. Clayton, and W. A. Fowler, Astrophys. J., Suppl. Ser. **16**, 299 (1968).

7. R. K. Brayton, F. G. Gustavson, and G. D. Hachtel, Proc. IEEE **60**, 98 (1972).

8. A. G. W. Cameron, J. J. Cowan, H. V. Klapdor, *et al.*, Astrophys. Space Sci. **91**, 221 (1983a).

9. A. G. W. Cameron, J. J. Cowan, and J. W. Truran, Astrophys. Space Sci. **91**, 235 (1983b).

10. J. J. Cowan, F.-K. Thielemann, and J. W. Truran, Phys. Rep. **208**, 267 (1991).

11. W. A. Fowler, G. R. Caughlan, and B. A. Zimmerman, Annu. Rev. Astron. Astrophys. **5**, 525 (1967).

12. C. Freiburghaus, S. Rosswog, and F.-K. Thielemann, Astrophys. J. Lett. **525**, L121 (1999).

13. C. Freiburghaus, J.-F. Rembges, T. Rausher, *et al.*, Astrophys. J. **516**, 381 (1999).

14. C. W. Gear, *Numerical Initial Value Problems in Ordinary Differential Equations* (Prentice-Hall, Englewood Cliffs, 1971).

15. E. R. Hilf, H. V. Groote, and K. Takahashi, Report CERN-76-13 (1976), p. 142.

16. W. Hillebrandt, Space Sci. Rev. **21**, 639 (1978).

17. W. R. Hix and F.-K. Thielemann, Astrophys. J. **511**, 862 (1999a).

18. W. R. Hix and F.-K. Thielemann, astro-ph/9906478 (1999b).

19. V. S. Imshennik and A. M. Khokhlov, Preprint No. 177, ITÉF (Institute of Theoretical and Experimental Physics, Moscow, 1983).

20. V. S. Imshennik, D. K. Nadezhin, and V. S. Pinaev, Astron. Zh. **44**, 768 (1967) [Sov. Astron. **11**, 617 (1967)].

21. V. S. Imshennik, S. S. Filippov, and A. M. Khokhlov, Pis'ma Astron. Zh. **7**, 219 (1981) [Sov. Astron. Lett. **7**, 121 (1981)].

22. J. Jänecke and B. P. Eynon, At. Data Nucl. Data Tables **17**, 467 (1976).

23. F. Käppeler, H. Beer, and K. Wisshak, Rep. Prog. Phys. **52**, 945 (1989).

24. K.-L. Kratz, J.-P. Bitouzet, F.-K. Thielemann, *et al.*, Astrophys. J. **403**, 216 (1993).

25. Yu. S. Lyutostanskiĭ, I. V. Panov, O. N. Sinyukova, *et al.*, Yad. Fiz. **44**, 66 (1986) [Sov. J. Nucl. Phys. **44**, 43 (1986)].

26. P. Möller and J. R. Nix, Nucl. Phys. A **536**, 20 (1992).

27. P. Möller, J. R. Nix, and K.-L. Kratz, At. Data Nucl. Data Tables **66**, 131 (1997).

28. D. K. Nadyozhin, I. V. Panov, and S. I. Blinnikov, Astron. Astrophys. **335**, 207 (1998).

29. I. V. Panov and D. K. Nadyozhin, Pis'ma Astron. Zh. **25**, 435 (1999) [Astron. Lett. **25**, 369 (1999)].

30. I. V. Panov, F.-K. Thielemann, and C. Freiburghaus, in *Proceedings of the International Conference on Nuclear Astrophysics*, Ed. by W. Hillebrandt and Ewald Müller (MPA, Tegernsee, 2000), p. 73.

31. S. Pissanetzky, *Sparse Matrix Technology* (Academic, London, 1984).

32. G. I. Pokrowski, Phys. Z. **32**, 374 (1931).

33. F. Rembges, C. Freiburghaus, T. Rausher, *et al.*, Astrophys. J. **484**, 412 (1997).

34. F.-K. Thielemann, M. Arnould, and J. W. Truran, in *Advances in Nuclear Astrophysics*, Ed. by E. Vangioni-Flam *et al.* (Editions Frontiéres, Gif-sur-Yvette, 1987), p. 525.

35. J. Witti, H.-Th. Janka, and K. Takahashi, Astron. Astrophys. **296**, 841 (1994).

36. S. E. Woosley and R. D. Hoffman, Astrophys. J. **395**, 202 (1992).

Translated by V. Astakhov

Photographic Observations of Comet Hale–Bopp at the Pulkovo Observatory: The Detection of Dust Envelopes

Yu. N. Gnedin*, A. A. Kiselev, T. P. Kiseleva, and K. L. Maslennikov

Pulkovo Observatory, Russian Academy of Sciences, Pulkovskoe shosse 65, St. Petersburg, 196140 Russia

Received July 19, 2000

Abstract—The photographic observations of comet Hale–Bopp with the 26-inch Pulkovo Observatory refractor in March–April, 1998, revealed three hemispherical gas–dust envelopes and one spiral jet in the comet head. We determined the angular distances of these envelopes from the comet nucleus and estimated their velocities. The masses and sizes of dust grains were estimated. We conclude that submicron-sized grains dominate in the envelopes. We also estimated the time scale of the comet nuclear activity, which manifests itself in dust ejection, the initial velocity of the ejected dust grains, and the ratio of the radiation-pressure force exerted on dust grains to the force of their gravitational attraction to the Sun. Our observations yielded an estimate for the radius of the comet nucleus, ~30 km. © *2001 MAIK "Nauka/Interperiodica".*

Key words: *comet Hale–Bopp: structure, activity, physical parameters*

1. INTRODUCTION

Our photographic observations of comet Hale–Bopp were carried out at Pulkovo Observatory with the 26-inch refractor from February 19 through April 8, 1997.

The original goal of our observing program was to determine accurate coordinates of the comet. However, our photographs clearly showed a spiral structure and hemispherical envelopes in the comet head that lay at different distances from the nucleus (or rather, from the comet photographic center) and changed with time. An analysis of these structures and a comparison of our results with those of other authors allowed us to determine several important physical parameters of the comet and to establish the pattern of their variations with time.

Before turning to a description of our specific results, we briefly consider the general characteristics of the comet Hale–Bopp phenomenon. It was included in the list of "Great Comets," the brightest comets that have appeared over the entire human history. About twenty comets have been honored with this name in the 19th and 20th centuries (Bortle 1997). Comet Hale–Bopp was not the brightest among them. The comets of March 1843, September 1882, and comet Ikeya-Secchi (C/1965 S1) were brighter. The distinctive features of comet Hale–Bopp were an unusually high brightness at a large heliocentric distance compared to other comets, an unusually high production rate of gas molecules Q (s^{-1}) and dust grains $M_{\rm d}$ (g s^{-1}), and its unusual activ-

ity. Thus, for example, when it was discovered on July 23, 1995, at a distance of 7.2 AU, its apparent magnitude was $m_V = 10\overset{m}{.}5$, whereas the magnitude of the famous comet Halley at the same distance was $m_V = 22\overset{m}{.}8$! The rate of production of virtually all gas molecules by the nucleus of comet Hale–Bopp was $Q = (10^{28}–10^{31})$ s^{-1} even at large heliocentric distances, $r_n > 3$ AU. The number of huge jets simultaneously ejected from the nucleus was commonly 6 to 8.

The figure shows the structure of the dust envelopes ejected from the nucleus.

2. OBSERVATIONS

A total of 20 photographs were taken for comet Hale–Bopp during our observations with the 26-inch Pulkovo Observatory refractor. The photographic plates were measured with the Ascorecord measuring machine. We measured the photometric center of the comet head and reference stars to determine the comet positions. In order to study the head structure, we measured three points on each of the three envelopes (two extreme points and one middle point), the head photometric center, and the comet second image obtained at the same diurnal circle after the telescope driving clock stopped. The latter was necessary for the photograph orientation in the equatorial coordinate system (to determine the position angles of the envelope central radii and the sunward direction).

A total of 36 comet positions were measured with an error of ±0.″35 (the rms error of a single comet position calculated relative to the ephemeris computed by Yu.D. Medvedev from the Institute of Theoretical

* E-mail address for contacts: gnedin@gao.spb.ru

Geometric-structure parameters for the head of comet Hale–Bopp

N pl	20496	20501	20511	20514	20517	20519	20531
Date UT, JD 24 505+	Mar. 4, 1997 $03^h\,47^m$ 11.6576	Mar. 5, 1997 $02^h\,35^m$ 12.6078	Mar. 10, 1997 $03^h\,24^m$ 17.6419	Mar. 11, 1997 $02^h\,36^m$ 18.6080	Mar. 25, 1997 $01^h\,59^m$ 32.5830	Apr. 2, 1997 $19^h\,46^m$ 41.3236	Apr. 8, 1997 $18^h\,38^m$ 47.2767
$R1$	6″9	7″5	9″3	10″9	21″8	12″9	6″9
$R2$	15″8	15″8	25″8	26″7	25″8	28″1	22″8
$R3$	27″9	29″7	38″6	39″6	40″6	44″0	35″6
$R12$	9″9	8″9	15″4	15″8	16″8	15″4	15″8
$R23$	11″9	13″9	13″9	12″9	17″4	16″0	12″9
$Q1$	150°	150°	137°	190°	135°	125°	120°
$Q2$	112°	115°	117°	115°	115°	108°	107°
$Q3$	93°	107°	90°	72°	74°	58°	64°
$P1$	181°	180°	217°	208°	195°	207°	201°
$P2$	201°	202°	217°	218°	216°	226°	217°
$P3$	201°	207°	232°	234°	243°	227°	224°
A	153°1	154°1	160°5	162°6	190°4	208°3	220°8

Astronomy) by using 20 plates taken over the observing period.

One of our first results was the detection of a displacement of the comet-head photometric center by 1″2 relative to the ephemeris in a direction away from the Sun, which apparently suggests a displacement of the brightness center from the nucleus.

Of the seven photographs currently studied in detail, the first five plates were taken during dawn hours at comet zenith distance $53° < Z_{HB} < 67°$ and at comet apparent distances from the Sun $44° < \rho_\odot < 46°$.

The last two plates were taken during dusk hours at zenith distances $62° < Z_{HB} < 68°$ and at distances from the Sun $40° < \rho_\odot < 42°$.

The table lists parameters that characterize the apparent geometric structure of the comet head. It gives the following data:

Npl—plate number;

Date—date and time (UT) of the observations (year, month, day, a fraction of a day);

$R1$, $R2$, $R3$—distances of the first, second, and third envelopes from the comet center (in arcseconds);

$R12$—separation between the first and second envelopes;

$R23$—separation between the second and third envelopes;

$Q1$, $Q2$, $Q3$—opening angles of the first, second, and third envelopes (in degrees);

$P1$, $P2$, $P3$—position angles of the envelope central radii (in degrees);

A—position angle of the sunward direction.

The envelopes are ~6″–8″ thick in the photographs. The diameter of the comet central nucleus varied between 4″ and 8″, depending on the comet total brightness.

3. RESULTS

3.1. First of all, our observational data allow us to estimate the apparent velocities of the envelopes relative to the photometric center. The mean velocity for the first envelope ($R1$) in the interval March 5–26, 1997, was $V_{R1} \approx 0″7$ day^{-1}. The velocity for the second envelope ($R2$) in the interval March 5–12, 1997, was $V_{R2} \approx 0″5$ day^{-1}. Finally, the corresponding estimate for the third envelope ($R3$) in the interval March 5–April 2, 1997, yields a similar velocity, $V_{R3} \approx 0″6$ day^{-1}.

If we associate the formation of the observed envelopes with an active process on the surface of the comet nucleus, then we can roughly estimate the characteristic period of the envelope activity due to rotation of the comet nucleus. To do this requires dividing the separation between the envelopes by the velocity of their apparent motion:

$$P_{\text{rot}} \approx \frac{R_{12}}{V_{R1}} \approx \frac{R_{23}}{V_{R2}} \approx 24^d \pm 1^d. \tag{1}$$

Curiously, this value agrees well with the so-called superperiod found by Jorda *et al.* (1997) using data on the molecular activity of comet Hale–Bopp. Recall that
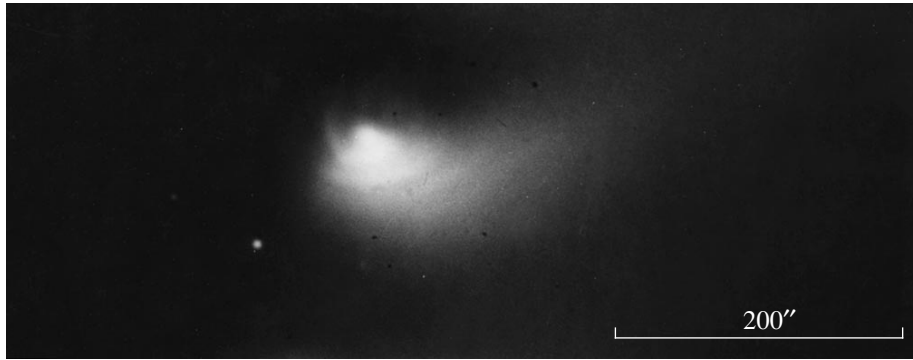
A photographic image of comet Hale–Bopp. The dust envelopes ejected from the nucleus are seen.

numerous observations, including those by Jorda *et al.* (1997), revealed a true rotation period of the comet nucleus $P_{rot}^{N} \approx 12\overset{h}{.}0$.

In March, the comet was at heliocentric distance $r = 1$ AU, which allows the characteristic true velocity of its envelopes to be estimated, $V \approx 5$ m s^{-1}. Curiously, our velocity estimates are comparable to the values that follow from the mechanism of electrostatic and rotational ejection of dust grains from disintegrating dust aggregates (Oberc 1997). In Fig. 1 from Oberc (1997), the velocity of electrostatic ejection of dust grains is plotted against their radii and masses (the grain density is assumed to be ~1 g cm^{-3}). Oberc's computations yield the radii and masses for grains with ejection velocities of several meters per second. As a result, it turns out that dust grain radii $\leq$~10^{-5} cm and masses $\leq$~10^{-15} g correspond to these velocities. It follows from this estimate that submicron-sized grains must dominate in the ejected envelopes. Curiously enough, the infrared spectrophotometric observations by Williams *et al.* (1997) in the wavelength range 1.20 to 18.5 μm on February 15 and 20, 1997, showed that the measured spectral energy distribution was satisfactorily explained by the scattering and thermal expansion of submicron-sized dust grains.

3.2. It is of interest to compare our data on the envelope radii for comet Hale–Bopp with the corresponding data for comet Halley obtained by the *Vega-2* spacecraft (Vaisberg *et al.* 1987; Table 4). The agreement between the envelope radii for the two comets is satisfactory. At the same time, direct *Vega-2* measurements of the grain masses yielded characteristic values of ~10^{-13} to -10^{-14} g (Vaisberg 1990).

3.3. A comparison of our observational data (Q) with the data of other authors allows the opening angles of the gas–dust envelopes to be compared. Approximately simultaneously with us (March 6), Licandro and Rudd (1997) observed diffuse arcs in the CN band and in the blue continuum. These two arcs can be compared with the two envelopes $R2$ and $R3$ that we observed. One diffuse arc was located north of the nucleus, and the other was to the east. The northern CN-band arc was

at a distance of 18″ from the nucleus with a 180° opening angle. The second, fainter arc, seen both in the CN band and in the continuum, had an opening angle of 90°. The opening angle of the dust envelope $R2$ that we observed was 115°, which roughly matches the opening angle of the diffuse gas envelope and slightly smaller than the opening angle of the first diffuse arc.

The circular shape of the gas–dust envelopes observed during the passage of comet Hale–Bopp through its perihelion is currently discussed in detail in the literature. Thus, for example, the numerical simulations by Samarasingha (2000) have shown that such an envelope structure stems from the fact that the dust and, apparently, gas jets are ejected from a fairly extended active region on the surface of the comet nucleus. Samarasingha (2000) estimates that the extent of the nuclear region generating the gas–jets can reach ~40°.

3.4 The most important result of our observations is the determination of v_0^2/β, an important physical parameter of comets, where v_0 is the initial grain velocity, and β is defined as the ratio of the radiation-pressure force exerted on a dust grain to the force of its gravitational attraction to the Sun. As a result, for a dust envelope whose motion is governed by the balance between the forces of radiation pressure and gravitational attraction to the Sun, as well as by the initial grain velocity v_0, the radius R_A is (see Grun and Jessberger 1990)

$$R_A = \frac{r_H^2}{2GM_\odot}\frac{v_0^2}{\beta}; \quad \beta = \frac{F_{rad}}{F_{grav}}, \qquad (2)$$

where r_H is the comet heliocentric distance, G is the gravitational constant, and $M_\odot$ is the solar mass. Hence, the estimate of v_0^2/β is

$$\frac{v_0^2}{\beta} = \frac{2GM_\odot R_A}{r_H^2} \approx 3 \times 10^5 \text{ m}^5/\text{s}^2. \qquad (3)$$

The radiation-pressure constant β is related to the radiation pressure η_{pr} introduced by Grun and Jessberger (1990) by

$$\beta = \frac{3F_\odot r_H^2}{4cGM_\odot \rho_d a}\eta_{pr} = \frac{5.78 \times 10^{-4}\ \text{kg/m}^2\ \eta_{pr}}{\rho_d a}, \quad (4)$$

where $F_\odot = 1370$ W m^{-2} is the energy flux from the Sun at distance $r_0 = 1$ AU; a and ρ_d are the grain radius and density, respectively. The efficiency coefficient η_{pr} depends markedly on grain properties and was numerically tabulated in several papers (Hellmich and Schwemm 1983; Burns *et al.* 1979; Crifo and Rodionov 1997). Assuming that $\beta \sim 1$ [submicron-sized grains; see, e.g., Grun and Jessberger (1990)], we obtain $v_0 \approx 5.5 \times 10^2$ m s^{-1} from Eq. (3) for the initial velocity of the dust grains that form the observed envelopes. On the other hand, the parameter β can be roughly estimated independently from the condition $\beta = g_{rad}/g_{grav}$, where $g_{grav} = 0.595$ cm s^{-2} is the gravitational acceleration. In turn, $g_{rad} = (v_0 - v)/t$, where $t \approx 8 \times 10^4$ s can be estimated from our observations: $g_{rad} \approx 0.7$ cm s^{-2} (if $v_0 = 5.5 \times 10^2$ m s^{-1}); hence $\beta \approx 1.1$.

3.5. The theory of cometary atmospheres allows the radius of the nucleus of comet Hale–Bopp to be estimated by using our observing data. The universally accepted theory by Probstein (1969) describes the dynamics of the gas–dust region near the nucleus, in which gas–dust envelopes and jets are formed. Having numerically solved the system of equations describing the behavior of the gas–dust mixture near the nucleus, Probstein derived a dependence of the initial grain velocity on two parameters: (1) χ, which determines the ratio of the rate of dust-grain production by the comet nucleus Q_d (s^{-1}) to the production rate of gas molecules Q_g; and (2) κ_d, which is a complex combination of the physical parameters of the nucleus itself and of the immediate circumnuclear region:

$$\kappa_d = 8a\rho_d \frac{(c_p T_0)^{1/2}}{3ZR_N}, \quad (5)$$

where c_p is the specific heat of the gas at constant pressure; T_0 is the temperature of the circumnuclear region, which is close to the surface temperature of the comet nucleus; R_N is the radius of the comet nucleus; and $Z = Q_g/4\pi R_N^2$. For comet Hale–Bopp, $Q_g \approx Q_{H_2O} = 5 \times 10^{30}$ s^{-1} (Weaver *et al.* 1997) and $T_0 = 300$ K (Williams *et al.* 1997). For the specific heat, we can take $c_p = 8 \times 10^2$ J kG^{-1} K^{-1} (Grun and Jessberger 1990). The parameter κ_d can be chosen based on the calculations by Probstein (1969) (see also Grun and Jessberger 1990) using the above initial grain velocity, $v_0 \approx 500$ m s^{-1}: $\kappa_d \approx 0.3$. On the other hand, based on the calculations by Crifo and Rodionov (1997), we can estimate the characteris-

tic size of the grains in the comet head from our initial velocity v_0: $a \approx 0.1$ μm. We then finally obtain

$$R_N = \frac{3Q_{H_2O}\kappa_d}{32\pi a\rho_d (c_p T_0)^{1/2}} \approx 30\ \text{km.} \quad (6)$$

Here, we took the universally accepted value $\rho_d \approx 1$ g cm^{-3} as the density of the cometary dust grains. Our estimate of the radius of the comet nucleus should be considered as an upper limit.

4. CONCLUSION

Comet Hale–Bopp was characterized by an extremely high activity, which manifested itself in the continuous generation of gas–dust envelopes, jets, and ejections by the comet nucleus. This activity was quasiperiodic in nature. We estimated the quasi-period to be 23–25 days; it was apparently associated with energy accumulation beneath the dust crust covering the comet nucleus and with rotation of the nucleus.

The ejected hemispherical envelopes consisted mainly of submicron-sized dust grains. This conclusion was independently reached by other researchers (see references to our paper).

Our observations allowed us to determine such an important parameter of cometary physics as v_0^2/β, where v_0 is the initial grain ejection velocity, and the parameter β is defined as the ratio of the radiation-pressure force exerted on a grain to the force of its gravitational attraction to the Sun.

Finally, based on our observational data, we estimated the radius of the nucleus of comet Hale–Bopp to be ~ 30 km.

REFERENCES

1. J. Bortle, Sky Telesc. **92**, 44 (1997).
2. J. A. Burns, P. L. Lamy, and S. Soter, Icarus **40**, 1 (1979).
3. J. F. Crifo and A. V. Rodionov, Icarus **127**, 319 (1997).
4. E. Grun and E. K. Jessberger, in *Physics and Chemistry of Comets*, Ed. by W. F. Huebner (Springer-Verlag, New York, 1990), p. 113.
5. R. Hellmich and G. H. Schwemm, in *Cometary Exploration,* Ed. by T. I. Gombosi (Central Research Institute for Physics, Hungarian Academy of Science, Budapest, 1983), p. 175.
6. L. Jorda, J. Lecacheux, and F. Colas, IAU Circ., No. 6583 (1997).

7. J. Licandro and P. Rudd, IAU Circ., No. 6583 (1997).

8. P. Oberc, Planet. Space Sci. **45** (2), 221 (1997).

9. R. F. Probstein, in *Problems of Hydrodynamics and Continuum Mechanics*, Ed. by M. A. Lavrent'ev (Society for Industrial and Applied Mathematics, Philadelphia, 1969), p. 568.

10. N. H. Samarasingha, Astrophys. J. Lett. **529**, L107 (2000).

11. O. L. Vaisberg, in *Comet Halley: Investigations, Results, Interpretations,* Ed. by J. Mason, E. Horwood, New York, 1990), Vol. 2, p. 33.

12. O. L. Vaisberg, V. Smirnov, A. Omel'chenko, *et al.*, Astron. Astrophys. **187**, 753 (1987).

13. H. A. Weaver, P. D. Feldman, M. F. A'Hearn, *et al.*, Science **275**, 1900 (1997).

14. D. M. Williams, C. G. Mason, R. D. Gehrz, *et al.*, Astrophys. J. Lett. **489**, L91 (1997).

Translated by N. Samus'

Generation of Resonance Transition Emissions in the Solar Atmosphere

G. D. Fleĭshman*

Ioffe Physicotechnical Institute, Russian Academy of Sciences, ul. Politekhnicheskaya 26, St. Petersburg, 194021 Russia
Received August 16, 2000

Abstract—We derive formulas for the radio flux generated in solar flares by the resonance transition mechanism. This mechanism is shown to produce the observed decimeter-wave emission in continuum radio bursts at a level of small-scale irregularities of $\sim 10^{-6}$–10^{-7}. Thus, an analysis of continuum decimeter emission offers a unique opportunity to study small-scale turbulence in solar flares. © *2001 MAIK "Nauka/Interperiodica"*.

Key words: *solar flares, small-scale turbulence, plasma diagnostics*

INTRODUCTION

The various types of solar radio emissions result both from a difference in the physical conditions in the source and from a difference in the microscopic mechanisms of electromagnetic radiation that dominate in particular events (Bastian *et al.* 1998). The important role of the bremsstrahlung, magnetobremsstrahlung (including maser), and plasma emission mechanisms for the solar corona is considered to have been firmly established (Bastian *et al.* 1998; Fleĭshman and Mel'nikov 1998). The role of the transition emission (TE) of fast particles in plasma with random density irregularities has been studied to a considerably lesser extent. Until now, the probable TE contribution has been estimated using formulas derived in the ultrarelativistic limit, which are valid for frequencies above the local plasma frequency (Fleĭshman and Kahler 1992). However, the bulk of the energy emitted by the transition mechanism is concentrated in the peak near the plasma frequency (Platonov and Fleĭshman 1994). The intensity of this peak (resonance transition emission, RTE) is very high and depends both on the level of plasma density irregularities and on the external magnetic field strength (Platonov and Fleĭshman 1995).

The plasma frequencies in the solar atmosphere lie in the range of radio waves observable by ordinary ground-based radio telescopes. These two facts (the high emission intensity and the accessible electromagnetic range) make the application of RTE to an analysis of the solar radio emission of current interest and promising. For comparison, note that in the interstellar medium, the transition emission dominates at frequencies $f < 100$ kHz (Fleĭshman and Tokarev 1995); observations at these frequencies are not easy to perform.

Here, we derive formulas for RTE in a form convenient for use in solar radio astronomy, give examples of their use, and make the corresponding estimates.

BASIC FORMULAS AND MODELS

Fleĭshman and Kahler (1992) showed that the contribution of transition emission could dominate in continuum bursts of decimeter and microwave solar radio emission if the magnetic field in the source is not too strong,

$$\omega_B = 2\pi f_B \ll \omega_p = 2\pi f_p, \qquad (1)$$

where ω_B and ω_p are the electron gyro- and plasma frequencies, respectively. In this case, the bulk of the emission is generated by the gyrosynchrotron mechanism at sufficiently high frequencies,

$$f \gtrsim f_{\text{R–Ts}} \approx f_p^2/f_B, \qquad (2)$$

where $f_{\text{R–Ts}}$ is the Razin–Tsytovich frequency. At frequencies

$$f_p < f \lesssim f_{\text{R–Ts}}, \qquad (3)$$

when the synchrotron emission (and absorption) is exponentially low, an increase of the emission intensity with decreasing frequency attributable to the contribution of the transition emission of fast particles on plasma density irregularities of the source can be observed.

This general conclusion is equally valid for ordinary and resonance transition emissions. However, the RTE spectrum from a homogeneous (on the average) source represents a narrow peak, which should be averaged with the distribution function describing the actual regular nonuniformity of the emission source.

For definiteness, we assume that the distribution of the TE source "in plasma frequency" can be described in some range of plasma frequencies by the power law

$$F(\omega_p) = (\lambda - 1)\frac{\omega_{p0}^{\lambda - 1}}{\omega_p^{\lambda}}, \quad \omega_p > \omega_{p0}, \qquad (4)$$

where ω_{p0} is the lowest plasma frequency in the source.

In addition, we assume that the distribution of fast electrons and the spectrum of plasma density irregularities are described in their own power laws

$$dN_e = (\xi - 1)N_e(x > x_0)\frac{x_0^{\xi - 1}dx}{x^{\xi}}, \qquad (5)$$

$$x_0 < x < x_1,$$

where $x = p/mc$ is the dimensionless particle momentum, $N_e(x > x_0)$ is the number density of fast electrons

$$|\delta N|_k^2 = \frac{\nu - 1}{4\pi}k_0^{\nu - 1}\langle \Delta N^2 \rangle k^{\nu + 2}, \qquad (6)$$

where $k_0 = 2\pi/l_0$, l_0 is the largest (normalization) scale of the plasma density irregularities, and $\langle \Delta N^2 \rangle$ is the mean square of the density irregularities on scales $l \le l_0$.

Depending on the type of an electromagnetic wave (ordinary or extraordinary) on the relationship between dimensionless parameters ω_B/ω_p and v_T/c (where v_T is the thermal velocity of the plasma electrons, c is the speed of light), and on the spectral indices ξ and ν, the RTE intensity is described by eight different formulas (Platonov and Fleĭshman 1995). Given that the RTE peak is narrow, the RTE spectral density for a homogeneous medium can be represented in each of these cases as

$$I_\omega^{(i)} = P^{(i)}\delta(\omega - \omega_p), \quad 1 \le i \le 8. \qquad (7)$$

To determine the flux generated by the transition mechanism in an inhomogeneous source in the solar atmosphere, we should integrated the intensity (7) with the distribution function (4) over the source volume and take into account the distance from it to the observer:

$$F_f = \frac{2\pi V}{R_s^2}\int F(\omega_p)P^{(i)}\delta(\omega - \omega_p)d\omega_p, \qquad (8)$$

where V is the volume of the emission source, and R_s is the distance from the Sun to the Earth.

In the sources of solar decimeter and centimeter radio bursts, the following relations generally holds:

$$v_T/c < \omega_B/\omega_p < (v_T/c)^{1/2}. \qquad (9)$$

If $\xi < \nu + 2$, the RTE of ordinary waves is described by formula P_5 (Platonov and Fleĭshman 1995); if $\xi > \nu + 2.5$, it is described by formula P_3; and if $\nu + 2 < \xi < \nu + 2.5$, it is described by their sum. Let us consider in more detail the case where the RTE is described by relation P_5:

$$P_5 = \frac{\pi^2(\nu - 1)(\xi - 1)\Gamma\left(\frac{\xi - 1}{2}\right)\Gamma\left(\frac{\nu - \xi + 2.5}{2}\right)}{9 \times 6^{1/2}(\nu + 2)\Gamma\left(\frac{\nu}{2} + \frac{3}{4}\right)}$$

$$\times (1 + \cos^2\theta)\frac{e^6\langle\Delta N^2\rangle k_0^{\nu - 1}}{m^2c^3}x_0^{\xi - 1}N_e\left(\frac{c}{\omega_p}\right)^{\nu + 1}$$

$$\times \left(\frac{\omega_p}{\omega_B}\right)^{1/2}\frac{c}{v_T}, \qquad (10)$$

where $\Gamma(z)$ is the Euler gamma function; θ is the angle between the line of sight and the magnetic-field direction in the source; and e and m are the electron charge and mass, respectively. Substituting Eq. (10) in Eq. (8) yields

$$F_f = \frac{V}{R_s^2}C_5\frac{e^2}{c}(1 + \cos^2\theta)\int f_p x_0^{\xi - 1}N_e\frac{\langle\Delta N^2\rangle}{N^2}$$

$$\times \left(\frac{k_0c}{\omega_p}\right)^{\nu - 1}\left(\frac{\omega_p}{\omega_B}\right)^{1/2}\frac{c}{v_T}\left(\frac{\omega_{p0}}{\omega_p}\right)^{\lambda}\delta(\omega - \omega_p)d\omega_p, \qquad (11)$$

where

$$C_5$$

$$= \frac{\pi^2(\lambda - 1)(\nu - 1)(\xi - 1)\Gamma\left(\frac{\xi - 1}{2}\right)\Gamma\left(\frac{\nu - \xi + 2.5}{2}\right)}{36 \times 6^{1/2}(\nu + 2)\Gamma\left(\frac{\nu}{2} + \frac{3}{4}\right)}. \qquad (12)$$

We emphasize that the result of integration (11) is determined by whether (and how) the parameters in Eq. (11), $\langle\Delta N^2\rangle$, k_0, ω_B, depend on plasma frequency ω_p. If we restrict our analysis to the case where the dependence of any of the parameters on plasma frequency can be fitted by a power-law function, then the result of integration (11) can be represented in general form as

$$F_f = C_5\frac{e^2 f_{p0}}{R_s^2 c}(1 + \cos^2\theta)x_0^{\xi - 1}(VN_e)$$

$$\times \frac{\langle\Delta N^2\rangle}{N^2}\left(\frac{k_0c}{\omega_{p0}}\right)^{\nu - 1}\left(\frac{\omega_{p0}}{\omega_B}\right)^{1/2}\frac{c}{v_T}\left(\frac{\omega_{p0}}{\omega}\right)^{\alpha}. \qquad (13)$$

The spectral index α is determined by the dependence of the quantities in Eq. (11) on local plasma frequency. For example, if

$$\frac{\langle\Delta N^2\rangle}{N^2} = \text{const}, \quad \frac{k_0c}{\omega_p} = \text{const}, \quad \frac{\omega_p}{\omega_B} = \text{const}, \qquad (14)$$

then

$$\alpha = \lambda - 1; \qquad (15)$$

if

$$\frac{\langle \Delta N^2 \rangle}{N^2} = \text{const}, \quad k_0 = \text{const}(\omega_p),$$

$$\omega_B = \text{const}(\omega_p), \tag{16}$$

then

$$\alpha = \lambda + \nu - 2.5 \tag{17}$$

and so on. For brevity, we omit subscript 0 on ω_{p0} and use the quantity ω_p in the subsequent formulas. Substituting the well-known fundamental constants and the distance from the Sun to the Earth $R_s = 1.49 \times 10^{13}$ cm in Eq. (13), we express the RTE flux from an inhomogeneous source in solar flux units (1 sfu = $10^{-19} \frac{\text{erg}}{\text{cm}^2 \text{ s Hz}}$):

$$F_f^{(5)} = 3.45 \times 10^5 C_5 (1 + \cos^2\theta) \frac{f_p}{1 \text{ GHz}} x_0^{\xi - 1}$$

$$\times \frac{(VN_e)}{10^{33}} \left(\frac{k_0 c}{\omega_p}\right)^{\nu - 1} \frac{\langle \Delta N^2 \rangle}{N^2} \left(\frac{\omega_p}{\omega_B}\right)^{1/2} \frac{c}{v_T} \left(\frac{\omega_p}{\omega}\right)^\alpha \text{ sfu.} \tag{18}$$

Recall that formula (18) is valid [under the condition (9)] for sufficiently hard spectra of fast electrons, $\xi < \nu + 2$. For soft particle spectra, $\xi > \nu + 2.5$, using the RTE intensity P_3 (Platonov and Fleĭshman 1995) yields for an ordinary wave:

$$F_f^{(3)} = 3.45 \times 10^5 C_3 \frac{f_p}{1 \text{ GHz}} x_0^{\xi - 1} \frac{(VN_e)}{10^{33}} \left(\frac{k_0 c}{\omega_p}\right)^{\nu - 1}$$

$$\times \frac{\langle \Delta N^2 \rangle}{N^2} \frac{c^2}{v_T^2} \left[\frac{\omega_p}{\omega_B} \left(\frac{6 \times 3^{1/2} v_T^3}{c^3}\right)^{1/2}\right]^{\nu + 3 - \xi} \left(\frac{\omega_p}{\omega}\right)^\alpha \text{ sfu,} \tag{19}$$

where

$$C_3 = \frac{\pi(\lambda - 1)(\nu - 1)(\xi - 1)}{12(\nu + 2)}$$

$$\times \left[\frac{8}{15(\nu + 3 - \xi)} + \frac{\pi(1 + \cos^2\theta)}{8(\xi - \nu - 2)}\right]. \tag{20}$$

In the intermediate case $\nu + 2 < \xi < \nu + 2.5$, the emission is described by the sum of Eq. (18) and Eq. (19).

The preferential RTE polarization corresponds to an ordinary wave (Platonov and Fleĭshman 1995). Nevertheless, the degree of polarization under the condition (9) is generally not high. Therefore, to estimate the RTE intensity (in the two modes), the doubled values of (18) and/or (19) can be used.

Note that even softer spectra of fast electrons,

$$\xi > \nu + 3, \tag{21}$$

commonly take place in solar flares. Indeed, the hard X-ray spectra of solar flares are generally

$$F_E \propto E^{-\gamma}, \quad 3 < \gamma < 7. \tag{22}$$

The corresponding energy spectra of fast nonrelativistic electrons are also the power laws

$$N(E) \propto E^{-\xi_E}, \quad 2.5 < \gamma < 8. \tag{23}$$

In the nonrelativistic range, the spectral index in the momentum distribution (5) ξ is related to ξ_E by

$$\xi = 2\xi_E - 1, \tag{24}$$

i.e., $\xi > 5$, and formula (21) is valid for a Kolmogorov irregularity spectrum.

In this case, the transition emission for each of the normal modes is described by P_2 (Platonov and Fleĭshman 1995). For the total emission (in both modes), which is not polarized in this case, we find, similar to Eqs. (18), (19), that

$$F_f^{(2)} = 3.45 \times 10^5 C_2 \frac{f_p}{1 \text{ GHz}} \left(\frac{k_0 c}{\omega_p}\right)^{\nu - 1}$$

$$\times \frac{\langle \Delta N^2 \rangle}{N^2} x_0^{\nu + 2} \frac{VN_e(>x_0)}{10^{33}} \frac{c^2}{v_T^2} \left(\frac{f_p}{f}\right)^\alpha \text{ sfu,} \tag{25}$$

where

$$C_2 = \frac{4\pi(\lambda - 1)(\nu - 1)(\xi - 1)}{45(\nu + 2)(\xi - \nu - 3)}. \tag{26}$$

ESTIMATING THE CONTRIBUTION OF RTE IN SOLAR RADIO BURSTS

As was discussed above, the intensity of transition emission is particularly high near the local plasma frequency. It should be borne in mind that the plasma mechanism of radio emission, which is based on the instability of plasma waves and on their subsequent conversion to radio waves, can effectively operate at the same frequencies. For this instability to take place, the distributions of fast particles must be anisotropic (of a cone or beam type). The transition emission mechanism dominates (near the plasma frequency) when the distributions of emitting fast electrons are sufficiently isotropic and when the conditions of plasma instability are not satisfied. Such a situation apparently occurs in continuum decimeter and microwave bursts of solar radio emission. In this case, the high-frequency part of the burst is undoubtedly associated with the gyrosynchrotron emission of energetic electrons (Bastian *et al.* 1998), while its low-frequency part can be generated by the transition mechanism.

Let us estimate the parameters in the sources of solar radio bursts. We assume that

$$\lambda = \nu = 1.5, \quad \xi = 3.5, \tag{27}$$

$$f_p = 1 \text{ GHz}, \quad VN_e(>1 \text{ MeV}) = 10^{32},$$

$$\left(\frac{\omega_p}{\omega_B}\right)^{1/2} \frac{c}{v_T} = 10^2, \tag{28}$$

$$k_0 = \omega_p/c, \quad \cos^2\theta \approx 0.5. \tag{29}$$

The RTE flux calculated using Eq. (18) is then

$$F_f = 3 \times 10^6 \frac{\langle \Delta N^2 \rangle}{N^2}\left(\frac{f_p}{f}\right)^\alpha \text{ sfu}. \tag{30}$$

This means that to provide a TE intensity of 100 sfu near 1 GHz requires [for the assumed parameters (27)–(29)] the presence of plasma density irregularities at the level

$$\frac{\langle \Delta N^2 \rangle}{N^2} = 3 \times 10^{-5} \tag{31}$$

on scales $l < l_0 = 2\pi c/\omega_p$ (for f_p = 1 GHz, l_0 = 30 cm).

For steeper (softer) spectra of fast electrons, the RTE intensity is given by formula (19). If we assume that

$$\lambda = 2, \quad \nu = 1.7, \quad \xi = 4.5, \tag{32}$$

then, for the same parameters (28), (29), (31), we find from Eq. (19) that

$$F_f \approx 5000 \text{ sfu}. \tag{33}$$

The corresponding flux exceeds (30) by more than an order of magnitude; i.e., at the irregularity level (31), the radio flux may exceed 1000 sfu.

The RTE flux depends on a number of parameters, which must seemingly result in a large uncertainty of the results. However, when diagnosing the parameters of a continuum burst source in detail, basic information (about the number of fast electrons, their spectrum, the magnetic-field strength, etc.) is extracted from the gyrosynchrotron part of the spectrum and from an analysis of the accompanying hard X-ray and gamma-ray emissions. An analysis of the soft X-ray and/or millimeter-wave emission allows the temperature and density of the medium to be estimated.

Thus, many of the parameters (ω_p, ω_B, v_T, VN_e, ξ) can be estimated from independent observations, after which only the irregularity level $\dfrac{\langle \Delta N^2 \rangle}{N^2}$ and the spectral indices λ, ν, α remain unknown. The value of α can be inferred from the slope of the low-frequency part of the spectrum (which is related to the transition emission). Unfortunately, there is no unambiguous relationship between α, on the one hand, and ν and λ, on the other; as a result, their values cannot be unequivocally inferred. Nevertheless, ν and λ are numbers of the order of unity, so the lack of knowledge of their exact values does not result in any considerable uncertainty in the level of small-scale density irregularities $\dfrac{\langle \Delta N^2 \rangle}{N^2}$ estimated from the radio flux in the low-frequency part of the spectrum.
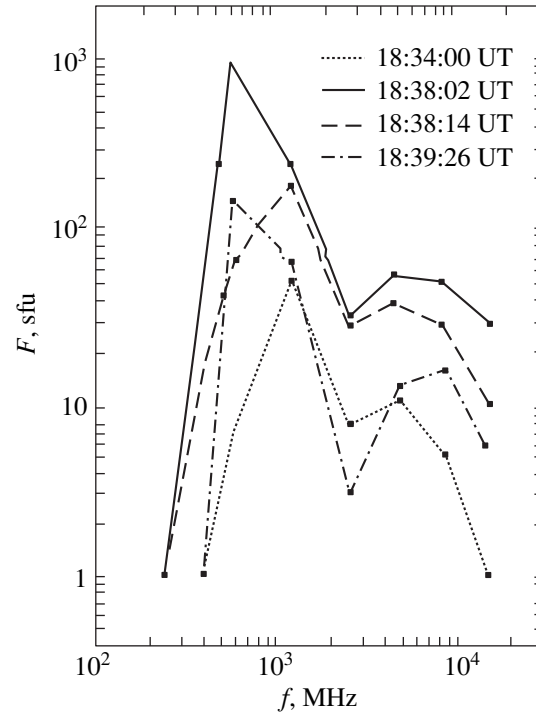
Radio spectra for the solar flare of December 24, 1991, at consecutive times.

As an example, let us consider the radio burst detected on December 24, 1991 (Willson 1993), whose continuum decimeter-wave emission was generated by the transition mechanism. Radio spectra of this burst at various times are shown in the figure. Apart from the above spectra, there are also observational data on the time profiles and spectra of hard X-ray emission, data on soft X-ray emission, the time profiles of radio emission at frequencies of 410, 606, 1415, 2695, 4880, 8800, and 15 400 MHz, as well as images of the radio source at 333 and 1446 MHz.

In the region of the peak radio emission, the instantaneous number of emitting electrons $VN(>10 \text{ keV})$ can be found from hard X-ray data:

$$VN_e(>10 \text{ keV}) \approx 10^{38}, \tag{34}$$

the X-ray spectral index γ is 4. The corresponding indices of the energy and momentum distributions for the nonrelativistic electrons captured in a radio source are (Melnikov and Magun 1998; Melnikov and Silva 1999)

$$\xi_E = 3.5, \quad \xi = 6. \tag{35}$$

The temperature of the plasma emitting the observed soft X rays is

$$T \sim 7 \times 10^6 \text{ K} \quad (v_T \approx 10^9 \text{ cm/s}). \tag{36}$$

Assuming that the microwave emission of a flare is generated by the gyrosynchrotron mechanism, we can obtain

$$f_p \approx 6 \times 10^8 \text{ Hz} \quad (N \approx 4 \times 10^9 \text{ cm}^{-3}),$$
$$f_B \approx 8 \times 10^7 \text{ Hz} \quad (B \approx 30 \text{ G}). \tag{37}$$

The high-frequency ($f = 8.8$–15.4 GHz) spectral index at the emission peak is

$$\alpha_2 \approx 0.9 \tag{38}$$

and subsequently increases to 1.75. The microwave flux, the spectrum shape, and the time-profile structure are in excellent agreement with the assumption that the hard X-ray and microwave emissions are generated by the same fast electrons, with the latter being generated by the gyrosynchrotron mechanism.

The time profiles of the decimeter radio emission show a surprising similarity to the profiles of the hard X-ray and microwave emissions. Consequently, the decimeter emission must also be generated by the same fast electrons as the microwave and hard X-ray emissions. However, as was shown in detail by Wilson (1993), the gyrosynchrotron mechanism cannot account for the shape of the decimeter-band spectrum. Note that the low-frequency spectral index ($f = 1415$–2695 MHz)

$$\alpha_1 \approx 3 \tag{39}$$

is appreciably larger than the high-frequency α_2 (38). Wilson (1993) assumed that the decimeter emission could be generated by the plasma mechanism. In this case, however, one would expect a much richer fine temporal structure than actually observed.

The decimeter emission can be explained most naturally by the resonance transition mechanism. Let us suppose that the dimensionless quantities (14) do not depend on plasma frequency. The spectral index in the distribution (4) is then

$$\lambda = \alpha_1 + 1 \approx 4. \tag{40}$$

Assume that the spectrum of density irregularities is described by the Kolmogorov law, i.e.,

$$\nu = 1.7. \tag{41}$$

Then, using (34)–(37), (40), (41), $C_2 = 0.15$, $x_0 (10 \text{ keV}) = 0.2$, we obtain the RTE flux (25) near $f_p \approx 600$ MHz

$$F_f = 0.7 \times 10^{10} \frac{\langle \Delta N^2 \rangle}{N^2} \text{ sfu}, \tag{42}$$

where $\langle \Delta N^2 \rangle$ refers to scales $l < c/f_p = 50$ cm, so $k_0 c/\omega_p = 1$.

From the observed flux at $f = 606$ MHz

$$F_{606} = 1300 \text{ sfu} \tag{43}$$

we find that

$$\frac{\langle \Delta N^2 \rangle}{N^2} \approx 2 \times 10^{-7}. \tag{44}$$

Thus, the very low level of plasma density irregularities (44) provides the observed decimeter radio emission of the December 24, 1991 flare. The sharp cutoff of the emission at $f < 600$ MHz is clearly associated with the deviation of the actual plasma-frequency distribution function of the source from Eq. (4) at $f_p < 600$ MHz.

It should be particularly emphasized that there are presently no other methods (except for the mechanism of resonance transition emission proposed here) for investigating the level of such small-scale irregularities in the solar atmosphere. Curiously, in the flare considered, the (dimensionless) level of small-scale density irregularities (44) is the same as that in the interstellar medium (in which it is determined by analyzing scintillations of radio sources (Cordes *et al.* 1991).

CONCLUSION

Here, we have transformed the general formulas of resonance transition emission in randomly inhomogeneous magnetoactive plasma (Platonov and Fleĭshman 1995) to a form convenient for the application to an analysis of continuum solar radio bursts.

Our estimates show that even low levels of small-scale plasma-density irregularities can result in intense radio emission in the low-frequency part of a continuum radio burst due to the high efficiency of the resonance transition mechanism.

The method described here offers a unique opportunity to study extremely small-scale turbulence in the solar atmosphere, because it is sensitive to very low irregularity levels of the medium

$$\frac{\langle \Delta N^2 \rangle}{N^2} > 10^{-6} - 10^{-7} \tag{45}$$

on very smallest scales

$$l < 100 \text{ cm}. \tag{46}$$

At present, there are no other methods (either direct or indirect) for investigating such irregularities.

REFERENCES

1. T. S. Bastian, A. O. Benz, and D. E. Gary, Annu. Rev. Astron. Astrophys. **36**, 131 (1998).
2. J. M. Cordes, J. M. Weisberg, D. A. Frail, *et al.*, Nature **354**, 121 (1991).

3. G. D. Fleĭshman and S. W. Kahler, Astrophys. J. **394**, 688 (1992).

4. G. D. Fleĭshman and V. F. Mel'nikov, Usp. Fiz. Nauk **168**, 1265 (1998) [Phys. Usp. **41**, 1157 (1998)].

5. G. D. Fleĭshman and Yu. V. Tokarev, Astron. Astrophys. **293**, 565 (1995).

6. V. F. Melnikov and A. Magun, Sol. Phys. **178**, 591 (1998).

7. V. F. Melnikov and A. V. Silva, in *Proceedings of the 9th Solar Meeting on Solar Physics "Magnetic Fields and Solar Processes,"* Ed. by A. Wilson (ESA, Florence, 1999), ESA SP-448, Vol. 2, p. 1053.

8. K. Yu. Platonov and G. D. Fleĭshman, Zh. Éksp. Teor. Fiz. **106**, 1053 (1994) [JETP **79**, 572 (1994)].

9. K. Yu. Platonov and G. D. Fleĭshman, Zh. Éksp. Teor. Fiz. **108**, 1942 (1995) [JETP **81**, 1059 (1995)].

10. R. A. Willson, Astrophys. J. **413**, 798 (1993).

Translated by G. Rudnitskiĭ

Does the Solar Magnetic Field Increase?

V. A. Kotov[1]* and I. V. Kotova[2]

[1] *Crimean Astrophysical Observatory, p/o Nauchnyĭ, Crimea, 334413 Ukraine*
[2] *Moscow State University, Vorob'evy gory, Moscow, 119899 Russia*
Received April 12, 2000

Abstract—We consider measurements of the general magnetic field (GMF) of the Sun as a star at four world observatories from 1968 until 1999. We show that, within the error limits, the mean strength of the photospheric magnetic field H (of its longitudinal component, in magnitude) has not changed over the last 32 years. This is in conflict with the recent conclusion by Lockwood *et al.* (1999) that the solar coronal magnetic field increased by 40% from 1964 until 1996 and has almost doubled in the last 100 years. The causes of discrepancies in the results are discussed. At the same time, the GMF exhibits a natural 11-year variation associated with the solar cycle. The strength of the photospheric longitudinal magnetic field (in absolute value) averaged over 32 years is 0.46 G (at an rms GMF strength of 0.57 G). The mean GMF for all years of measurements had a south polarity: $\overline{H} = -0.030 \pm 0.018$ G. The difference from zero is statistically significant at 1.7σ (90%) and may be directly related to the outstanding problem of the solar magnetic "monopole." © *2001 MAIK "Nauka/Interperiodica"*.

Key words: *Sun*

1. INTRODUCTION

The magnetic field is largely responsible for the Sun's variability and its 11-year cycle. It appears to be also closely correlated with luminosity variations, although the mechanism of this correlation is not yet clear. Measurements with extra-atmospheric radiometers (specifically, with ACRIM) indicate that the solar irradiance actually varies with a quasi-period of 11 years and a relative amplitude of about 0.1%. In addition, and this is most important in the context of our work, the solar irradiance apparently has a secular trend: it increases approximately by 0.036% in a decade (Willson 1997). Theoretical calculations of atmospheric circulation models show that a global change in the Earth's temperature by 1 K can occur when the solar irradiance changes by a mere 1% (Willson 1997; and references therein.) According to the estimate by Willson (1997), a change in irradiance can cause a global warming by 0.4 K in the next 100 years, which, ignoring the greenhouse (industrial) effect, can have substantial climatic impacts on our planet.

It is natural to associate the secular change in solar irradiance, for example, with a potential change in the solar general magnetic field (GMF), especially since the magnetic field, while extending from the photosphere into the interplanetary medium and then being involved in reconnection in circumterrestrial space, can effectively take part in energy transfer from the Sun to the Earth. Therefore, this field can also affect appreciably the Earth's climate, specifically, the state of cloudiness (Lockwood *et al.* 1999). However, the interplanetary magnetic field (IMF) is known to correlate with background (or large-scale) photospheric fields and, consequently, with the mean magnetic flux from the visible solar hemisphere rather than with sunspots and active regions (Severny 1969; Scherrer 1973; Kotov *et al.* 1998a; Kotov and Stepanyan 1980; Grigoryev and Demidov 1987).

It is difficult to measure the mean magnetic field of the visible solar disk, because its value (H) rarely exceeds 1 G. In the 1960s, Bumba *et al.* (1967) attempted to average synoptic magnetic maps of the Sun in order to determine H, but they failed to obtain any significant result, in particular, a dependence of the mean field on the phase of 27-day solar rotation. The cause of this failure was an excessively high threshold of the magnetograms (6 G). Now, background fields with a mean (effective) longitudinal strength in the photosphere of about 2 G (Scherrer 1973; Kotov and Stepanyan 1980) are known to be the main source of the magnetic field H that determines the mean magnetic flux from the Sun.

Severny (1969) proposed a new, more efficient, and simple method for measuring the GMF by observing the Sun in a "parallel" beam, when the spectrograph slit is illuminated by light from the entire visible solar disk; i.e., the Sun is observed as a star. In this case, the magnetic field H is recorded by a solar magnetograph using the Zeeman effect in a photospheric absorption line (as a rule, in the Fe I $\lambda 525.0$ nm line with a Lande factor $g = 3$).

Subsequently, the GMF has been measured more or less regularly at four observatories: Crimean Astrophysical Observatory (CrAO), Wilcox Solar Observatory (WSO) of the Stanford University, Sayany Solar Observatory (SSO) of the Institute for Solar–Terrestrial Physics (Irkutsk), and Mount Wilson Observatory (MWO). These measurements have been continuing up until now at the first three observatories. A total of about 12 000 GMF measurements were made over 32 years (according to the CrAO data and the published data of other observatories, see Section 2), each representing the H value measured with a particular magnetometer during a given UT day. The measurement error is typically 0.05–0.15 G. For more details on the instruments, the method of measurements, and the observational data themselves, see Scherrer (1973), Kotov *et al.* (1998a), and Grigoryev and Demidov (1987).

Recently, having analyzed variations of the IMF radial component at the Earth's orbit from 1964 until 1996, Lockwood *et al.* (1999) concluded that the solar coronal magnetic field increased approximately by 40% in 32 years and almost doubled in the last 100 years. The conclusion was confirmed by the behavior of geomagnetic activity index *aa* in the 20th century. Since the coronal field is largely determined by large-scale photospheric fields (especially by the field of coronal holes), this conclusion can have serious implications for the dynamo mechanism and theories explaining solar cyclic activity, including in the context of the Sun's secular variability. This can also be of considerable importance for geophysical phenomena and for climatic impacts on the Earth, for example, global atmospheric processes on a sufficiently long time scale [see Willson (1997) and Lockwood *et al.* (1999) for references].

We consider the behavior of the GMF of the Sun as a star in an effort to independently verify the surprising result of Lockwood *et al.* (1999). The data were obtained over the last 32 years at different world observatories from direct measurements of the mean photospheric magnetic field.

2. 1968–1999 MEASUREMENTS OF THE SOLAR GMF

All published GMF measurements are listed in the table. We supplemented the data set with new, as yet unpublished measurements in 1998–1999, bringing the total number of CrAO measurements to $N = 1707$. Apart from normalization factors k (see below), we introduced no correction factors associated, for example, with calibration, the instrument, solar limb darkening, and magnetograph signal saturation in the photosphere (in thin magnetic flux tubes with strong magnetic fields). These normalization factors were determined separately for the data of each observatory in order to combine them into a single time sequence 1968–1999.

To obtain the combined GMF series, we used a simple, but apparently reliable procedure. First, we calculated the rms values Δ for each of the four magnetographs (see the table) and determined their mean $\langle\Delta\rangle = 0.630$ G. Subsequently, the H values from the four data sets were reduced to $\langle\Delta\rangle$ by multiplying the data from each of the four sets by the factors $k = \langle\Delta\rangle/\Delta$, which are given in the next-to-last column of the table. Finally, the calculated normalized values of H for the four observatories were reduced to a single time sequence (1968–1999) with the total number of measurements $N = 11\,878$ and $\Delta = 0.630$ G.

We do not provide the GMF power spectrum, because it has been extensively studied in recent years (see, e.g., Kotov *et al.* 1998a, 1998b, 1999; Rivin and Obridko 1992; Khaneĭchuk 1999; Ponyavin 1998) in connection with solar rotation, annual GMF variations (of an unclear origin), and quasi-periodicities of about 2 and 6 years. The period of 20–23 years, which is undoubtedly associated with the 22-year solar magnetic cycle, is of particular interest.

3. VARIATIONS IN THE MEAN STRENGTH OF THE PHOTOSPHERIC MAGNETIC FIELD

The GMF strength is known (Rivin and Obridko 1992; Kotov and Demidov 1980) to vary greatly in absolute value with phase of the 11-year cycle. We now have the longest data set, which allows us not only to trace this variation, but also to determine whether it has a secular trend. The presence of the latter follows from circumstantial (for the photospheric magnetic field) evidence (Lockwood *et al.* 1999).

We considered the normalized GMF set obtained above with the number of measurements $N = 11\,878$. For each year, we calculated the mean (in absolute value) GMF strength $\langle|H|\rangle$. Its variation over a period of

Solar GMF measurements during 1968–1999

Observatory	Interval, years	N	Δ, G	k	Reference
CrAO*	1968–1999	1707	0.661	0.953	Kotov *et al.* (1999)
MWO	1970–1982	2457	0.670	0.940	Kotov *et al.* (1998a)
SSO	1982–1993	313	0.775	0.813	Grigoryev and Demidov (1987), Grigoryev *et al.* (1983), and Kotov *et al.* (1998b)
WSO	1975–1999	7401	0.413	1.525	*Solar-Geophysical Data ...* (1976–1999)
Total**	1968–1999	11878	0.630	–	–

 * The Crimean measurements were supplemented with new 1998–1999 measurements with $N = 158$.
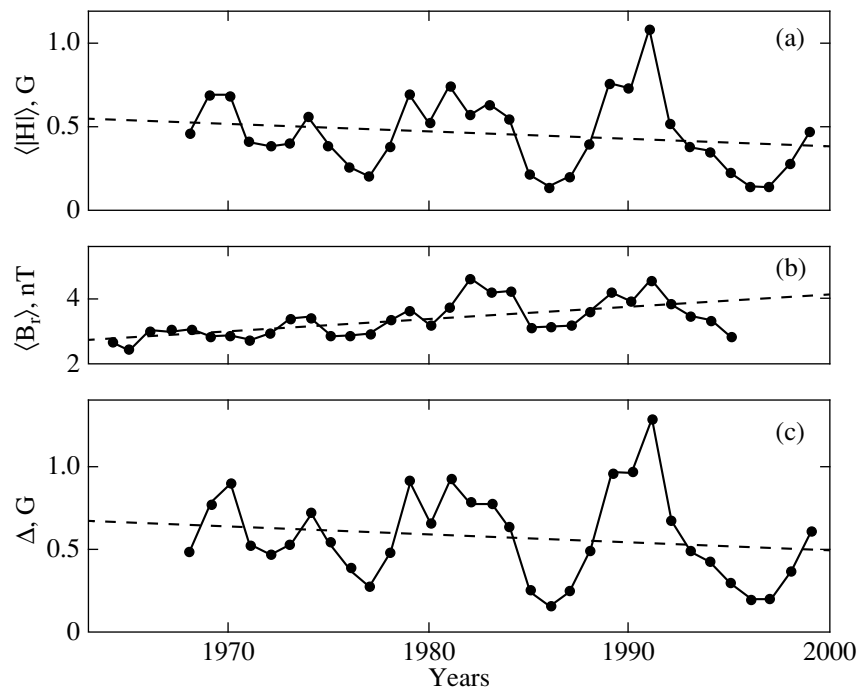
** The normalized series (see the text).

Fig. 1. Variations in the yearly mean values of (a) GMF strength $\langle|H|\rangle$, (b) radial IMF component $\langle|B_r|\rangle$ as inferred by Lockwood *et al.* (1999), and (c) rms values Δ of the GMF. The dashed lines indicate the linear regression lines.

32 years is shown in Fig. 1a, where we see the cyclic behavior with extrema following the variation in Wolf numbers W (the latter is shown in Fig. 2b).

The linear regression line of $\langle|H|\rangle$ in Fig. 1a corresponds to the equation

$$\langle|H|\rangle = 0.46(\pm 0.04) - 0.004(\pm 0.004)(t - 1984.0), \quad (1)$$

where $\langle|H|\rangle$ is in G, t is in years, and the quoted errors correspond to an uncertainty of $\pm 1\sigma$. Thus, the $\langle|H|\rangle$ values over 32 years exhibit no slow (secular) variation, within the error limits. It should be particularly emphasized that the time intervals of two series of measurements virtually overlap: the series of IMF radial component $\langle|B_r|\rangle$ and the GMF series refer to 1964–1996 and 1968–1999, respectively.

The $\langle|H|\rangle$ linear trend was also calculated for 1968–1996, which is in best agreement with the interval of IMF measurements (Lockwood *et al.* 1999):

$$\langle|H|\rangle = 0.48(\pm 0.04) + 0.000(\pm 0.005)(t - 1982.5). \quad (2)$$

There is no trend.

Some authors believe the Stanford measurements to be the most reliable GMF data; besides, they are made most regularly compared to the measurements at other observatories. At present, the Stanford data represent the largest GMF data set. Therefore, we separately calculated a linear trend for the normalized Stanford series for 1975–1999. The result obtained closely agrees with expressions (1) and (2), within the error limits:

$$\langle|H|\rangle = 0.44(\pm 0.05) - 0.002(\pm 0.007)(t - 1987.5). \quad (3)$$

We conclude that there was no substantial trend in the GMF behavior over the period 1968–1999. This is inconsistent with the result of Lockwood *et al.* (1999) for the radial IMF component [see Fig. 1b, which shows variations of the yearly mean $\langle|B_r|\rangle$, as inferred from the data of Lockwood *et al.* (1999)]. We see that the main fluctuations of $\langle|B_r|\rangle$ correspond to the extrema of $\langle|H|\rangle$ and Wolf numbers W (Figs. 1a and 2b). However, the $\langle|B_r|\rangle$ values clearly show a linear trend, which indirectly suggests an increase in the solar coronal magnetic field by 41% ($\pm 13\%$) in 32 years or almost a factor of 2 in 90 years (Lockwood *et al.* 1999).

4. VARIATION IN THE GMF ENERGY INDEX

A similar procedure was also performed for the rms values of H, more specifically, for the yearly means of Δ. Their variation over 32 years is shown in Fig. 1c; qualitatively, it essentially matches the variation in yearly mean $\langle|H|\rangle$ (Fig. 1a). The slope of the linear regression line for the yearly means of Δ (in G) is virtually the same as that for $\langle|H|\rangle$ [see expression (1)]:

$$\Delta = 0.57(\pm 0.05) - 0.005(\pm 0.005)(t - 1984.0). \quad (4)$$

Note that the slopes of the straight lines given by Eqs. (1), (3), and (4) are *negative*, although they are within the error limits, which is in conflict with the *essentially positive* slope of the regression line for the yearly mean $\langle|B_r|\rangle$ (see Fig. 1b).
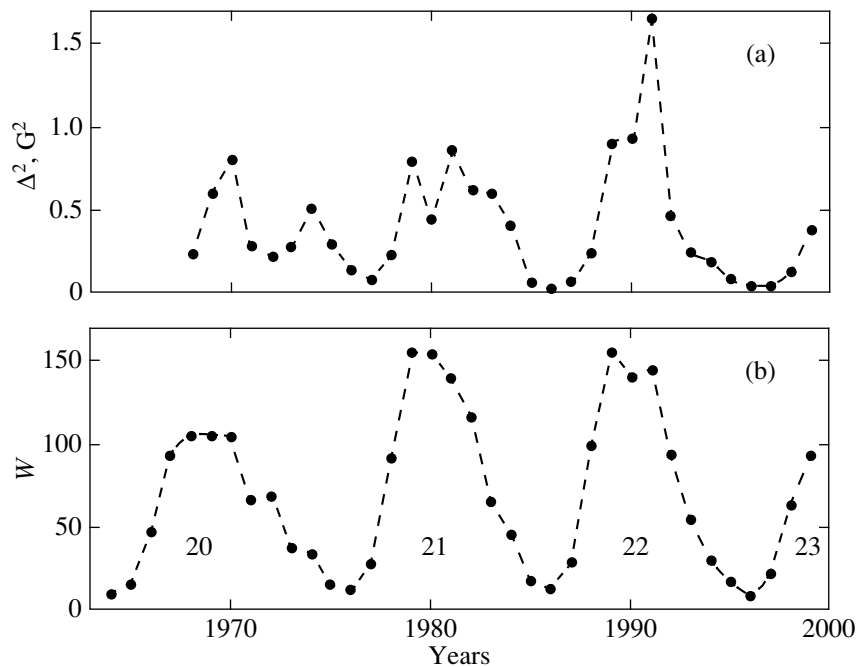
Fig. 2. The same as Fig. 1 for (a) the solar GMF energy index $E = \Delta^2$ and (b) Wolf numbers W (*Solar-Geophysical Data ...* (1976–1999)). The numerals under the envelope of Wolf numbers are solar-cycle numbers.

Temporal variations in the energy of the large-scale magnetic fields that are carried away by the solar wind into interplanetary space and that potentially affect the Earth and, probably, its climate [see Lockwood *et al.* (1999) and references therein] are also of considerable interest. As the energy index of such fields or the GMF, it would be natural to take a quantity proportional to H^2. Here, we took the yearly mean $E \equiv \Delta^2$ as the GMF energy index. Its temporal variation over the last 32 yr is shown in Fig. 2a, where we see the cyclic variation in the solar magnetic energy carried away by the solar wind into interplanetary space. The extrema of E correspond to the epochs of the minima and maxima of solar activity, i.e., the Wolf numbers W presented in Fig. 2b.

The largest release of solar magnetic energy in 1991 is also remarkable. At this time, the yearly mean GMF strength and Δ in Figs. 1a and 1b were at a maximum.

5. THE CAUSES OF DISCREPANCIES

The magnetograph signal proportional to the GMF is known (Scherrer 1973; Kotov *et al.* 1998a; Kotov and Stepanyan 1980; Grigoryev and Demidov 1987) to depend mainly on the total area occupied by background magnetic fields of a particular polarity at a mean photospheric field strength of approximately 2 G. Here, we do not consider questions related to the true structure of solar magnetic fields, to the existence of thin magnetic flux tubes with a strength of about 1 kG, and to the temperature sensitivity of the 525.0-nm line (Howard and Stenflo 1972). Therefore, one might think that the constancy of $\langle |H| \rangle$ with time compared to the

increase in radial IMF component $\langle |B_r| \rangle$ in the years under consideration was offset, for example, by a gradual decrease in the effective areas (by enhanced fragmentation) of unipolar regions on the Sun and by an increase in the mean strength of background photospheric fields. However, this is a highly artificial assumption: the main characteristics of large-scale solar fields, in particular, their sector structure, are known to be constant for decades (see, e.g., Svalgaard and Wilcox 1975).

It would also be unreasonable to attribute the discrepancy between the results to the IMF azimuthal component, i.e., to explain this difference by a gradual decrease in the winding of IMF lines (at the Earth's orbit in Parker's model). This assumption is no less speculative than the above hypothesis about the fragmentation and increase in the strength of solar background fields. The effect revealed by Lockwood *et al.* (1999) cannot be attributed to a gradual enhancement of the compression of IMF lines to the solar equatorial plane and, consequently, to ecliptic plane either. This is highly unlikely: according to magnetometer measurements from the Ulysses interplanetary spacecraft, the strength of the radial IMF component is virtually independent of heliolatitude [see Wang and Sheeley (1995) and references therein]. It was established previously (Papitashvili and Gromova, 1983) that the solar wind velocity at the Earth's orbit shows no significant cyclic variations or a slow temporal trend, while the observed rapid fluctuations are governed by transient high-velocity flows of interplanetary plasma. In addition, the IMF magnitude $|B|$ during 1963–1977 considered by Kotov

and Levitskiĭ (1983) showed no appreciable growth with time either, except for slight natural variations attributable to the 11-year cycle.

Based on the model of "thin heliospheric current sheets," Wang and Sheeley (1995) extrapolated the solar photospheric magnetic field to the Earth's orbit in the interval 1970–1993 (using MWO and WSO data). They obtained satisfactory agreement with the $|B_r|$ variations, which showed a gradual growth of the field with time confirming the result of Lockwood *et al.* (1999). However, to reconcile the data obtained by averaging magnetograms with the $|B_r|$ values, Wang and Sheeley (1995) had to introduce a factor δ^{-1} dependent on heliolatitude φ in the model. This factor was assumed to offset the well-known effect of magnetograph-signal saturation in fine-structure elements of the strong photospheric magnetic field and the so-called effect of "temperature dependence" (Howard and Stenflo 1972). In the opinion of Wang and Sheeley (1995), the necessity of introducing the factor δ^{-1} implies the existence of a strong concentration of the polar field near the epochs of maximum solar activity with a mean strength of polar coronal holes of about 10 G. The field distribution near the poles at the epochs of minimum solar activity is given by (Wang and Sheeley 1995)

$$H \approx H_0 \cos^7 (\pi/2 - \varphi), \qquad (5)$$

where $|H_0| \approx 14$ G.

The idea of a strong polar concentration of the solar field was first put forward by Svalgaard *et al.* (1978) to explain the annual field variation at the solar poles. According to their model, the field strength in polar regions is

$$H \approx H_0 \cos^8 (\pi/2 - \varphi) \qquad (6)$$

with $|H_0| = 6.4$ G at the poles themselves (note that expressions (5) and (6) are qualitatively similar); the field lines are virtually radial.

However, Kotov and Levitskiĭ (1985) adduced several serious arguments that make us question both the validity of formulas (5) and (6) and the strong polar-field concentration in general. The following should be noted regarding the extrapolation of the photospheric field (or, rather, magnetograms) to the corona, to the source surface, and then to the Earth's orbit (Wang and Sheeley 1995).

As was said above, in order to reconcile the extrapolated magnetic field with the observed variation of $|B_r|$, Wang and Sheeley (1995) had to introduce the factor

$$\delta^{-1}(\varphi) = 4.5 - 2.5 \sin^2 \varphi. \qquad (7)$$

However, the actual variation in mean magnetic field strength obtained from magnetograms and extrapolated to a distance of 1 AU from the Sun correlates only slightly with the temporal variation of $|B_r|$ if we do not introduce the latitude-dependent correction factor (7)

but take δ^{-1} = const. Figure 2a from Wang and Sheeley (1995) shows no correlation. In our view, this is an interesting and very important fact. It suggests that the latitudinal correction of the photospheric field, at least in the form (7), is not adequately justified [the inference about a polar enhancement of the field following from Eq. (7) is apparently not legitimate either). This procedure *contradicts* the variation in GMF magnitude, which clearly *correlates* with the variation in $\langle|B_r|\rangle$ even without the factor $\delta^{-1}(\varphi)$ (see Fig. 1, where the coefficient of correlation between the residual $\langle|H|\rangle$ and $\langle|B_r|\rangle$ after the removal of linear trends is 0.69) in contrast to the extrapolation of Wang and Sheeley (1995) (see Fig. 2 from their paper). By the residuals, we mean the "measurements minus trend" differences.

We believe that the reason for the discrepancy between the field calculated in the simplest model with the factor δ^{-1} = const = 1.8 (Wang and Sheeley 1995) and the measured field ($|B_r|$) is that magnetograms of the solar surface give information mostly about the magnetic fields in active regions. However, the threshold level of magnetograms (or, in other words, their sensitivity to weak background fields) is of importance in correctly determining the total photospheric magnetic flux, as in the pioneering work by Bumba *et al.* (1967). A proper determination of the zero level of magnetograms, which can include significant errors, also plays a role [special sophisticated methods for checking the instrumental displacement of a magnetograph zero level (Severny 1969; Kotov *et al.* 1998a; Grigoryev and Demidov 1987) are known to be used in GMF measurements]. The significant correlation between GMF magnitude and $\langle|B_r|\rangle$ (Figs. 1a, 1b) suggests that introducing the saturation factor $\delta^{-1}(\varphi)$ in the extrapolation of magnetograms is not necessary and is highly artificial.

Lockwood *et al.* (1999) considered a gradual enhancement (in addition to 11-year variations) of the geophysical *aa* index during the 20th century as an important argument for the growth of the solar coronal magnetic field with time from cycle to cycle. They assumed that, according to Parker's model, the variation in mean strength of the radial IMF component $|B_r|$ should correspond to the variation in magnetic flux F_S on the source surface in the solar corona. Note, however, that such an enhancement could be caused, first, by a simple increase in sunspot activity and in solar activity in general (the number of active regions) and, second, by the accompanying increase in the frequency of nonstationary processes (for example, the frequency of flares and/or coronal mass ejections) rather than by an increase in the mean coronal magnetic field and, thus, in the solar photospheric magnetic field.

The sunspot activity (as well as apparently the corresponding frequency and intensity of nonstationary processes: flares, coronal mass ejection, etc.) actually rose during the 20th century. This is clearly seen from the gradual increase in maximal Wolf numbers W of

solar cycles throughout almost the entire 20th century. However, this apparently reflects the existence of well-known secular solar cycles with a duration of $\gtrsim 90$ yr (Vitinskiĭ *et al.* 1986). As follows from our analysis of the GMF, these cycles are not related to the slow (secular) enhancement of the solar magnetic field (the solar photospheric and coronal fields).

Note, in particular, that the positive slope of the linear regression line in Fig. 1b is mainly related to the enhancements of $\langle |B_r| \rangle$ during cycles 21 and 22 compared to cycle 20. However, these enhancements can only reflect a rise in general solar activity (specifically, in Wolf numbers W) during cycles 21 and 22 (see Fig. 2b). In this case, the mean GMF was virtually constant (see Figs. 1a, 1c).

6. MEAN GMF PARAMETERS

We have at our disposal the most complete GMF data set from 1968 until 1999 [note that the main SSO data for 1985–1999 have not yet been published and will be considered later (Demidov 1999)]. Let us determine the quantities that characterize the magnetism of the Sun as a star averaged over 32 years, more specifically, the mean (in magnitude) GMF $|\overline{H}|$, the rms value $\overline{\Delta}$, and the general mean IMF $\overline{H}$. In this case, it should be noted that all 11 878 GMF values are distributed highly nonuniformly over years from $N = 82$ for 1968 to $N = 676$ for 1976. Therefore, we first determined 32 yearly mean values of the above parameters and then their means. The following results were obtained (for the total normalized GMF series for 1968–1999, see Section 2):

$$|\overline{H}| = 0.456 \text{ G,}$$

$$\overline{\Delta} = 0.570 \text{ G,}$$

$$\overline{H} = -0.030 \pm 0.018 \text{ G,}$$

at a mean strength of the radial IMF $|\overline{B_r}| \approx 3.3$ nT (i.e., 3.3×10^{-5} G, see Fig. 1b) for the similar period 1964–1996. Approximately the same value follows from the data of Wang and Sheeley (1995) for 1970–1993.

The deviation of the mean solar field $\overline{H}$ from zero is statistically significant at a level of approximately 1.7σ (90%). It is of interest for solar physics in the context of the well-known problem of the solar magnetic monopole, which has been repeatedly discussed in the literature (see, e.g., Kotov and Levitskiĭ 1985; Grigoryev and Demidov 1989; and references therein). Of course, this intriguing issue deserves a special consideration.

We see from Fig. 1a that the yearly mean GMF strength changes dramatically in magnitude from the minimum to the maximum of solar activity (on the average, from ≈ 0.16 to ≈ 0.84 G), so the relative modulation is approximately $\pm 70\%$. At the same time, the radial IMF component exhibits a much smaller modulation, changing in the range 2.9–4.2 nT, i.e., by a mere 18%. The main reason why the relative modulation amplitudes differ is that $\langle |B_r| \rangle$ is the average magnitude of the IMF strength at the Earth's orbit; i.e., the *local* fields that are stretched by the solar wind from specific regions of the visible solar hemisphere are averaged. In contrast, the GMF signal corresponds to the integral of *all* fields in the visible solar hemisphere (of course, given the corresponding weighting factors), i.e., it represents the result of adding up the contributions of background fields with their signs. At the same time, the absolute strengths of the latter are known to be virtually constant with solar cycle: the configuration and sizes of unipolar regions on the solar surface change.

This is also partly responsible for the difference between the mean strengths (in magnitude) $|\overline{H}|$ and $|\overline{B_r}|$. Indeed, for the calculated mean radial IMF component at the Earth's orbit, we have

$$\left|\overline{B_r}\right| \approx |\overline{H}| \left(\frac{R_\odot}{R}\right)^2 \approx 1.0 \text{ nT} \tag{8}$$

($R_\odot$ is the solar radius, and $R = 1$ AU), whereas the strength of the actually measured radial IMF is $|\overline{B_r}| \approx 3.3$ nT; i.e., it is a factor of 3.3 larger. Of course, the well-known saturation factor (underestimation of the magnetograph signal recorded by the 525.0-nm spectral line [Howard and Stenflo 1972; Wang and Sheeley 1995; Svalgaard *et al.* 1978]) can also play a significant role here. However, this question, along with the general problem of GMF calibration and its detailed comparison with the IMF, is beyond the scope of this study.

7. CONCLUSION

It is difficult to imagine that the magnetic field in the solar corona (on the source surface) increased by 40% in 32 years without an appreciable enhancement of the mean photospheric magnetic flux. This is especially true, because, according to theoretical models [in particular, according to the model of Wang and Sheeley (1995)], the distribution of the photospheric field must be known to calculate F_S in the corona and the strength $\langle |B_r| \rangle$ at the Earth's orbit.

We believe that the following factors are responsible for the discrepancy between our results and those of Lockwood *et al.* (1999). (i) Lockwood *et al.* (1995) used an indirect procedure to obtain information about the solar coronal field. (ii) The correlation between the mean photospheric field inferred from magnetograms and the IMF B_r component (in magnitude) is weak (see Section 5). (iii) The IMF data are limited, and the effect of the abnormally large GMF peak (and, consequently, of the IMF strength) at the maximum of solar cycle 22 may be strong (see Fig. 2a).

The GMF measurements convincingly suggest that the strength of the solar (large-scale and background)

magnetic fields averaged over the solar disk has been virtually constant in the last 32 years. Over this period, the slow trend of the GMF magnitude had the sign opposite to that obtained by Lockwood *et al.* (1999). Strictly speaking, it was insignificant and was within the error limits (–27 ± 27%) over 32 years; i.e., there was virtually no slow trend.

Concurrently, our result casts doubt on the correlation between the secular trend in solar irradiance (Willson 1997) and the slow variation in solar global magnetic field (Lockwood *et al.* 1999).

At the same time, note that, over the entire period of observations, the GMF and, consequently, the total flux of large-scale photospheric magnetic fields exhibited a distinct 11-year variation attributable to the solar cycle with a mean relative amplitude of about 70%. In this case, the maximum of the GMF strength lagged behind the maximum of solar activity and the maximum of Wolf numbers W (see Figs. 1a, 2b) approximately by two years.

REFERENCES

1. V. Bumba, R. Howard, and S. F. Smith, *Magnetic and Related Stars*, Ed. by R. C. Cameron (Mono Book Co., Baltimore, 1967).
2. M. L. Demidov, private communication (1999).
3. V. M. Grigor'ev, M. L. Demidov, and B. F. Osak, Issled. Geomagn., Aéron. Fiz. Solntsa **65**, 13 (1983).
4. V. M. Grigoryev and M. L. Demidov, in *Solar Magnetic Fields and Corona* (Nauka, Novosibirsk, 1989), Vol. 1, p. 108.
5. V. M. Grigoryev and M. L. Demidov, Sol. Phys. **114**, 147 (1987).
6. R. Howard and J. O. Stenflo, Sol. Phys. **22**, 402 (1972).
7. V. I. Haneychuk, Astron. Zh. **76**, 385 (1999) [Astron. Rep. **43**, 330 (1999)].
8. V. A. Kotov and M. L. Demidov, Izv. Krym. Astrofiz. Obs. **61**, 3 (1980).
9. V. A. Kotov and L. S. Levitskiĭ, Izv. Krym. Astrofiz. Obs. **66**, 110 (1983).
10. V. A. Kotov and L. S. Levitskiĭ, Izv. Krym. Astrofiz. Obs. **71**, 32 (1985).
11. V. A. Kotov and N. N. Stepanyan, Izv. Krym. Astrofiz. Obs. **62**, 117 (1980).
12. V. A. Kotov, P. H. Scherrer, R. F. Howard, and V. I. Haneychuk, Astrophys. J., Suppl. Ser. **116**, 103 (1998a).
13. V. A. Kotov, M. L. Demidov, V. I. Khaneĭchuk, and T. T. Tsap, Izv. Krym. Astrofiz. Obs. **94**, 110 (1998b).
14. V. A. Kotov, V. I. Haneychuk, and T. T. Tsap, Astron. Zh. **76**, 218 (1999) [Astron. Rep. **43**, 185 (1999)].
15. M. Lockwood, R. Stamper, and M. N. Wild, Nature **399**, 437 (1999).
16. V. O. Papitashvili and L. I. Gromova, Geomagn. Aéron. **23**, 130 (1983).
17. D. I. Ponyavin, in *New Solar Cycle: Observational and Theoretical Aspects* (Glavn. Astron. Obs. Ross. Akad. Nauk, St. Petersburg, 1998), p. 153.
18. Yu. R. Rivin and V. N. Obridko, Astron. Zh. **69**, 1083 (1992) [Sov. Astron. **36**, 557 (1992)].
19. P. H. Scherrer, Stanford Univ. Inst. Plasma Res. Rep., No. 554 (1973).
20. A. Severny, Nature **224**, 53 (1969).
21. *Solar-Geophysical Data Prompt Reports* (National Geophysical Data Center, Boulder, 1976–1999).
22. L. Svalgaard and J. M. Wilcox, Sol. Phys. **41**, 461 (1975).
23. L. Svalgaard, T. L. Duvall, Jr., and P. H. Scherrer, Sol. Phys. **58**, 225 (1978).
24. Yu. I. Vitinskiĭ, M. Kopetskiĭ, and G. V. Kuklin, *Statistics of Sunspot Activity* (Nauka, Moscow, 1986).
25. Y.-M. Wang and N. R. Sheeley, Jr., Astrophys. J. Lett. **447**, L143 (1995).
26. R. C. Willson, Science **277**, 1963 (1997).

Translated by Yu. Safronov

Small-Scale High-Temperature Structures in Flare Regions

V. A. Kovalev[1]*, G. P. Chernov[1], and I. Hanaoka[2]

[1] *Institute of Terrestrial Magnetism, Ionosphere and Radiowave Propagation, Russian Academy of Sciences, Troitsk, 142092 Russia*
[2] *National Astronomical Observatory, Tokyo, Japan*
Received June 5, 2000; in final form, October 9, 2000

Abstract—When analyzing YOHKOH/SXT, HXT (soft and hard X-ray) images of solar flares against the background of plasma with a temperature $T \simeq 6$ MK, we detected localized (with minimum observed sizes of ≈ 2000 km) high-temperature structures (HTSs) with $T \approx (20–50)$ MK with a complex spatial-temporal dynamics. Quasi-stationary, stable HTSs form a chain of hot cores that encircles the flare region and coincides with the magnetic loop. No structures are seen in the emission measure. We reached conclusions about the reduced heat conductivity (a factor of $\sim 10^3$ lower than the classical isotropic one) and high thermal insulation of HTSs. The flare plasma becomes collisionless in the hottest HTSs ($T > 20$ MK). We confirm the previously investigated idea of spatial heat localization in the solar atmosphere in the form of HTSs during flare heating with a volume nonlocalized source. Based on localized soliton solutions of a nonlinear heat conduction equation with a generalized flare-heating source of a potential form including radiative cooling, we discuss the nature of HTSs. © 2001 MAIK "Nauka/Interperiodica".

Key words: *solar flares, high-temperature structures, heat conductivity, solitons*

1. INTRODUCTION

The heating of flare plasma, which is studied by using YOHKOH X-ray observations, is currently discussed in terms of collisionless magnetic reconnection (Somov and Kosugi 1997; Somov *et al.* 1998). At the short-duration (of the order of 10 s) impulsive phase of a flare, accompanied by plasma evaporation, the plasma is assumed to be heated to a temperature $T \sim 8$ MK by the beams of accelerated electrons that penetrate into the chromosphere. Heating to the observed abnormally high temperatures of 30–40 MK requires heat flows from a turbulent current sheet. Plasma flows interact at the post-maximum slow phase of a flare: an intermediate temperature is established in the flare region; subsequently, the plasma must relax to its original state.

Tsuneta (1996) numerically calculated the temperature structure of a flare in the magnetic reconnection model with classical heat conductivity and with slow shock waves propagating from a spatially localized reconnection source in the corona as the flare region was heated. The results obtained point to a uniform temperature distribution.

Here, our analysis of observations has revealed small-scale high-temperature structures (HTSs) in the flare region (Kovalev *et al.* 2000), suggesting a pattern

of energy release that is qualitatively more complex than that predicted by calculations (see, e.g., Tsuneta 1996). We confirm the previously investigated idea (Kovalev 1990; Kovalev and Laptukhov 1992) that heat can be localized in the form of spatial structures in the solar atmosphere with a nonlocalized volume source of heating.

2. OBSERVATIONS

In order to study the flare scenario, we analyzed X-ray images from the YOHKOH X-ray telescope for two flares, November 4 and 28, 1997, whose development is shown in Figs. 1 and 2. The upper left panels of these figures show SOHO/MDI magnetograms of these regions. The events were accompanied by microwave radio bursts and millisecond spikes. Numerous HTSs with $T \approx 18$ MK are seen in soft X rays against the background of plasma with a temperature of 6 MK. The minimum observable HTS size is ~1 pixel (1800×1800 km). The angular resolution per pixel is $2.46'' \times 2.46''$. The images contain 64×64 pixels. Observed parameters are listed in the table.

The Flare of November 4, 1997

The November 4 event was associated with a large 2B X2.1 Hα flare in the active region NOAA 8100 (S14 W33) in the interval 05:54–05:59–07:15 UT. The onset of the November 4 flare in Hα is shown in the

---

* E-mail address for contacts: vkovalev@izmiran.troitsk.ru

Observed parameters in the center and at the edges of the flare regions on November 4 and 28, 1997: T is the temperature, ME is the emission measure, n is the density, and d is the linear HTS scale

Parameters	Nov. 4, 1997 flare		Nov. 28, 1997 flare	
	center	edge	center	edge
T, MK	6	6–18	6	18–50
EM, 10^{44} cm^{-3} per pixel	2×10^3	125	10^5	10^4
n, 10^{10} cm^{-3}	6.32	4	130	13
d, 10^3 km	–	≥ 2	2	≥ 2

upper right panel of Fig. 1 (an image from the Lermont Observatory, Australia). The flare exhibits a helmet shape above the leading spot of the south magnetic polarity.

The middle left panel of Fig. 1 shows a frame from the (SOHO/EIT) film of flare development in the ultraviolet 195 Å line (reflecting regions heated to $T \approx 2 \times 10^6$ K). Note the bright (black in negative) hot triangular flare region above the leading spot, which is similar in shape to the Hα flare region, and the ejections moving northward (toward the helmet structure mentioned above). These optical data may suggest magnetic reconnection with the X-point in the upper part of the helmet structure; the mass ejections (in the 195 Å line) noted above coincide in time and position with the halo-type coronal mass ejection (CME) from this region detected in the interval 06:10–06:15 UT with the SOHO/LASCO C1 and C2 optical coronograph. The large loop seen on the EIT 195 Å image between the leading and following spots up to heights of ≈60 000 km was relatively stable during the event. The middle right panel of Fig. 1 shows the soft X-ray image of the flare region obtained from the YOHKOH calibrated data with a Be 119-μm filter. The linear scale of this image (and of all the subsequent YOHKOH/SXT images) is ≈114 073 km.

The lower panels of Fig. 1 show the maps of volume emission measure (left) and temperature (right) in the flare region for 06:10:32 UT (when the recording first emerged from saturation after flare maximum) that we computed from the photon energies obtained with the YOHKOH/SXT soft X-ray telescope. The maps were computed by the standard method of Hara *et al.* (1992). Intensity ratios through Be119/Al12 filters, which provide the widest temperature range, were used to calculate the temperature. The emission-measure contours correspond to 125, 500, and 2000×10^{44} cm^{-3} per pixel; the heavy line indicates the 500 contour. Temperatures of 8, 10, 12, 14, 16, and 18 MK are marked on the temperature map; the heavy contour highlights the temperature of 10 MK. The emission measure is at a maximum, EM ≈ 2000×10^{44} cm^{-3} per pixel, at the center of a region with a half width of about 13 660 km. According-

ing to Krucker *et al.* (1995), the formula EM ≈ n^2qd (with a filling factor $q \sim 1$) yields the electron density $n = 6.32 \times 10^{10}$ cm^{-3}. At the same time, the plasma in a magnetic loop is more rarefied: $n = 4 \times 10^{10}$ cm^{-3} for ME ≈ 125×10^{44} cm^{-3} per pixel and for a loop diameter $d \approx 2000$ km.

The Flare of November 28, 1997

The November 28 event was accompanied by a 2B M6.8 flare in region NOAA 8113 near the eastern limb (N13 E61) in the interval 04:56–05:06–06:33 UT. The X-ray observations took place without saturation; numerous images of the flare were obtained at intervals of ≈1.5 min. Figure 2 shows three computed temperature maps, starting from flare maximum. The peak temperature was 20 MK, and the heavy contour marks 10 MK. The peak emission measure on the middle left map in Fig. 2 is 10^{49} cm^{-3} per pixel, while the heavy contour corresponds to 10^{48} cm^{-3} per pixel. There are also hard X-ray images of the flare; in the lower left panel of Fig. 2, isolines in the $M2$ (33–53 keV) energy channel are superimposed on the soft X-ray temperature map for 05:06:50 UT.

No small-scale structures are seen in the emission measure. The emission measure is at a maximum in the central core, ~2000 km in diameter. A similar estimate of the electron density yields $n \simeq 1.3 \times 10^{12}$ cm^{-3}. Magnetic loops are more rarefied: $n \simeq 1.3 \times 10^{11}$ cm^{-3} at EM ≈ 10^{47} cm^{-3} per pixel for a loop with a half-width of about 2000 km. The higher densities in this X-ray flare may suggest a large amount of evaporated photospheric plasma at a small height in the corona compared to the November 4 flare (the higher position of the latter can be seen on the Hα image in Fig. 1). When comparing the soft and hard X-ray images (the lower left panel of Fig. 2), we can see that the HTS cores are spatially close to each other in both channels, but do not coincide. The HTS temperature determined from hard X-ray emission in the M2 channel is ≈50–60 MK.

An analysis of the images reveals a complex pattern of energy release and of spatial-temporal HTS dynamics at the impulsive and decay phases of the flare: the structures are formed, interact with each other, combine together, and disappear (the right row in Fig. 2). The picture resembles a cellular medium with multiple microflares. Two types of HTS can be distinguished: quasi-stationary, long-lived (of the order of several minutes) and short-lived (with lifetimes of less than a minute) HTSs. In the magnetic loop encircling the flare region and producing a kind of an envelope, the ordered HTSs represent a quasi-stationary, stable structure in the form of an elongated chain of hot cores. Tsuneta (1996) noted an association of the high-temperature plasma with the magnetic loop. For the flare of November 28, 1997, we managed to trace the HTS establishment at the end of the impulsive phase.
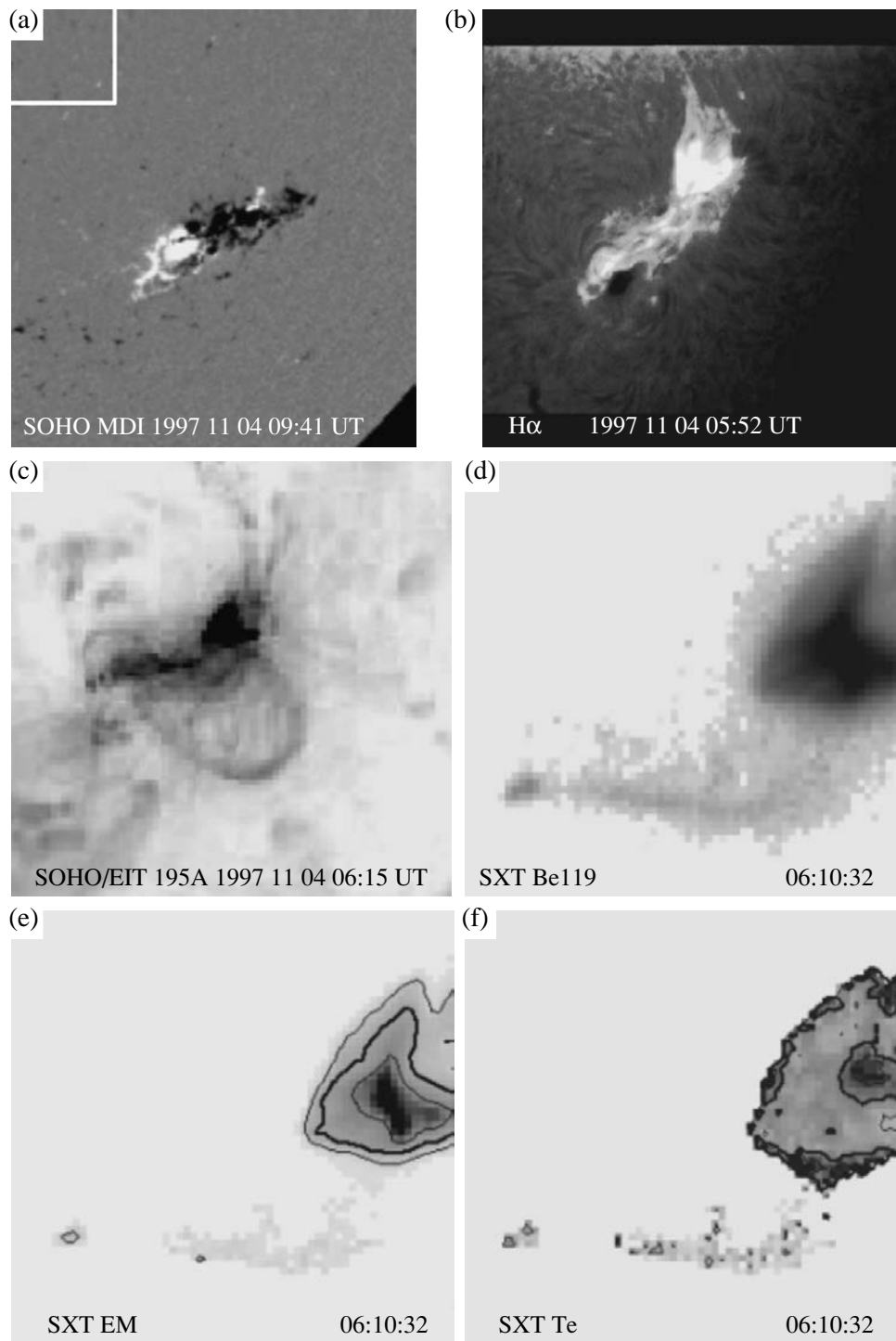
Fig. 1. Development of the November 4, 1997 flare. The upper left panel shows the SOHO/MDI magnetogram of AR 8100. The Lermont Hα (6563 Å) image of flare onset is shown in the upper right panel; the bright flare region extends upward in the form of a helmet structure above the leading spot of south magnetic polarity. The bright UV 195 Å region in the middle left frame taken from the SOHO/EIT film has the same triangular shape, although it reflects regions heated to 1.8 MK with ejections moving northward (toward the helmet structure). The middle right panel shows the flare in soft X-rays (YOHKOH/SXT) with a Be 119-μm filter (the first calibrated data were obtained only in the decay stage at 06:10:32 UT). The distribution of volume emission measure per pixel for the same time is shown in the lower left panel: the heavy and thin lines correspond to EM = 500 and 125, respectively; the peak at the center of the bright region is 2000×10^{44} cm^{-3}. The lower right panel shows the temperature map computed from the intensity ratio through Be119/Al12 filters: the heavy contour corresponds to a temperature of 10 MK; the temperature is at a maximum in bright (black) pixels, of the order of 18 MK. The scale of all X-ray images is 114 073 km (64×64 pixels with $2.46'' \times 2.46''$ sizes.)
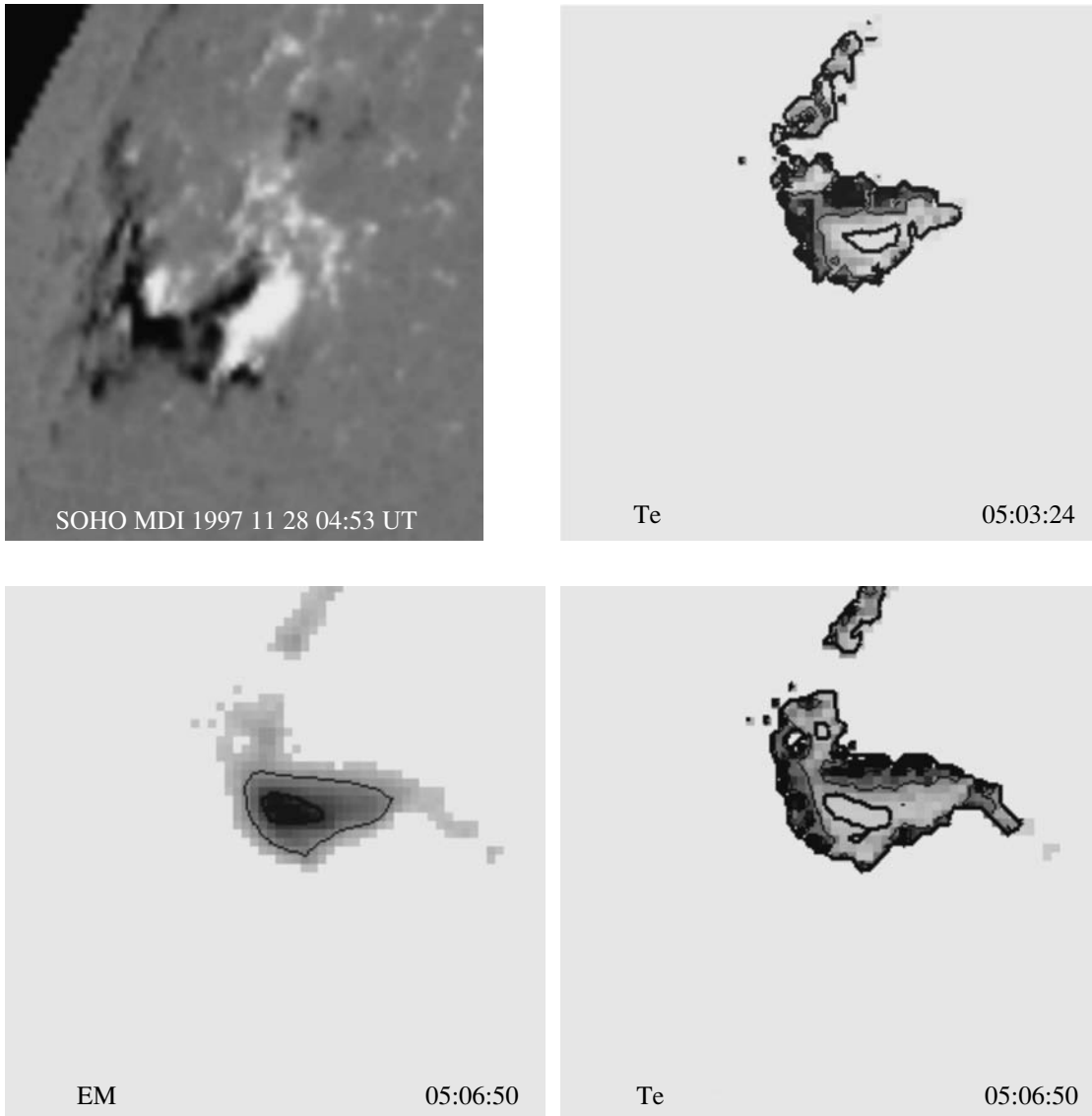
Fig. 2. Development of the November 28, 1997 flare. The upper left panel shows the SOHO/MDI magnetogram of AR 8113. Three consecutive (starting from flare maximum) temperature maps constructed from YOHKOH/SXT data by using Be119/Al12 ratios are shown on the right from top to bottom. The contours correspond to temperatures of 10 MK (heavy line) and 15 MK (thin line); the peak value along the flare loops is 20 MK. On the contour map of emission measures (middle left panel), the heavy and thin lines correspond to EM = 10^{48} and 10^{47}, respectively; the peak is at the center, 10^{48} cm^{-3} per pixel. In the lower left panel, the temperature map obtained from soft X-ray emission was superimposed on the contour map of hard X-ray emissions (YOHKOH/HXT) in the M2 (33–53 keV) energy channel at the same flare time 05:06:50 UT. Small isolated sources of hard X-ray emissions (reflecting regions heated to 30–35 MK) also lie along the flare loops, but they do not coincide with the small-scale temperature structure of soft X-ray emission.

3. THEORETICAL ANALYSIS

In our view, the detection of HTSs significantly changes the theoretical ideas of solar flares. There are no structures of this kind in currently available models. In this section, based on observations and on energy balance, we estimate flare-plasma parameters, show that spatial heat localization can take place in principle for a nonlocalized source, and obtain soliton solutions for a model heat conduction equation.

Energy Balance

Let us consider stationary plasma for which the following heat conduction equation holds:

$$c_v \frac{\partial T}{\partial t} = \text{div } \mathbf{q} + f(n, T). \quad (1)$$

Here, $c_v = 3nk_B$ is the heat conductivity, k_B is the Boltzmann constant, and $\mathbf{q}$ is the heat flux (Braginskiǐ 1963):

$$\mathbf{q} = \kappa_\parallel^e \mathbf{\nabla}_\parallel T + \kappa_\perp^i \mathbf{\nabla}_\perp T, \quad (2)$$
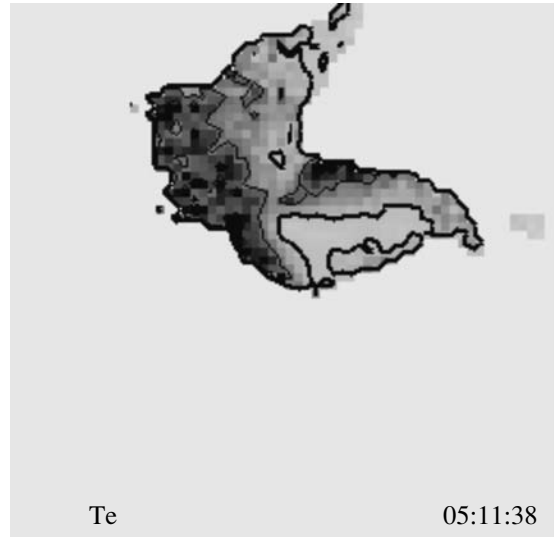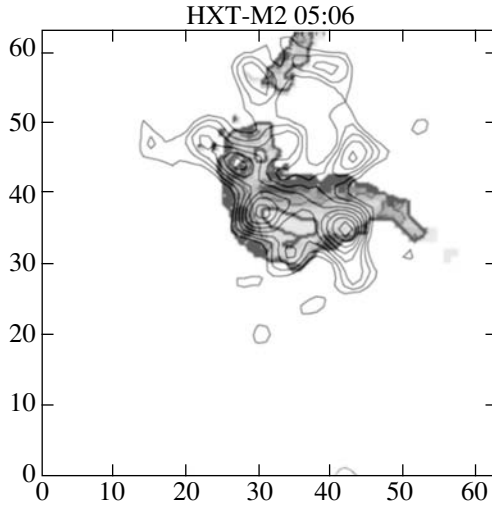
Fig. 2. (Contd.)

where $\kappa_\parallel^e$ and $\kappa_\perp^i$ are the coefficients of longitudinal electron and transverse ion heat conductivities:

$$\kappa_\parallel^e \simeq \frac{3.16 n k_B^2 T \tau_{ei}}{m_e} \simeq 10^{-6} T^{5/2}, \qquad (3)$$

$$\kappa_\perp^i \simeq \frac{2 n^2 k_B^2 T}{m_i \omega_{B_i}^2 \tau_i} \simeq 3 \times 10^{-16} \frac{n^2}{T^{1/2} B^2}, \qquad (4)$$

m_e and m_i are the electron and ion masses, τ_{ei} is the electron-ion collision time, τ_i is the ion-ion collision time, and ω_{B_i} is the ion cyclotron frequency.

The generalized source can be represented as

$$f(n, T) = Q - \mathscr{L}, \qquad (5)$$

where Q is the source of flare heating proper, which is not yet known. In particular, it can be proportional to energy flux A_γ and to heating efficiency $\epsilon(T)$ (Kaplan and Pikel'ner 1979):

$$Q = A_\gamma \epsilon(T) n. \qquad (6)$$

Cooling is included in radiative losses in the approximation of an optically thin medium: $\mathscr{L} = n^2 L(T)$, where $L(T)$ is a standard function (Rosner *et al.* 1978).

Let us obtain estimates for a HTS with $d = 2 \times 10^8$ cm, $T = 18$ MK, and $n = 4 \times 10^{10}$ cm^{-3} (the flare of November 4, 1997). The thermal energy of an individual HTS is

$$W \sim n k_B T d^3 \simeq 4 \times 10^{26} \text{ erg.} \qquad (7)$$

We simultaneously observe a relatively small number of structures (several tens); the bulk of the flare energy ($\sim 10^{31}$ erg) is most likely concentrated in cooler, unresolved small-scale structures with $d < 2000$ km. In any case, no structures are observed in the emission measure determined from background-plasma emission.

The gas-dynamical time is $t_d = d/v_{T_i} \sim 5$ s. Here, $v_{T_i} = \sqrt{k_B T / m_i} \simeq 4 \times 10^7$ cm s^{-1} is the speed of sound.

The cooling time for isotropic heat conductivity,

$$t_\kappa \sim \frac{3 n k_B d^2}{\kappa_\parallel^e} \simeq 0.4 \text{ s} \qquad (8)$$

is considerably shorter than the radiative cooling time, for which, using $L(T) \simeq 10^{-23}$ erg cm^3 s^{-1} from Mewe *et al.* (1985), we have

$$t_\mathscr{L} \sim \frac{3 n k_B T}{\mathscr{L}} \sim 10^4 \text{ s.} \qquad (9)$$

Thermal Insulation of HTSs

We see from the above estimates that the hot plasma of HTSs can rapidly cool down because of the high isotropic heat conductivity ($t_\kappa < 1$ s), so its long-term confinement in the localization region when the stable contact with background plasma is preserved requires a high degree of thermal insulation.

On the other hand, the corresponding linear heat-conduction scale,

$$d_\parallel \sim \left(\frac{\kappa T}{\mathscr{L}} \right)^{1/2} \qquad (10)$$

for isotropic heat conductivity is too large, $\sim 10^{10}$ cm. Therefore, for the observed small-scale structures to exist, the heat conductivity must be reduced by more than three orders of magnitude. What is the cause of such low heat conductivity?

The most likely cause is the effect of magnetic field, because the heat conductivity becomes anisotropic. The magnetic-field effect can be represented in Eq. (2)

by the factor $(B_z/B)^2$. To provide the observed scale in the loop, this factor with an axial field component B_z must be too low ($<10^{-3}$). However, such a configuration is unstable (Priest 1982).

At the same time, the transverse ion heat conductivity (4) results in scales that are considerably smaller than the observed ones. Thus, for example, we have $d_\perp \sim 7 \times 10^3$ cm for $B = 50$ G. In reality, however, we have to do with intermediate scales: $d_\perp < d < d_\parallel$. In this case, some intermediate heat conductivity κ must "work": $\kappa_\perp < \kappa < \kappa_\parallel$.

The gas pressure of HTS plasma exceeds the gas pressure of background plasma with $T = 6$ MK and $n = 4 \times 10^{10}$ cm^{-3}. To provide an equilibrium of the pressures inside and outside a HTS requires the pressure balance, which is possible for a stronger magnetic field outside the HTS by ~50 G. The magnetic field is expelled from the hot plasma.

The HTS flare plasma with $T > 20$ MK becomes collisionless: the mean free path,

$$\lambda_{ei} \simeq 1.3 \times 10^4 \frac{T^2}{n} \qquad (11)$$

is larger than the HTS scale length. Under these conditions, plasma turbulence can play a crucial rule, electron collisions are now determined by waves rather than by particles, and the heat conductivity, as well as the electric conductivity, decrease appreciably compared to $\kappa_\parallel^e$ (Galleev and Sagdeev 1973). However, estimates show that for the collision frequency to increase sufficiently, the turbulence level must be too high (of the order of the thermal energy). Anomalous electric and heat conductivities can result from the generation of vortices in plasma (Petviashvili and Pokhotelov 1989). An advantage of this mechanism is that it requires no difference between the electron and ion temperatures.

Thermal Instability

The formation of a HTS in a homogeneous medium can be described by the linear theory of thermal instability for a heat-conducting gas with the generalized source constructed by Field (1965). For $\partial f / \partial T > 0$, it follows from Eq. (1) for the wave mode that perturbations with

$$l \geq d_* \qquad (12)$$
$$= 2\pi \{ \kappa T / [Q + \mathcal{L}(3/2 - d\ln\mathcal{L}(T)/d\ln T)] \}^{1/2}$$

are unstable. By contrast, short-wave perturbations are stabilized by heat conduction. The condensation of cold plasma is accompanied by the heating of hot plasma; two phases are formed.

According to the general principles of synergetics, in an open system with a volume heating source and dissipation, spatial coherent structures emerge, and energetically favorable plasma self-organization takes place (Prigogine 1980; Haken 1983). The spatial distributions of temperatures fields can differ qualitatively: there can be periodic and quasi-periodic distributions among them, as well as localized-structure- and dynamic-disorder-type states (Rabinovich and Ezerskiĭ 1998).

We investigate heating with the formation of HTSs by using solutions of the heat conduction equation in two limiting cases. The $n = $ const cases with unsteady-state solutions of Eq. (1) is valid at the initial stage of the impulsive flare phase, when rapid processes with $t \ll t_d$ are considered. For the steady state, steady-state solutions are valid at constant pressure and for $t \gg t_d$.

Stationary Structures

Let us consider the steady-state equation (1) by assuming that all variables depend on the x coordinate alone:

$$\frac{dq}{dx} + f = 0, \qquad (13)$$

$$q = \kappa \frac{dT}{dx}. \qquad (14)$$

A thermal equilibrium with homogeneous solutions $T = T_i = $ const takes place at points with $f = 0$ ($Q = L$). In order to obtain inhomogeneous solutions, we multiply Eq. (13) by $\kappa(T)dT$; integration yields

$$E_k = E - U, \qquad (15)$$

$$E_k = q^2/2, \quad E = q_0^2/2, \qquad (16)$$

$$U = \int_{T_0}^{T} \kappa(T) f(T) dT, \qquad (17)$$

where the initial conditions are $x = x_0$, $q(x_0) = q_0$, and $T(x_0) = T_0$. When changing $x \longrightarrow t$ and $T \longrightarrow x$, we see an analogy with the classical problem of the motion of a mass point in a potential well (Landau and Lifshitz 1965). The quantities E_k, E, and U act as the kinetic, total, and potential energies, respectively. The motion between $T_{\min}$ and $T_{\max}$ is possible only for $U < E$. Using Eq. (14), we obtain

$$x = \frac{1}{\sqrt{2}} \int \frac{\kappa(T) dT}{\sqrt{E - U}}. \qquad (18)$$

The corresponding solutions of Eqs. (13) and (14) in the form of spatially periodic nonlinear waves, which exhibit the alternation of hot and cold regions separated by heat-conducting fronts, were obtained by Ko-valev (1990). The types and parameters of the structures (periodic waves, solitons, transition layers) are related to the temperature dependence of a generalized alternating source (Kovalev and Laptukhov 1992). Steady-state solutions are possible for

$$\int_{T_{\min}}^{T_{\max}} \kappa(T) f(T) dT = 0, \qquad (19)$$

which determines T_i (the bottom of the well). The homogeneous solution $T = T_i$ is unstable at this point ($\partial f / \partial T > 0$). To analyze the solutions, we use a polynomial form of U by assuming that $E = 0$ and $\kappa = \kappa_0 T^\sigma$.

(1) Periodic solution. For the potential well

$$U = -U_0(u - u_1)(u_2 - u),$$
$$u = T^{\sigma+1}, \quad U_0 > 0, \quad u_1 < u_2 \qquad (20)$$

we obtain

$$u = \frac{u_1 + u_2}{2} - \frac{u_2 - u_1}{2} \sin ax. \qquad (21)$$

The particle oscillates between T_1 and T_2 with the characteristic period

$$2\pi a^{-1} = \frac{\sqrt{2}\pi}{(\sigma+1)} \frac{\kappa_0}{\sqrt{U_0}}. \qquad (22)$$

(2) Solution solution. For a "well + hill" potential

$$U = -U_0(u - u_1)^2(u_2 - u), \quad U_0 > 0, \qquad (23)$$

we obtain the solution in the form of a localized structure for $u(0) = u_2$,

$$u = u_1 + \frac{u_2 - u_1}{\cosh^2 ax} \qquad (24)$$

with a characteristic width

$$2a^{-1} = \frac{2\sqrt{2}}{(\sigma+1)} \frac{\kappa_0}{\sqrt{U_0(u_2 - u_1)}}. \qquad (25)$$

The soliton solution can be commented on as follows. The particle stays for a long time at $u = u_1$ and then rapidly reaches a maximum, $u = u_2$, from which it "reflects" and again returns to its original state with $u = u_1$. In this case, the following quantity is conserved:

$$(u_2 - u_1) d^2 = \text{const}, \qquad (26)$$

where $u_2 - u_1$ is the soliton amplitude.

(3) "Wide" soliton. For a more complex potential

$$U = -U_0(u - u_1)^2(u_2 - u)(u_3 - u), \quad U_0 > 0 \qquad (27)$$

we obtain for $u(0) = u_2$ the solution

$$u = u_1 + \frac{(u_2 - u_1)(u_3 - u_1)}{u_2 + u_3 - 2u_1 + (u_3 - u_2)\cosh ax} \qquad (28)$$

with two characteristic linear scales. The first characterizes the front steepness and is determined by the coefficient of heat conductivity

$$d_1 = a^{-1} = \frac{\sqrt{2}}{(\sigma+1)} \frac{\kappa_0}{\sqrt{U_0(u_2 - u_1)(u_3 - u_1)}}, \qquad (29)$$

while the effect of the second scale,

$$d_2 = 2a^{-1}\ln[2u_3/(u_3 - u_2)] \qquad (30)$$

becomes significant at $u_2 \simeq u_3$, when the maximum of the potential approaches zero, and the particle stays for an increasingly long time in the u_2 region; d_2 increases. In this case, the soliton size, which is determined by the d_2 scale, is not related to its amplitude, as in the preceding case. In the limiting case where $u_2 = u_3$, both hills have the same height and the soliton width becomes infinitely large as we obtain a "transition-layer"-type solution. This kind of solution was analyzed by Zel'dovich and Pikel'ner (1969).

Thus, a "wide" soliton with steep edges (the smallest scale that can be determined by transverse heat conductivity) and a flat top is preferred for modeling HTSs. In the future, obtaining localized soliton solutions of the heat conduction equation in terms of inhomogeneous models (Molotkov *et al.* 1999) is promising.

Thermal Explosion

We have made sure that steady-state localized soliton-type solutions are possible for a generalized nonlinear alternating source. Let us show that in the unsteady-state case of rapid heating, such a source can result in explosion solutions. In the simplest homogeneous case where $\kappa = 0$ under the initial conditions $t = 0$ and $T(0) = T_0$ for the source

$$f = (T - T_1)(T - T_i), \quad T_i = (T_1 + 2T_2)/3, \qquad (31)$$

corresponding to the potential (23), the solution (1) appears as follows:

$$T(t) = \frac{T_i - T_1 b \exp(\alpha t)}{1 - b \exp(\alpha t)},$$
$$b = \frac{T_0 - T_i}{T_0 - T_1}, \quad \alpha = T_i - T_1. \qquad (32)$$

In this case, the solutions depend on initial conditions. For $T_0 < T_i$ and $T_0 \neq T_1$, we have an asymptotic behavior: $T \longrightarrow T_1$ as $t \longrightarrow \infty$. Point T_1 is stable. If, alternatively, $T_0 > T_i$, then we obtain an explosion solution when the temperature formally becomes infinite following a hyperbolic law $\sim (t_{\text{cr}} - t)^{-1}$ in a finite time:

$$t_{\text{cr}} = \frac{1}{\alpha} \ln \frac{T_0 - T_i}{T_0 - T_i}. \qquad (33)$$

The value of t_{cr} decreases with increasing T_0.

It can be shown that in a medium with a power-law source,

$$f \sim (T - T_i)^\beta, \quad \beta > 1 \qquad (34)$$

an explosion solution with a hyperbolic temperature behavior takes place:

$$T \sim (t_{cr} - t)^{-\frac{1}{\beta - 1}}. \tag{35}$$

Heat localization with the formation of metastable discrete HTSs on the scale

$$d = \frac{2\pi}{\sigma}\sqrt{\sigma + 1}\sqrt{\kappa_0/Q_0}, \quad \kappa = \kappa_0 T^\sigma, \tag{36}$$

arises "in a sharpening mode" when solving the heat conduction equation with a nonlinear source of the form $f = f_0 T^\beta$ under the condition $\beta > \sigma + 1$ (Kurdyumov 1982; Akhromeeva *et al.* 1992). This mechanism may take place at the initial formation phase of nonstationary HTSs, because the condition $\beta > \sigma + 1$ is easily satisfied for transverse heat conductivity. Such solutions can be related to short-lived HTSs with $t \ll \min(t_\kappa, t_d)$.

Flare Scenarios, the Source, and HTSs

An analysis of the observations leads us to conclude that plasma regions with markedly differing properties lie in the neighborhood of the flare region. Golub (1997), who observed the coincidence of the emission sources in different energy bands, pointed to a similar property of the flare plasma. This is possible in the presence of small-scale structures with different temperatures. In our case, hot HTSs are surrounded by relatively cool plasma; the reverse situation with cool cores embedded in hot plasma is also observed. If the formation takes place under nonequilibrium conditions, then much of the flare region can be porous and consist of convective cells (Kadomtsev and Pogutse 1967) or of filamentary structures rather than be a continuous medium. Such plasma exhibits several new macroscopic properties. In particular, since the plasma is fractal, the radiation increases in intensity (Smirnov 1993). The same (spatially resolved) volume contains cold and hot elements and, hence, simultaneously emits radiation in various temperature ranges. Such a situation apparently takes place in our observations as well. Thus, for example, no structures similar to HTSs were found in the emission measure, which may be attributable to the following circumstance. The emission measure was determined from (~6 MK) background plasma. If, however, the background plasma consisted only of unresolved (< 2000 km) structures embedded in HTSs (or without them), then this explanation is quite acceptable. An in-depth analysis of the effect of the fractal flare-region structure on radiation parameters will be performed in the next paper.

The question of the flare mechanism and the source nature is still an open question. This may be the widely discussed mechanism of magnetic reconnection (Sakei and De Jager 1996; A. Podgornyǐ and I. Podgornyǐ 2000). A model with the fragmentation of flare energy release

with multiple elementary microflares (magnetic islands, current sheets) was considered by Vlahos (1993).

An alternative viewpoint associates the flare mechanism with the dissipation of electric currents (Alfven and Karlqvist 1967; Zaǐtsev *et al.* 1998). In the model of a helmet magnetic configuration mentioned above (Tsuneta 1996), the source (current sheet) and the flare region, which acts as a "target," are spatially separated. There are no HTSs in such models.

HTS observations indicate that models in which the source and the flare region are inseparable hold; i.e., the source of flare heating, as well as radiative cooling, has a volume nature. Flare heating is accompanied by a reduction in the heat removal of coronal plasma. Energy release accompanied by coronal heating continuously proceeds in the corona, which is an open system. The heating source is not yet known (Priest *et al.* 1998). The mechanisms of wave and current dissipation are being discussed. The energy flux from the solar interior is constant. Many manifestations of solar activity, including flare events, eventually result from the "operation" of the same volume source. Magnetic-field restructuring because of photospheric motions may be responsible for the reduction in the heat removal of the HTS-forming coronal plasma. This scenario is consistent with present-day observations and should be further studied both experimentally and theoretically.

Finally, it should be noted that a number of problems that arise when interpreting observational facts established long ago can be solved through the high-spatial-resolution observations discussed here. The quasi-periodic pulsations, the fine temporal structure of flares, in particular, in the radio range, and other phenomena can be associated with HTS dynamics.

4. CONCLUSION

(1) Having analyzed soft X-ray observations of solar flares against the background of plasma with $T \sim 6$ MK, we detected small-scale high-temperature structures (HTSs) with minimum sizes of ~2000 km. Their temperatures reach ≈ 20 MK and, in several cases, ~50 MK. There are also cool cores with temperatures below the background, $T < 6$ MK. No structures were found in the emission measure, which is at a maximum at the center of the flare region.

(2) HTSs exhibit a complex spatial-temporal dynamics: they are formed, interact with one another, combine, and disappear. The duration of short-lived HTSs is less than a minute; quasi-stationary HTSs exist throughout the entire hot flare phase.

(3) In a magnetic loop, the ordered HTSs represent a quasi-stationary structure in the form of a chain of hot cores. Geometrically, the HTS cores in soft (~20 MK) and hard (~50 MK) X-rays are close to each other, but do not coincide.

(4) The heat conductivity of solar-flare plasma was found to be reduced (a factor of ~10^3 lower than the

classical isotropic one), suggesting high HTS thermal insulation. We justified the hypothesis that flare heating is accompanied by a reduction of the heat removal in an active region.

(5) In the hottest HTSs ($T > 20$ MK), the flare plasma is collisionless: the electron mean free path is larger than the structure linear size.

(6) We confirmed the previously studied idea (Kovalev 1990) that heat can be spatially localized in the form of temperature structures in a flare region with a nonlocalized volume source of heating.

(7) Based on localized soliton solutions of a nonlinear heat conduction equation with a generalized flare-heating source of a potential form including radiative cooling, we discussed the nature of HTSs. We showed that flare heating could take place in the sharpening mode (explosion solutions with a hyperbolic rise in temperature).

HTSs should be further investigated along the following lines:

(i) A detailed study of spatial-temporal HTS dynamics during flares in various energy bands, including microwave observations with a high temporal and spatial resolution (VLA, Nobejama).

(ii) The inclusion of HTSs affecting the physical processes in theoretical flare models. An analysis of HTS formation conditions, stability, and dynamics based on MHD equations and fractal theory.

ACKNOWLEDGMENTS

REFERENCES

1. T. S. Akhromeeva, S. P. Kurdyumov, G. G. Malinetskiĭ, and A. A. Samarskiĭ, *Nonstationary Structures and Diffusion Chaos* (Nauka, Moscow, 1992).
2. H. Alfven and P. Karlqvist, Sol. Phys. **1**, 220 (1967).
3. S. I. Braginskiĭ, in *Reviews of Plasma Physics*, Ed. by M. A. Leontovich (Gosatomizdat, Moscow, 1963; Consultants Bureau, New York, 1963), Vol. 1.
4. G. B. Field, Astrophys. J. **142**, 531 (1965).
5. A. B. Galeev and R. Z. Sagdeev, in *Reviews of Plasma Physics*, Ed. by M. A. Leontovich (Atomizdat, Moscow, 1973; Consultants Bureau, New York, 1979), Vol. 7.
6. L. Golub, Sol. Phys. **174**, 99 (1997).
7. H. Haken, *Advanced Synergetics: Instability Hierarchies of Self-Organizing Systems and Devices* (Springer-Verlag, New York, 1983; Mir, Moscow, 1985).
8. H. Hara, S. Tsuneta, J. R. Lemen, *et al.*, Publ. Astron. Soc. Jpn. **44**, 135 (1992).
9. B. B. Kadomtsev and O. P. Pogutse, in *Reviews of Plasma Physics,* Ed. by M. A. Leontovich (Atomizdat, Moscow, 1967; Consultants Bureau, New York, 1970), Vol. 5.
10. S. A. Kaplan and S. B. Pikel'ner, *Physics of the Interstellar Medium* (Nauka, Moscow, 1979).
11. V. A. Kovalev, Kinematika Fiz. Nebesnykh Tel **6**, 38 (1990).
12. V. A. Kovalev and A. I. Laptukhov, Issled. Zemli Kosmosa, No. 1, 11 (1992).
13. V. A. Kovalev, G. P. Chernov, and I. Hanaoka, in *The Sun at Maximum Activity and Solar–Stellar Analogies. Abstracts of Papers* (Glavn. Astron. Obs. Ross. Akad. Nauk, St. Petersburg, 2000), p. 39.
14. S. Krucker, A. O. Benz, M. J. Aschwanden, and T. S. Bastian, Sol. Phys. **160**, 151 (1995).
15. S. P. Kurdyumov, *Modern Problems of Mathematical Physics and Computational Mathematics* (Nauka, Moscow, 1982), p. 217.
16. L. D. Landau and E. M. Lifshitz, *The Classical Theory of Fields* (Nauka, Moscow, 1965; Pergamon, Oxford, 1975).
17. R. Mewe, E. H. B. M. Gronenshild, and G. H. J. van den Oord, Astron. Astrophys., Suppl. Ser. **62**, 197 (1985).
18. I. A. Molotkov, S. A. Vakulenko, and M. A. Bisyarin, *Nonlinear Localized Wave Processes* (Yanus-K, Moscow, 1999).
19. V. I. Petviashvili and O. A. Pokhotelov, *Isolated Vortexes in Plasma and Atmosphere* (Énergoizdat, Moscow, 1989).
20. A. I. Podgornyĭ and I. M. Podgornyĭ, Astron. Zh. **77**, 467 (2000).
21. E. R. Priest, *Solar Magnetohydrodynamics* (Reidel, Dordrecht, 1982; Mir, Moscow, 1985).
22. L. R. Priest, C. R. Foley, J. Heyvaerts, *et al.*, Nature **393**, 6685 (1998).
23. I. Prigogine, *From Being to Becoming: Time and Complexity in the Physical Sciences* (Freeman, San Francisco, 1980; Nauka, Moscow, 1985).
24. M. I. Rabinovich and A. B. Ezerskiĭ, *Dynamical Theory of Shaping* (Yanus-K, Moscow, 1998).
25. R. Rosner, W. H. Tucker, and G. S. Vaiana, Astrophys. J. **220**, 643 (1978).
26. J. I. Sakei and C. De Jager, Space Sci. Rev. **77**, 1 (1996).
27. B. M. Smirnov, Usp. Fiz. Nauk **163**, 51 (1993) [Phys. Usp. **36**, 267 (1993)].
28. B. V. Somov and T. Kosugi, Astrophys. J. **485**, 859 (1997).
29. B. V. Somov, T. Kosugi, and T. Sakao, Astrophys. J. **497**, 943 (1998).
30. S. Tsuneta, Astrophys. J. **456**, 840 (1996).
31. L. Vlahos, Adv. Space Res. **13**, 161 (1993).
32. V. V. Zaĭtsev, A. V. Stepanov, S. Urpo, and S. Pohjolainen, Astron. Zh. **75**, 455 (1998) [Astron. Rep. **42**, 400 (1998)].
33. Ya. B. Zel'dovich and S. B. Pikel'ner, Zh. Éksp. Teor. Fiz. **56**, 310 (1969) [Sov. Phys. JETP **29**, 170 (1969)].

Translated by V. Astakhov